Acoustic Transfer Functions Derived from Finite Element Modeling for Thermoacoustic Stability Predictions of Gas Turbine Engines

By

Paul Black

Thesis submitted to the Faculty of the

Virginia Polytechnic Institute and State University

In partial fulfillment of the requirements for the degree of

Masters of Science

In

Mechanical Engineering

Approved:

Robert L. West, Advisor

Uri Vandsburger, Committee Member

William Baumann, Committee Member

May 7, 2007

Blacksburg, Virginia Tech

Keywords: Acoustics, transfer function, finite element, thermoacoustic instability, combustor

Acoustic Transfer Functions Derived from Finite Element Modeling for Thermoacoustic Stability Predictions of Gas Turbine Engines

Paul Black

(Abstract)

Design and prediction of thermoacoustic instabilities is a major challenge in aerospace propulsion and the operation of power generating gas turbine engines. This is a complex problem in which multiple physical systems couple together. Traditionally, thermoacoustic models can be reduced to dominant physics which depend only on flame dynamics and acoustics. This is the general approach adopted in this research. The primary objective of this thesis is to describe how to obtain acoustic transfer functions using finite element modeling. These acoustic transfer functions can be coupled with flame transfer functions and other dynamics to predict the thermoacoustic stability of gas turbine engines. Results of this research effort can go beyond the prediction of instability and potentially can be used as a tool in the design stage. Consequently, through the use of these modeling tools, better gas turbine engine designs can be developed, enabling expanded operating conditions and efficiencies.

This thesis presents the finite element (FE) methodology used to develop the acoustic transfer functions of the Combustion System Dynamics Laboratory (CSDL) gaseous combustor to support modeling and prediction of thermoacoustic instabilities. In this research, several different areas of the acoustic modeling were addressed to develop a representative acoustics model of the hot CSDL gaseous combustor. The first area was the development and validation of the cold acoustic finite element model. A large part of this development entailed finding simple but accurate means for representing complex geometries and boundary conditions. The cold-acoustic model of the laboratory combustor was refined and validated with the experimental data taken on the combustion rig.

The second stage of the research involved incorporating the flame into the FE model and has been referred to in this thesis as hot-acoustic modeling. The hot combustor acoustic model required

accounting for the large temperature gradients that are inherent in any combustion system. A detailed analytical study of temperature dependent wave propagation was performed and compared to finite element results. This was done for a very simple geometry so that the temperature effects could be isolated. The outcome of this study revealed that the closed form analytical solution and finite element results match exactly.

The hot-acoustic model also required the investigation and characterization of the flame as an acoustic source. The detailed mathematical development for the full reacting acoustic wave equation was investigated and simplified sufficiently to identify the appropriate source term for the flame. It was determined that the flame could be represented in the finite element formulation as a volumetric acceleration, provided that the flame region is small compared to acoustic wavelengths. For premixed gas turbine combustor flames, this approximation of a small flame region is generally a reasonable assumption.

Both the high temperature effects and the flame as an acoustic source were implemented to obtain a final hot-acoustic FE model. This model was compared to experimental data where the heat release of the flame was measured along with the acoustic quantities of pressure and velocity. Using these measurements, the hot-acoustic FE model was validated and found to correlate with the experimental data very well.

The thesis concludes with a discussion of how these techniques can be utilized in large industrial-size combustors. Insights into stability are also discussed. A conclusion is then presented with the key results from this research and some suggestions for future work.

Acknowledgements

I would like to thank my wife, Emily for her patience and help. I would also like to express my sincere appreciation for my advisor Dr. West, as well as, my committee members Dr. Vandsburger and Dr Baumann. In addition, I would like to thank the members of my research group Joe and Chris for their help and advice. Lastly, I would like to express my appreciation to the United States Department of Energy for their sponsorship of this project.

Table of Contents

List of Figures

List of Tables

Chapter 1

1 Introduction

1.1 Statement of Need and Overview

Thermoacoustic instabilities are a problem in a variety of combustion systems such as ramjets, rocket motors, afterburners, and gas turbine engines. This problem manifests itself differently depending on the application. Typically in aerospace applications, the instability tends to appear at high frequencies. Consequently, these types of instabilities are sometimes referred to as screech. On the other hand, in large power generating gas turbine engines, the instabilities typically occur at lower frequencies and are sometimes referred to as chugging. These instabilities produce extremely large pressure fluctuations. In some cases these pressure fluctuations can exceed more than 10% of the operating pressure [1]. Consequently, thermoacoustic instabilities can lead to significant structural damage.

This work will focus on thermoacoustic instabilities in lean premixed and prevaporized power generating gas turbine engines. The word lean, in this case, means a low fuel to air ratio. This provides the desired cleaner combustion, but it also contributes to an increased onset of instability. In order to avoid this problem, the operating range of the combustor must be limited. Consequently, a big push has been made in the combustion community to understand and model thermoacoustic instabilities. The end goal is to have the knowledge and tools to make educated design changes which will reduce the onset of instability.

The study of thermoacoustic instabilities is a challenging problem due to the coupling of many complicated physical processes. However, a simplified problem statement can be given if one assumes that the flame and the acoustics constitute the dominant physics. In this case, the natural fluctuations in the flame cause local thermal expansion of the surrounding fluid. This expansion of the fluid local to the flame creates acoustic waves which will propagate up and down the combustor forming acoustic standing waves. This is always occurring in any combustion system to some degree. However, the instability occurs when the two following conditions are met:

1) Acoustic waves are in phase with the flame fluctuations (heat is added when fluid is compressed, heat removed when fluid is under rarefaction)
2) Flame perturbations are strong enough to overcome the damping in the system

Under these conditions, the acoustics will cause the heat fluctuations of the flame to increase, and consequently, the heat fluctuations of the flame will cause the acoustic response to grow. This self-excitation will continue to increase until a limit cycle is reached.

Although the statement above pinpoints the cause of the problem, trying to model thermoacoustic instabilities in a real system is extremely difficult. Many, in both industry and academia, have spent a great deal of time, money, and effort trying to more fully understand this phenomenon. In trying to understand thermoacoustic instability, many different approaches have been utilized. Among these approaches, some of the most common have been computational fluid dynamics, analytical and reduced-order models, and finite element modeling. The research done in Virginia Tech's Active Combustion Control Group (VACCG) which is presented in this thesis uses a combination of reduced-order modeling and finite element modeling. This work was sponsored by the US Department of Energy to investigate thermoacoustic instabilities in power generating gas turbine engines which operate on premixed and prevaporized hydrocarbon fuel.

As described above, thermoacoustic instability is a complex problem that limits the performance of gas turbine engines. There has been some attempt in the past to use active control as a solution. However, this method is expensive and difficult to maintain. The goal of this research has been to improve the understanding and the modeling of thermoacoustic instabilities. The results of this effort could potentially provide for improvements in the area of "passive control". Here, the usage of passive control refers mainly to the ability to make design changes in the gas turbine engine which could improve performance and operating conditions.

It was hypothesized by VACCG that a reduced-order modeling approach would be capable of capturing the dominant physics and behavior of thermoacoustic instabilities. With such a model, predictions could be made as to the stable operating conditions of the combustor. In addition, this reduced-order model could potentially be used for making improvements in passive control efforts.

The thermoacoustic reduced-order model proposed in this research is outlined in the block diagram shown in Fig. 1.1.

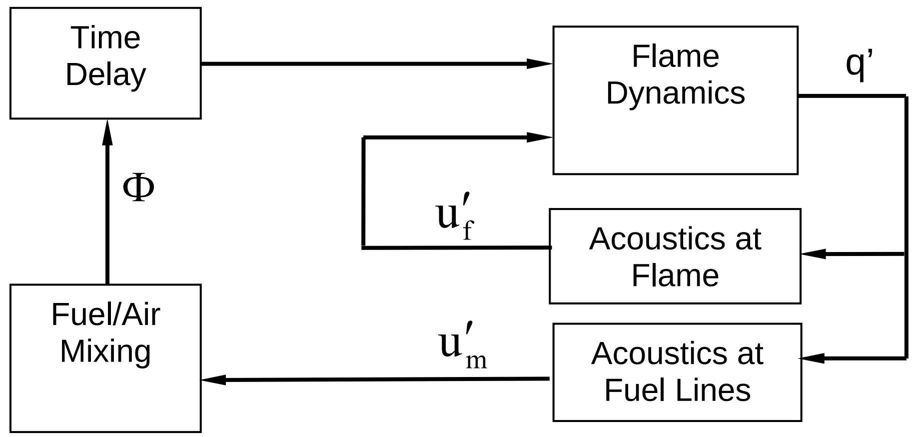

Fig. 1.1: Block diagram of a reduced-order thermoacoustic system

Each block in the figure above can be described by a transfer function which is a mathematical representation of the relationship between the input and output of a linear time-invariant system. Consequently, each of the five transfer functions shown in the figure above can be produced independently and simply combined using linear systems theory. The transfer function modeling approach is commonly used in signal processing and control theory to characterize systems. This approach has been adopted in this research for its ability to break up a complex system into multiple independently modeled subsystems. In addition, this approach is consistent with the work of other researchers in this area, namely the combustion research group at MIT [1].

As seen in the block diagram, there are two needed acoustic transfer functions: "Acoustics at Flame" and "Acoustics at Fuel Lines". The "Acoustics at Flame" transfer function is essentially the ratio between the acoustic velocity taken directly upstream of the flame relative to the dynamic flame heat release. This transfer function is used to characterize how the acoustics alter the air flow that the flame receives. The "Acoustics at Fuel Lines" transfer function is the ratio between the acoustic velocity at the fuel lines relative to the dynamic heat release of the flame. This transfer function is coupled with the "Fuel/Air Mixing" and "Time Delay" transfer functions to describe the unsteady fuel given to the flame. These acoustic transfer functions are combined with the transfer functions for the "Flame Dynamics" to produce the feedback system shown in the block diagram above.

As with any feedback system, under certain operating conditions, the system can go unstable. Once the system goes unstable, it is inherently nonlinear. However, the feedback system shown in the figure above focuses only on the linear operating range of the combustor. Consequently, the reduced-order modeling approach should still remain valid in the linear operating range.

One of the unique contributions to this work has been the use of finite element analysis to develop the acoustic transfer functions. The work presented in this thesis will focus on the acoustic finite element development specifically for gas turbine engine combustors.

1.2 Hypothesis and Goals

At the onset of this research, it was believed that by using ABAQUS as a finite element tool, the combustor acoustics could be characterized adequately to obtain the acoustic transfer functions for the reduced-order model. In order to achieve this goal, several areas needed to be researched and resolved.

The first area was properly characterizing the complex geometry of the combustor. It is widely believed and experimentally verified that lean premixed flames have a low-pass filter characteristic. This means that the flame will respond to low frequency perturbations in the air flow and fuel, however, the flame will be unaltered by high frequency perturbations. Typically, for the lean premixed flames, the bandwidth is less than 1000 Hz. Consequently, the frequency range of interest for the acoustic modeling is less than 1000 Hz. In fact, based on the bandwidth of the laboratory combustion flame used in this study, it was found that a frequency range of about 500 Hz was sufficient. In this low frequency, only 1-D plane acoustic wave propagation exists. Therefore, it was hypothesized that a 1-D acoustic FE model would be able to capture the acoustic response adequately. In making this assumption, methods were needed to transform complex geometries and boundary conditions into equivalent cross sections, lengths, and impedances.

Another area of research addressed in this thesis is the treatment of flame effects on the acoustics. It was believed that the large temperature gradients of the flame would significantly alter the acoustic wave propagation. These effects are very difficult to experimentally measure. Therefore, closed form analytical solutions were investigated and compared to temperature gradient representations in the acoustic finite element model. In doing this, simple case studies were examined to isolate the effects of temperature on the acoustics. It was believed that through this analytical and numerical study, the proper representation of the temperature gradients could be discovered and incorporated into the model.

The representation of the flame as an acoustic source was another challenge that had to be overcome. In this case, a theoretical and mathematical approach was taken. The approach required a derivation of the complete reacting wave equation starting from the conservation laws. This derivation is not new, and has been made by researchers in the past. However, the goal in this case was to get these mathematical expressions in an appropriate form to extract a source term that could be implemented in a finite element formulation. As a result of this, it was found that the heat release source of the flame is mathematically proportional to a volumetric acceleration source. The resulting volumetric acceleration source can easily be implemented as an acoustic source in a finite element analysis. The biggest assumption in this analysis is that the flame is compact compared to the acoustic wavelength.

In order to validate the assumption stated above, as well as, other assumptions used to model the acoustics, experimental measurements were taken on the VACCG laboratory combustion rig. It was believed that the most appropriate means of validating the model was through the measurement of the acoustic transfer functions. In the frequency domain, these are known as frequency response functions. The measurements taken to reconstruct the frequency response functions were dynamic flame heat release, acoustic pressure, and acoustic velocity.

Lastly, it was desired to relate the approaches taken in this research to a larger industrial scale. Although this was not a primary objective of the research, some effort was put forth to provide some suggestions as to how this research could apply to a larger scale.

1.3 Thesis Objectives and Outline

As discussed above, the general objective of this thesis is to explain the finite element modeling methods used to obtain the appropriate acoustic transfer functions for thermoacoustic reduced-order models. This effort involves multiple different sub-objectives and they are outlined below with their corresponding chapters. The thesis is broken into four main areas: research review and overview of acoustic FE modeling, cold acoustic combustor modeling, hot-acoustic combustor modeling, and insights and implementation.

1.3.1 Research review and overview of acoustic FE modeling

- Review other research that has been done in the area of thermoacoustic modeling (Chapter 2)
- Overview general finite element formulation (Chapter 3)
- Investigate general source and damping representations (Chapter 3)
- General development of acoustic models in commercial FE software (Chapter 3)

1.3.2 Cold acoustic combustor modeling

- Overview process for modeling 1-D combustor acoustics (Chapter 4)
- Provide equivalent lengths, cross sections, and impedances for complex geometry and boundary conditions, (Chapter 4)

- Develop methods for validating the cold acoustic models (Chapter 5)
- Compare cold acoustic FE results with cold acoustic experimental data (Chapter 5)

1.3.3 Hot-acoustic combustor modeling

- Perform analytical case studies to investigate temperature effects on the acoustic response (Chapter 6)
- Compare the results of the temperature dependency case studies to finite element results to reconcile how temperature effects can be treated in the FE code (Chapter 6)
- Develop an equivalent acoustic source for the flame that can be implemented in a FE formulation (Chapter 7)
- Develop methods for validating the hot-acoustic models (Chapter 8)
- Compare hot-acoustic FE results with hot-acoustic experimental data (Chapter 8)

1.3.4 Insights and implementation

- Discuss the application of modeling techniques for industrial size gas turbine engines (Chapters 9)
- Discussion of insights gained into thermoacoustic stability from the acoustic model (Chapters 9 and 10)
- Provide key results and give recommendations for future work (Chapter 10)

1.4 Scope of Thesis

As previously stated, this work was based on the modeling and verification of a laboratory combustion rig. Consequently, the complexity and scale of the problem was significantly reduced so that fundamental issues could be researched and addressed. These issues have been detailed in the objectives listed above. Specifically some of the issues that could potentially be important but are not addressed in this thesis are:

- Boundary condition characterization of the compressor and turbine
- 3-D finite element considerations
- Characterization of the flame as an acoustic source for large flames relative to acoustic wave length

It should be noted that in general this thesis is not meant to represent a complete set of guidelines for developing acoustic transfer functions. Rather, it is well suited as an initial building block to help one start the modeling process.

Chapter 2

2 Literature Review

2.1 Background

One of the first recorded studies on the phenomena of thermoacoustics instability was done by Lord Rayleigh in his work entitled the Theory of Sound [4]. In fact, his criterion for characterizing thermoacoustic instability is still widely used today. The Rayleigh Criterion states that a thermoacoustic process is amplified when the heat release from the combustion is in phase or strongly correlated with the acoustic pressure variations. Likewise the thermoacoustic process is dampened when the heat release and pressure are out of phase. This is a simple and powerful statement that summarizes the phenomena of thermoacoustic instability.

Although thermoacoustic instabilities were observed even before Lord Rayleigh's time in the late 1700's, they were never of much interest until the 1940's and 50's when the gas turbine engines and other technologies started to emerge. As the aerospace industry expanded, instabilities were also observed in ramjets, rocket motors, and afterburners. However, it wasn't until the Clean Air Act was passed in the 1990's that thermoacoustic research really became a primary focus. The Clean Air Act was a federal law concerning the reduction of smog and atmospheric pollution. Consequently, this act imposed strict regulations on the formation of nitrogen oxides vented into the atmosphere as a by-product of combustion. In order to reduce these pollutants, leaner combustion was required. However, the consequence of lean combustion is an increase in the onset of thermoacoustic instability. These instabilities limit the operating range of combustion and can also lead to significant structural damage to the combustion section of a gas turbine engine. In 2003, the cost of repair and replacement of hot-section components (much of which is attributed to combustion dynamics) was said to exceed one billion dollars annually [5].

As stated above, Lord Rayleigh came up with a criterion for describing thermoacoustics. Although the statement outlines the basics of thermoacoustic instability, the accurate modeling of this phenomenon requires understanding and quantifying many different dynamic components. For example, the combustion process includes physical processes for fluid dynamics, acoustics, chemical kinetics, feedline dynamics, mixing, transport processes, flame kinematics, and heat transfer. In order to model such a system, we must determine which components to include and the appropriate level of detail that is required. Therefore, in the past, several different approaches have been used to attack this problem of thermoacoustic instabilities. Generally speaking the approaches can be divided into the following groups:

- Computational Fluid Dynamic Models
- Analytical or Reduced-order Flame Models
- Transfer Matrix and Finite Element Acoustic Models

2.2 Computational Combustion and Fluid Dynamic Modeling

In recent years, significant progress has been made in the area of Computational Fluid Dynamics (CFD). Consequently, CFD has become increasingly popular in the combustion community. In the past, numerical combustion was generally only capable of performing stationary classical turbulent combustion. This was done through a tool called Reynolds Averaged Navier Stokes, RANS. However, tools such as Direct Numerical Simulation, (DNS) and Large Eddy Simulations, (LES) have allowed for simulating the dynamics of the flame.

In the case of DNS, the full reacting flow equations are solved without any turbulent model. Consequently, the whole range of spatial and temporal scales of turbulence must be resolved. Particularly with DNS, simplifications must be implemented to obtain results [6]. The drawback of the DNS approaches is that it can lead to extremely large models which are very time consuming and tedious to build and can take days to solve on supercomputers. Consequently, one is left with less time for model exploration and validation which is a critical step in understanding the problem of thermoacoustic instabilities.

Large Eddy Simulations numerically calculate only the large structures in the flow field. Consequently, this method is less computationally expensive as compared to the DNS approach, and it is more in line with the relative scales of the physics. There have been several researchers that have proposed that one cause of thermoacoustic instability can be attributed to large scale vortices. As the vortex is formed due to acoustic velocity perturbations, unburned gasses are trapped and convected downstream. When the vortex breaks up, a combustion pulse occurs. This combustion pulse produces a sudden heat release which provides energy to create acoustic motion. When the combustion pulse and acoustic standing waves are in phase, instability can occur [6, 7]. Since vortices can be a key mechanism for instability, a tool such as LES can be very helpful in modeling and understanding these types of instabilities.

2.3 Analytical and Reduced-order Flame Modeling

There has been an enormous amount of analytical and statistical models that have come out over the last 20 or 30 years in this area of flame dynamics. This section will attempt to outline only a few of the most popular or significant modeling approaches. In the late 1980's, Bloxidege et al. came up with some models to predict thermoacoustic instability in afterburner engines. They called this instability "reheat buzz", and their models were based partly on theory and partly on experimental data. This was one of the first studies to come up with a specific model for the dynamic heat release of the flame [8].

Since then, other models have come out with a more physical basis. One very common flame model is based on the kinematics of the flame surface. The model is also sometimes referred to as a flame sheet. There are several different variations of this type of model. One good example of this is the work done by Dowling [9]. Essentially, the flame sheet model is based on the balance of the dynamic flame speed and the dynamic flow velocity.

Another type of flame model is a dynamic well stirred reactor. The well stirred reactor is traditionally used for determining flame blow-off limits. However, Martin at Virginia Tech, developed a variation of this model to predict flame dynamics with the critical parameter being the dynamic flame volume [10]. A similar model was also developed by Annaswamy et al. at MIT [11].

Some other important models that are worth noting might be the mixing model of Lieuwen et al. and the vortex interaction model of Poinsot et al. [7, 12]. The mixing model gives some explanation of how unmixedness or equivalence ratio perturbations can affect stability. The vortex model was explained above where the vortices interact with the flame and consequently the acoustics.

These are just a few of the theoretical or analytical models that exist. Most of the models described above deal mainly with how the flame is modeled and its dynamics. There is less emphasis placed on how the acoustics are modeled. Although, we know that the acoustics are an essential element of the physics associated with thermoacoustic instabilities.

2.4 Acoustic Modeling

In many of the flame studies discussed above, the acoustics have been approximated by a simple straight duct with one end open and one end closed. These acoustic models were simply longitudinal or bulk modal expansions. Some examples of this are given in [1, 6, 8, 9]. An acoustic model that is slightly more complex, but still relatively simplistic, is the transfer matrix model. This approach was taken by Schuermans et al and Pankiewitz et al [13, 14]. In this approach, different components of the combustor are lumped into sub-systems and then combined into an acoustic network. Some good success in modeling industrial size annular combustors has been achieved using this method [15].

In addition to the work done and presented in this thesis, there has also been some previous combustor acoustic finite element analysis. One example is the work done by Krebs et al. where they looked at the acoustic mode shapes of annular combustion chambers [16]. In addition to this research, interesting work was done by Pankiewitz, et al which coupled the flame and the acoustics together in the finite element model. This was done by combining Dowling's nonlinear flame surface model with the acoustic wave propagation. The tool this research group used is now called COMSOL which is a multi-physics finite element tool with the capability of combining multiple physical analyses [17].

The finite element analysis method as described in the introduction is a powerful and flexible tool which allows you to specify any arbitrary domain, boundary condition, or loading. As seen with Pankiewitz's work, multiple physical processes can be coupled together as well. However, as with any numerical tool, caution must be taken in the modeling process in order to obtain accurate results. In this thesis, the process of modeling a laboratory-scale combustor for cold and hot-acoustics will be carefully explained. In addition, means for simplifying the model are emphasized and methods for validating the model will be discussed. The goal of this work is to provide a methodology that can be used in an academic or industrial setting for modeling the acoustics of a combustor or gas turbine engine.

Chapter 3

3 Finite Element Formulation & Model Development

Finite element analysis, FEA was the method of choice to model the acoustic response of the combustor. The advantage of the FE approach is that, in principal, it can be used for any field problem with no geometric restrictions. Likewise, there are no restrictions on boundary conditions or loading. Any material properties can be implemented. Even multiple physical phenomena or coupled physics problems can be solved. Although, finite element analysis is a very flexible and powerful modeling tool, in real modeling applications, constraints do exist. Many times these constraints are dependent on the FE code that is being utilized, as well as, the computational power available. In commercial FEA, only certain types of elements, sources, and boundary conditions are available.

ABAQUS was the commercial finite element software used in this research. This package was chosen based on its strong element library and solver. It also has the needed flexibility to specify arbitrary boundary conditions and account for a non-homogenous medium. This chapter will discuss the details of how ABAQUS does the acoustic finite element formulation. In addition, general model development in ABAQUS is presented. The purpose of this chapter is to introduce acoustic modeling in ABAQUS in order to get a better feel for its capabilities and limitations. Although ABAQUS was the FE code chosen in this research, much of what is discussed in this thesis can be generally applied to most any finite element code capable of acoustic analyses.

3.1 Acoustic Finite Element Formulation

3.1.1 Weak Form of the Problem

In order better understand the analysis that the finite element software performs, the steady-state finite element formulation will be overviewed. This discussion will serve as a foundation to better understand what the FE code is doing and how sources, boundary conditions, and acoustic damping are treated mathematically in the analysis. To begin the formulation, the constitutive relation for acoustic wave propagation will be used.

$$\frac{\partial p}{\partial \mathbf{x}} + \gamma \dot{\mathbf{u}} + \rho \ddot{\mathbf{u}} = \mathbf{0}, \qquad (3.1)$$

where p is the fluid total pressure, $\mathbf{x}$ is the position vector, $\mathbf{u}$ is the fluid particle displacement vector, and ρ is the density. If we assume that the acoustic pressure is attributed to small pressure perturbations about the mean pressure which varies harmonically, ($p = \overline{p} + p'e^{i\omega t}$, $\mathbf{u} = \overline{\mathbf{u}} + \mathbf{u}'e^{i\omega t}$), Eq. (3.1) reduces to the following form

$$\frac{\partial p'}{\partial \mathbf{x}} - \omega^2 \left(\rho + \frac{\gamma}{i\omega} \right) \mathbf{u}' = \mathbf{0} . \tag{3.2}$$

This equation can now be simplified by defining a complex density term

$$\tilde{\rho} \equiv \rho + \frac{\gamma}{i\omega} . \tag{3.3}$$

The constitutive law for a linear inviscid compressible fluid can also be used to further simplify Eq. (3.2)

$$p = -K \frac{\partial}{\partial \mathbf{x}} \cdot \mathbf{u} , \tag{3.4}$$

where K is the bulk modulus of the fluid. We divide Eq. (3.2) by $\tilde{\rho}$ and combine it with the second time derivative of the constitutive law to obtain a form of the wave equation. This is often referred to as Euler's equation

$$-\omega^2 \frac{1}{K} p' - \frac{\partial}{\partial \mathbf{x}} \cdot \left(\frac{1}{\tilde{\rho}} \frac{\partial p'}{\partial \mathbf{x}} \right) = 0 . \tag{3.5}$$

A weak form for the wave equation can be obtained by multiplying the above expression by a weighting function, δp , and integrating over the fluid domain

$$\int_V \delta p \left[-\omega^2 \frac{1}{K} p' - \frac{\partial}{\partial \mathbf{x}} \cdot \left(\frac{1}{\tilde{\rho}} \frac{\partial p'}{\partial \mathbf{x}} \right) \right] dV = 0 . \tag{3.6}$$

This can be integrated by parts to distribute the derivatives as follows

$$-\int_V \delta p \frac{\omega^2}{K} p' dV + \int_V \frac{1}{\tilde{\rho}} \frac{\partial \delta p}{\partial \mathbf{x}} \cdot \frac{\partial p'}{\partial \mathbf{x}} dV + \int_S \delta p \frac{1}{\tilde{\rho}} \frac{\partial p'}{\partial \mathbf{x}} \cdot \mathbf{n} dS = 0 . \tag{3.7}$$

Equation (3.7) is the weak formulation of the problem [19]. Here, the weak form relaxes second derivative constraints on field variable representation in the problem. This permits a larger solution domain, making it possible to solve acoustic wave propagation problems that might otherwise be unsolvable.

3.1.2 Source Representation

In ABAQUS, there are three types of source terms that can be used for acoustic modeling. These three types of sources are available in most commercial finite element packages: prescribed pressure, volumetric acceleration, and reactive sources.

The simplest type of source that can be represented is a prescribed pressure source, S_p. For this source, the value of the acoustic pressure, P_o, is prescribed at a given location. This can also be used to specify a boundary condition.

Volumetric acceleration, S_a**,** is the second type of source which is available. This type of source is implemented in the model by prescribing the integral of the inward acceleration, a_o. The acceleration of the acoustic medium is evaluated over the surface area, *S*, at a given node or node set. In addition, it can be thought of as prescribing the normal pressure gradient at the surface divided by the mass density. This source is also referred to as a surface traction

$$T_a(x) \equiv -\frac{1}{\rho}\frac{\partial p'}{\partial \mathbf{x}} \cdot \mathbf{n} = \mathbf{n} \cdot \ddot{\mathbf{u}} = a_o . \qquad (3.8)$$

Lastly, a reactive source, S_z, is a prescribed linear relationship between the acoustic pressure and its normal derivative. This can also be used to produce a reactive acoustic boundary condition, Z_o, which is also referred to as an impedance or admittance. The mathematical expression for this source is given as

$$T_r(x) \equiv -\left(\frac{i\omega}{c} - \frac{\omega^2}{k}\right) p' . \qquad (3.9)$$

Therefore, if we add all of these source terms to our weak formulation, the complete variational statement then becomes the following

$$-\int_V \delta p \frac{\omega^2}{K} p' dV + \int_V \frac{1}{\tilde{\rho}} \frac{\partial \delta p}{\partial \mathbf{x}} \cdot \frac{\partial p'}{\partial \mathbf{x}} dV - \int_{S_a} \delta p a_o dS - \int_{S_z} \delta p \left(\frac{i\omega}{c} - \frac{\omega^2}{k}\right) p' dS = 0 . \qquad (3.10)$$

In this work, the volumetric acceleration was used as the source. Justification for this choice is shown in Chapter **7**.

In order to gain more insight into our choice to represent the acoustic source, we consider only a volumetric acceleration source and rewrite Eq. (3.10) in its differential form

$$-\frac{\omega^2}{K} p' - \frac{1}{\rho} \frac{\partial}{\partial \mathbf{x}} \cdot \frac{\partial p'}{\partial \mathbf{x}} - a_o = 0 . \qquad (3.11)$$

This equation can be further simplified by utilizing the wave number, *k*

$$\frac{\partial}{\partial \mathbf{x}} \cdot \frac{\partial p'}{\partial \mathbf{x}} + k^2 p' + \rho a_o = 0 , \qquad (3.12)$$

If we compare the wave equation in Eq. (3.12) with a wave equation having a general volumetric body force, the following mathematical relationship can be identified.

$$-\frac{\partial}{\partial \mathbf{x}} \cdot \mathbf{F} = -\rho \mathbf{n} \cdot \ddot{\mathbf{u}} = \rho a_o . \tag{3.13}$$

In examining the above expression, we find that this source term is typically used to simulate an unbaffled loudspeaker or a vibrating sphere of constant volume similar to a dipole [20].

3.1.3 Damping – Volumetric Drag

The acoustic damping has a very strong impact on the stability of the overall system. Higher damping values will result in a more stable combustor system. There are different approaches to determining the acoustic damping, many of which involve experimental study. There are, however, analytical guidelines for determining the damping. These guidelines are described below. The FE formulation of the problem shown in Eq. (3.10) is defined in terms of a complex density. This complex density is defined with a quantity called the volumetric drag, γ, shown in Eq. (3.3) as

$$\tilde{\rho} \equiv \rho + \frac{\gamma}{i\omega} .$$

Volumetric drag can be characterized from the shear viscosity, μ and the bulk viscosity, η

$$\gamma = \frac{\omega^2 \rho}{\mathrm{K}} \left(\eta + \frac{4}{3} \mu \right). \tag{3.14}$$

This model assumes a thermoviscous medium and Kinsler and Frey show that Eq. (3.14) can be broken down into the following form

$$\gamma_T = \gamma_c + \gamma_w + \gamma_{wk} , \tag{3.15}$$

were the first term γ_c is related to the viscous and thermal absorption coefficients. In addition, γ_w and γ_{wk} are related to viscous wall losses. These terms can be expanded to give the relationship

$$\gamma_T = \frac{\omega^2}{c^2} \left(\frac{4}{3} \mu + \left(\frac{\left(C_p / C_v - 1 \right) \kappa}{C_p} \right) \right) + \frac{1}{r_o \rho} \left(\frac{2 \mu \omega}{\rho} \right)^{1/2} \left(1 + \frac{C_p / C_v - 1}{\sqrt{\mu C_p / \kappa}} \right). \tag{3.16}$$

To provide a feel for the properties at atmospheric room temperature conditions, Table 3.1 lists the key properties used for the volumetric drag [20].

Table 3.1: For T = 20°C and $\overline{P}$ =1atm

Shear viscosity (μ)	1.85E-5 ($Pa \cdot s$)
Heat Conduction (κ)	0.0263 ($W/(m \cdot K)$)
Density (ρ)	1.21 ($\mathrm{kg/m^3}$)
Specific heat at constant pressure (C_p)	1.01E3 $J/(kg \cdot K)$
Specific heat ratio (C_p / C_v)	1.402
Speed of sound (c)	343 (m/s)
Prandtl Number (Pr)	0.710

3.2 Finite Element Model Development

The mathematical formulation for acoustic analysis has been described above. We can now discuss how the mathematics can be applied under a finite element framework. Since ABAQUS was the FE tool used in this research, some emphasis will be placed on modeling within the ABAQUS environment. However, the implementation discussed below is fairly general and is easily adapted to almost any finite element software.

3.2.1 Define Geometry

The first step when beginning a model is to define the geometry or the spatial domain. This is a key step in the modeling process and can be very time consuming. First, we need to consider the dimensionality of the model: 1-D, 2-D, 3-D, or axisymmetric. There are obvious tradeoffs with the choice of dimensionality. In general, this choice should be determined based on the geometry and physics of the problem. In addition, it is not advisable to model every geometric detail of the actual system. This is because the smallest feature in the geometry usually dictates the mesh size and consequently the run time. Therefore defeaturing the model as much as possible is an important step.

In some cases, the ability to import CAD files can be important. Many of the Commercial FE codes have the capability of importing geometry from different CAD packages in a neutral file format. Some commercial codes such as ANSYS even have defeaturing options to get rid of some of the unnecessary details in the model. However, many codes do not have this capability and therefore the CAD models would need to be defeatured within the FE program environment.

3.2.2 Define Material

The next step is material property definition. In this case, only the properties of the fluid subvolumes need to be defined. There are multiple ways in which this can be done. In this research, we assumed that the medium was a homogenous fluid with an equivalent density and bulk modulus. In other codes, one might specify the speed of sound rather than the bulk modulus.

Since these acoustic properties are highly temperature dependent, the heating effects of the flame must be accounted for. In this research, the material properties were tabulated with respect to temperature. This way, when the temperature gradient was prescribed in the model, the correct fluid properties could be mapped by interpolating the tabulated properties. Temperature dependence will be discussed further in Chapter 6.

3.2.3 Assemble Parts

When dealing with large and complex systems, there is a great need for breaking the system down into subsystems which can be independently modeled and verified prior to exploring the complete system response. It is much easier to develop and verify simpler geometries for each fluid sub-section independently. This allows much higher productivity and reduces the model error. In addition, some subsystems have an important role in the overall acoustic response of the combustor and must be represented well. Other subsystems do not directly interact with the acoustic response of the combustor. For these subsystems, it may be adequate to minimally represent them or eliminate them all together.

ABAQUS has a very good subcomponent modeling capability which can be used to partition each of the fluid volumes and create controlled meshes. ABAQUS can instance the sub-models into position in the overall assembly and mesh each sub-model individually. Once in the correct position, ABAQUS can unite two surfaces through a tie command.

3.2.4 Mesh Part

As mentioned above, the parts can be individually meshed and then assembled. One can either use free meshing or mapped meshing options depending on how tailored the mesh needs to be. One nice attribute within many FE codes is the biased mesh option. This provides the option of a denser mesh in critical regions of the model and a sparser mesh in other regions.

In any finite element analysis, convergence studies should be performed to ensure that the solution has converged. In addition to this, for dynamic modeling there are general guidelines that can be used as a starting point when converging the mesh. Just as the Nyquist–Shannon sampling theorem provides guidelines to avoid temporal aliasing, there are also guidelines to avoid spatial aliasing. As a general rule of thumb, when reconstructing a waveform using linear elements, a minimum of 5 nodes for every half of a sine wave is required. Therefore if one is interested in the 10^{th} acoustic mode, at least 50 nodes would be needed to reconstruct that mode shape. In addition, more nodes might be needed to accurately capture aspects such as temperature gradients caused by the flame.

3.2.5 Analysis Type

The type of analysis needed is not always clear. In the case of acoustic modeling, one could perform a modal, steady-state, or transient analysis. The choice is generally dictated by the type of information one needs from the model. In this research, frequency response functions were needed. Therefore, a frequency domain or steady-state analysis was chosen. Since most acoustic properties and boundary conditions are defined in the frequency domain, a steady-state analysis is a convenient choice.

If the flame dynamics and acoustics were modeled together, a closed-loop transient analysis would likely be needed. Lastly, the modal analysis might be a good choice if we wanted to check the behavior and validity of our model. Such a check will be explained in more depth in Chapter 5.

3.2.6 Assign Boundary Conditions

The specification of the boundary conditions (BC's) in the acoustic finite element model will strongly affect the acoustic field at any location in the model. Therefore, defining the boundary conditions is an essential step for achieving accurate results. In order to solve any finite element problem, one must first determine where the boundaries will be and what condition to place on those boundaries. In the case of this research, only the combustor region of the gas turbine engine was modeled. Modeling only this section of the engine allows for a much simpler model with sufficient accuracy as long as the boundary conditions are specified correctly.

The most common approach to specifying a boundary condition is to prescribe a complex impedance at each surface. Much like its electrical system analog, impedance has resistive and reactive components. The impedance can vary over the surface, or one might specify an average impedance over the surface (depending on the application). If the impedance is specified appropriately, it can completely characterize the effect of both the compressor and turbine on the combustor acoustics.

The determination of the impedance can be difficult and is not part of the scope of this thesis. More research is needed in order to determine the best method for resolving these impedances. However, it should be noted that there has been some research performed in experimentally measuring the boundary condition impedance on industrial size gas turbine engines [18].

In ABAQUS we can specify an arbitrary impedance through the following relationship.

$$\dot{u}_{out} = \left(i\frac{\omega}{k_1} + \frac{1}{c_1} \right) p = \frac{1}{Z(\omega)} p, \tag{3.17}$$

where ω is the angular frequency. The spring and dashpot properties, k_1 and c_1 respectively are defined per unit surface area. The term $1/Z(\omega)$ is called the complex admittance, and $Z(\omega)$ is called the complex impedance. Therefore, to specify a complex impedance or admittance, one only needs to enter the values of $1/c_1$ and $1/k_1$ for each angular frequency of interest. The impedance is applied to a node in 1-D, an element edge in 2-D, and to an element face in 3-D [19].

3.2.7 Assign Loading

Lastly, before running a FE model, the proper load must be established. In this case, the flame must be represented as an acoustic source. The different types of possible sources were mathematically described in Section 3.1. The three different sources were prescribed pressure, volumetric acceleration, and reactive sources. In Chapter **7**, it will be shown that the heat release perturbations of the flame can be related to a volumetric acceleration source. This is very convenient since most FE codes which are capable of acoustic analysis are also capable of representing a volumetric acceleration.

So far, we have discussed the finite element mathematical formulation and modeling guidelines in a very general sense. In the following chapter, more detail will be given toward the modeling effort performed in this research.

Chapter 4

4 Cold Acoustic Model

In this chapter, the modeling of the combustor acoustics will be examined without the flame. This produces simpler models which can be explored and validated before adding the complexity involved with the flame.

4.1 Motivation

The acoustic finite element formulation and general model development was explained in the preceding chapter. However, to build an acoustic model which incorporates all of complex geometries associated with a gas turbine engine is many times not possible and certainly not practical. Even with a simple laboratory combustor, we will find that there still exist complex geometries and boundary conditions that are difficult to model. Without simplifying the modeling effort further, accurate results will be difficult to obtain. Consequently, one of the main focuses of this research has been to simplify the models as much as possible while still maintaining accurate results.

4.2 Application to Laboratory-Scale Combustor

In order to have a tractable system and be able to compare our models with real experimental data, the majority of the research was performed on a laboratory combustor at Virginia Tech's Active Combustion and Control laboratory. A picture of the test apparatus is shown below in Fig. 4.1. In addition, Table 4.1 shows the specifications for the combustor. This laboratory rig is a swirl stabilized dump combustor which is meant to represent a single injector flame in the annulus of an industrial combustor. This of course simplifies the research by looking at a single flame rather than 18 or more flames distributed around the annular combustion liner.

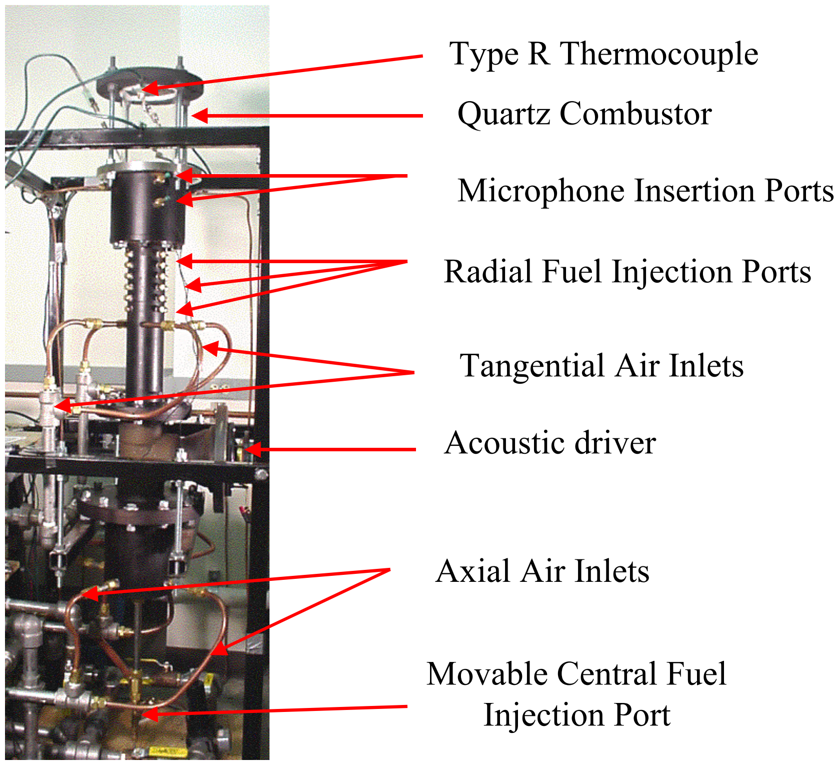

Fig. 4.1: The VACCG Laboratory-Scale Combustor

Table 4.1: Specifications for VACCG Laboratory-Scale Combustor

Combustor Type	Swirl and dump & enables turbulent flame stabilization
Air Flow rate	200 SCFM
Power	400 KW
Reynolds Number	100,000 max
Swirl Number	0.4-1.8
Pressure	Atmosphere to 10 bar

Throughout the remainder of this thesis, much of the finite element modeling effort will use this turbulent premixed gas combustor shown in Fig. 4.1. This gives us a system which we can model and then verify through experiments. It should also be noted that some of the FE results presented later include an extended section downstream of the flame. This was added to allow the system to go unstable at certain operating conditions and will be discussed later on.

4.3 1-D FE Acoustic Model

One major area of simplification was to reduce the dimensionality of the models from 3-D to 1-D. Consequently, the complex and non-symmetric cross-sections were lumped into an equivalent cross-sectional area, and the acoustics were only allowed to propagate in one dimension. This type of one-dimensional acoustic wave propagation is commonly referred to as plane wave or longitudinal wave propagation.

To illustrate the amount of simplification obtained by changing the dimensionality from 3-D to 1-D, we can compare a 3-D and 1-D model of the laboratory combustor. The 3-D version of the combustor was done by Alok Dhagat, another member of the VACCG. A section of the laboratory combustor directly upstream of the flame is shown in Fig. 4.2. From the comparison of the drawings in Fig. 4.2, it is simple to observe that it would be significantly easier to build a 1-D model. In addition, from the specifications listed below the images, it can be seen that the 1-D model greatly reduces the computation time.

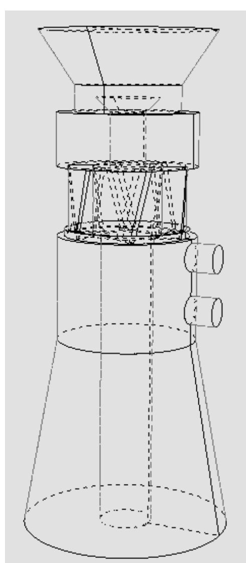

3-D model

- Degrees of Freedom = 150,000
- Computational time = 24 hours
- Captures acoustic response

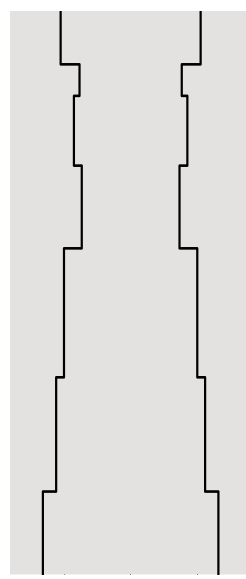

1-D model

- Degrees of Freedom = 150
- Computational time = 30 sec.
- Captures acoustic response

Fig. 4.2: Comparison between 3-D and 1-D acoustic models

It turns out that the one-dimensional plane wave assumption not only simplifies the modeling effort, it is also accurate in the lower frequency range which is the typical frequency range of interest for thermoacoustic instabilities. At low frequencies, only plane or longitudinal waves propagate along the length of the combustor. The plane wave assumption is valid until a critical frequency is reached, also referred to as the "cutoff frequency". This frequency is based strictly on the diameter or the largest cross-sectional dimension of the combustor. For a circular cross-section, the cutoff frequency is given by the following equation

$$f_c = \frac{1.84c}{\pi d}, \tag{4.1}$$

where c is the speed of sound in the medium and d is the diameter of the combustor. In the case of a rectangular section, the cutoff frequency is

$$f_c = \frac{c}{2}\left(\left(\frac{n_x}{L_x}\right)^2 + \left(\frac{n_y}{L_y}\right)^2\right) \qquad n_x, n_y = 0,1,2,..., \tag{4.2}$$

where the smallest non-zero value of Eq. (4.2) is considered the cutoff frequency and L_x and L_y are the width and height of the cross-section respectively.

Plane waves traveling through a section of the combustor can be modeled as shown in the figure below.

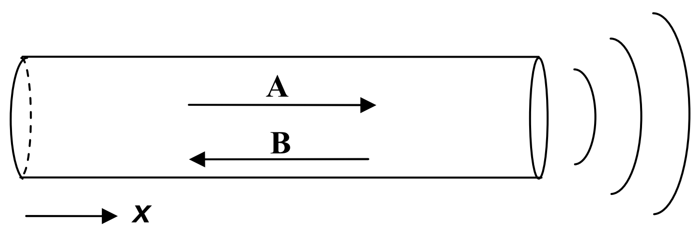

Fig. 4.3: Representation of a plane wave traveling in a section of the combustor

The acoustic pressure and particle velocity can be described in terms of the forward and backward complex wave coefficients A and B

$$p'(x,t) = Ae^{i(\omega t - kx)} + Be^{i(\omega t + kx)}, \tag{4.3}$$

$$u'(x,t) = \frac{1}{\rho c}\left(Ae^{i(\omega t - kx)} - Be^{i(\omega t + kx)}\right). \tag{4.4}$$

In addition, there are two important terms which help to describe how the plane waves travel in the combustor. These terms are the reflection coefficient, R and the acoustic impedance, Z_A

$$R = \frac{B}{A}, \tag{4.5}$$

$$Z_A = \frac{p'}{u'S}, \tag{4.6}$$

where S is the cross-sectional area of the duct. Another important aspect of one dimensional plane wave acoustics that will be discussed in this section is the end correction, l_0. End corrections can be used to approximate various acoustic radiation conditions [20]. The impedance, reflection coefficient, and end corrections will be used to describe various boundary conditions. It should be noted that all of the analytical expressions shown below are only valid if the plane wave assumption holds true.

4.4 Analytical Expressions for Modeling 1-D Acoustics

As mentioned earlier, it is critical that boundary conditions are represented correctly to predict an accurate acoustic response. There are several common boundary conditions and geometries encountered in combustors which have analytical expressions for plane wave analysis. These boundary conditions are described below along with their analytical representation. Fig. 4.4 below shows some of the common boundary conditions and complex geometry found in gas turbine engines and more specifically in the laboratory combustor used in this study. In the following paragraphs, 1-D analytical expressions will be derived for the above boundary conditions and geometries listed in Fig. 4.4.

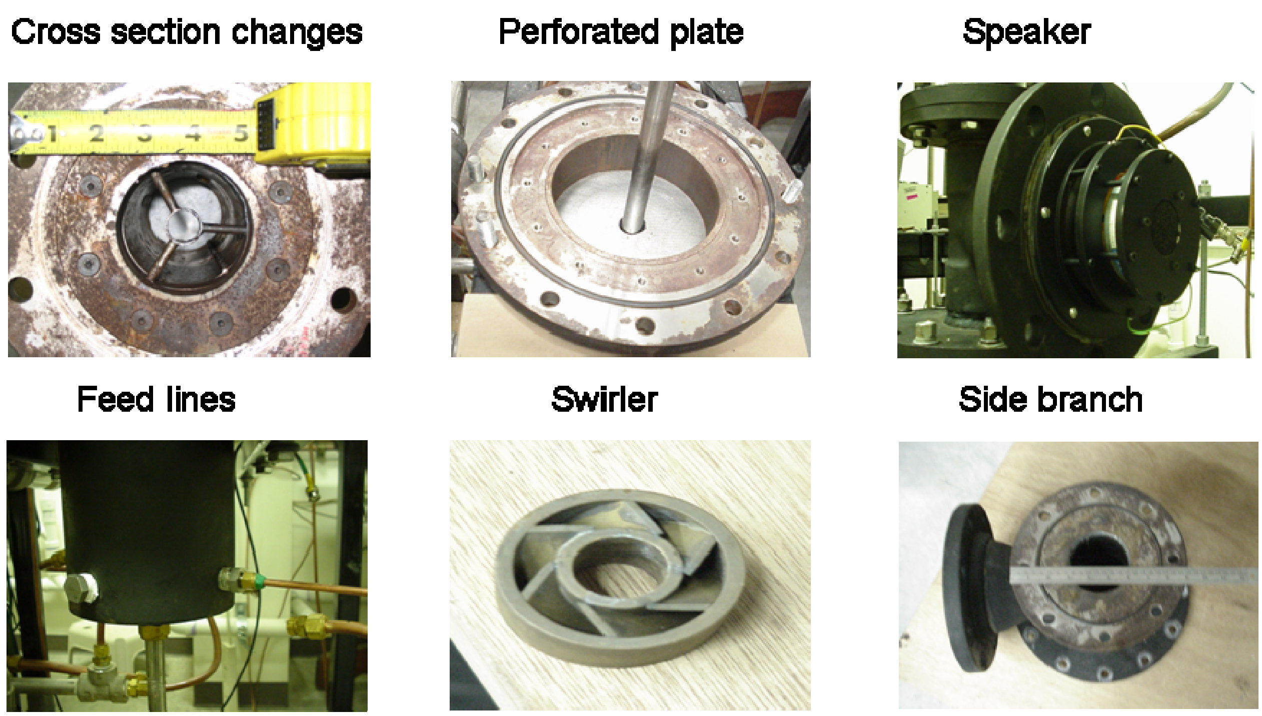

Fig. 4.4: Picture of complex geometries and boundary conditions found on the laboratory combustor

4.4.1 Perforated Plates and Honeycombs

A perforated plate or honeycomb is often used in combustors to straighten the flow and eliminate vortices and other complex flow structures. Fig. 4.5 shows a schematic drawing for a section of perforated plate. The dashed lines show the effective length, l which the acoustic waves see. The equation for the effective length is given below. The mathematical expressions that follow for the perforated plate were taken from Pierce [21].

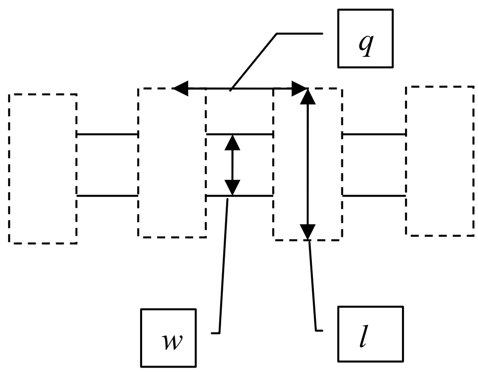

Fig. 4.5: Cross-sectional view of a perforated plate

To start, we can look at the complex impedance for a perforated plate

$$Z_A = \frac{1}{N\pi a^2}\left(j\rho c \tan(kl(1-M)) + R_A A \right). \tag{4.7}$$

where N is the number of holes, R_A is the acoustic resistance, A is the area of a single hole, and M is the mach number. Now, if one examines the impedance of an orifice, we obtain the following expression

$$Z_A = R_A + j\frac{\rho c}{A} kl(1-M)\,. \tag{4.8}$$

Comparing Eq. (4.7) and Eq. (4.8) we see that these two expressions differ by a tangent term. For small angles, $\tan\theta = \theta$ and Eq. (4.7) and Eq. (4.8) become identical. This means that when the quantity kl is small ($kl \ll \pi/2$), a perforated plate can be treated as an orifice plate with an equivalent cross-sectional area and an equivalent thickness given in the equation below

$$l \approx w + \frac{16a}{3\pi}(1-1.25\xi_o)(1-M)^2\,, \tag{4.9}$$

where a is the radius of the hole, and ξ_o is the ratio of orifice diameter to duct diameter. In this study we have assumed the Mach number term is negligible. Although there is a finite mean flow, typically if the Mach number is less than 0.1, mean flow effects can be neglected in the acoustic analysis. In this research and many power generating gas turbine engines, this is a safe assumption.

This simplification is significant because instead of modeling thousands of tiny holes, one can simply model a single hole with an equivalent open area and adjusted thickness. This analysis is specifically valid for perforated plates, but could also be utilized for thin honeycombs. For a thicker honeycomb, a simple equivalent cross-sectional area without an effective length would be better suited [21].

4.4.2 Side Branches

Another commonly found geometric feature are side branches which can also be referred to as quarter wave tubes or Helmholtz resonators in acoustic terminology. Fig. 4.6 show a simple example of a side branch. On a combustor, side branches could represent air or fuel lines or a number of other features.

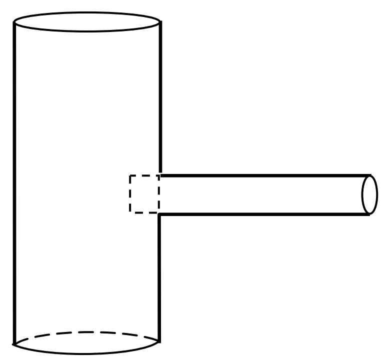

Fig. 4.6: Image of a side branch or a quarter wave tube

An often overlooked aspect when modeling side branches is the end correction associated with the acoustic wave radiating out of the side branch. This end correction can be expressed as shown below

$$l_0 = \frac{8a}{3\pi}(1 - 1.25\xi_{SB}), \tag{4.10}$$

where ξ_{SB} is the ratio of the diameter of the side branch to the diameter of the combustor cross-section. The expression for the effective length, l_0, remains valid as long as the ratio, ξ_{SB} is below a value of 0.6.

4.4.3 Open Boundary Condition

Another common boundary condition in which the effective length is useful in modeling is the open termination. This is typically applicable in all combustors or gas turbine engines since there is always an entrance and an exit. When an acoustic wave sees the end of a duct, part of the wave will be reflected back due to the sudden change in impedance. This change in impedance is due to a plane wave just before the exit and a spherically evanescent wave just after the exit. A wave with a low frequency will reflect significantly, and can be defined by its effective length or impedance. Fig. 4.7 shows the representation of the open termination.

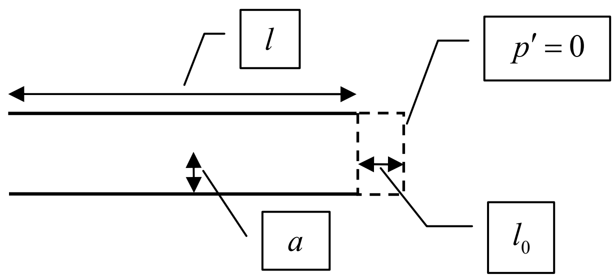

Fig. 4.7: Representation of an open boundary condition

The easiest way to model the open condition is to simply use an end correction and specify the pressure equaling zero after the end correction. The end correction for an unflanged open termination is given as

$$l_0 = 0.61a, \tag{4.11}$$

where a is the radius. Consequently the overall or equivalent length is

$$l_{eq} = l + 0.61a. \tag{4.12}$$

As an alternative one could also specify impedance of the unflanged open boundary condition [20]

$$Z_A = \frac{\rho_o c}{S}\left(\frac{1}{4}(ka)^2 + j0.6ka\right). \tag{4.13}$$

4.4.4 Rigid Termination

At a rigid termination, the acoustic particle velocity is zero. It can be shown from Euler's equation that particle velocity equaling zero is equivalent to the gradient of pressure equaling zero

$$\rho\frac{\partial u'}{\partial t} = -\frac{\partial p'}{\partial x}. \tag{4.14}$$

Assuming a steady-state solution, this expression simplifies to the following

$$u' = \frac{i}{\omega\rho}\frac{\partial p'}{\partial x}. \tag{4.15}$$

Since the boundary condition at a rigid wall is that particle velocity equal zero. This means that the gradient of pressure is also equal to zero

$$\frac{\partial p'}{\partial x} = 0. \tag{4.16}$$

When using commercial finite element codes such as ABAQUS, the acoustic velocity or gradient of the pressure equaling zero is the default boundary condition.

4.4.5 Change in Cross-Sectional Area

Changes in cross section make a significant impact on the acoustic response. To see this, let us examine the simple expansion in cross-sectional area shown below in Fig. 4.8

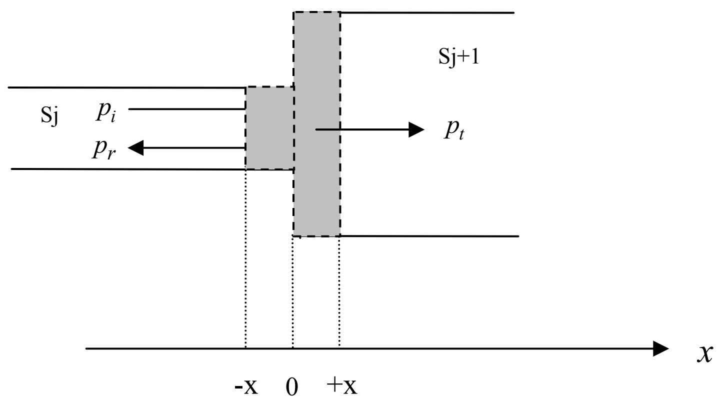

Fig. 4.8: Schematic of a duct undergoing a change in cross-section

To analyze change in area, we can use the linearized continuity equation and the momentum equation shown below respectively [20]

$$\frac{1}{c^2}\frac{\partial p'}{\partial t} + \rho\frac{1}{S}\frac{\partial}{\partial x}\left(Su'\right) = 0, \tag{4.17}$$

$$\rho\frac{\partial u'}{\partial t} + \frac{\partial p'}{\partial x} = 0. \tag{4.18}$$

Integrating the above equation from *–x* to *+x* and taking the limit where *–x* and *+x* go to zero, we obtain the following jump conditions

$$S_{j+1}u'_{j+1} = S_j u'_j, \tag{4.19}$$

$$p'_{j+1} = p'_j. \tag{4.20}$$

Eqs. (4.19) and (4.20) then imply that the pressure and volume flow is conserved through the interface while the acoustic particle velocity is not

$$u'_{j+1} = \frac{S_j}{S_{j+1}} u'_j . \tag{4.21}$$

The acoustic impedance can be stated as follows

$$Z_A = \frac{\rho c}{S} \frac{P_i + P_r}{P_i - P_r} , \tag{4.22}$$

where P_i and P_r are the complex incident and reflected pressure wave magnitudes respectively. As a special case, when the section in the figure above has an anechoic termination and no changes in cross-section the impedance becomes

$$Z_A = \frac{\rho c}{S} . \tag{4.23}$$

The acoustic impedance can be determined by using continuity or pressure and volume velocity along the entire combustor. However, any useful finite element code already takes these effects into consideration. Therefore, one must simply specify the changes in the cross section accurately.

4.4.6 Speaker Boundary Condition

Speakers are commonly found on laboratory combustors for the purpose of dynamically manipulating the mass flow rate. On industrial gas turbine engines, a speaker probably would not be present. However, other non rigid boundaries with elastic behavior similar to a speaker may exist and must be accounted for properly. In the lower frequency range, a non-rigid boundary such as a speaker can be approximated with a single degree of freedom mass spring damper system. Using Newton's second law of motion we get the following expression

$$m\ddot{x} = -b\dot{x} - kx + Sp' + F . \tag{4.24}$$

where in this case, x is the speaker displacement, and F is the driving force. Assuming simple harmonic motion and that the speaker is not being driven, the mechanical impedance can be expressed as

$$Z_{md} = b + j(\omega m - k/\omega) , \tag{4.25}$$

where b is the damping constant, k is the spring constant, and m is the mass of the speaker. This can be converted to acoustic impedance by dividing by the square of the cross-sectional area, S^2

$$Z_A = \frac{1}{S^2}\left(b + j(\omega m - k/\omega)\right) . \tag{4.26}$$

The parameters *b*, *k*, and *m* can be determined experimentally through a fiber optic probe to measure speaker displacement at specified voltage inputs. The picture below shows the experimental set up for the speaker characterization. There are several different methods which can be used.

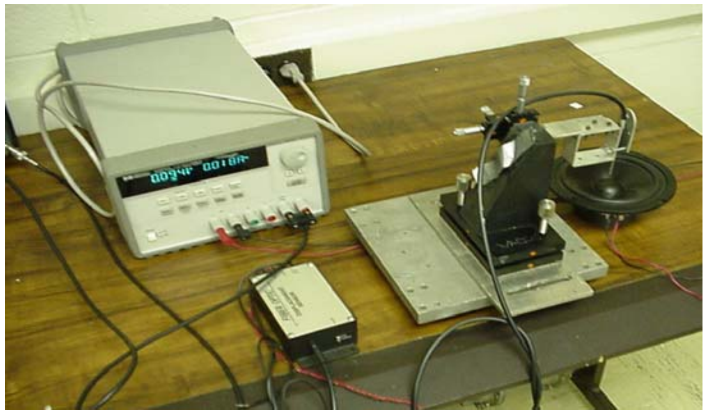

Fig. 4.9: Experimental setup for speaker characterization

As an example, the speaker that is used to excite the test rig for this project has the following properties: k = 682.75 N/m, m = .006812 Kg, and ζ = 0.33. The damping is defined as

$$b = 2\zeta\sqrt{km}\ , \tag{4.27}$$

and therefore b = 1.423. The above properties were experimentally determined previously by another member of VACCG, Alok Dhagat.

Table 4.2 shows a summary of the analytical expressions and treatment of boundary conditions for various geometries. From these analytical expressions, many geometric features can be easily represented in the 1-D FE model. There can be situations, particularly with non-rigid boundary conditions, where experimental means are necessary to obtain the proper boundary condition. The optical technique discussed above is just one of many techniques used to characterize the impedance of these boundary conditions. Another common means for measuring impedance is the plane wave tube technique [22].

Table 4.2: Summary of common boundary conditions and geometries

Configuration	Boundary Condition	Impedance	End Correction	Natural Frequency
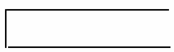	Open $p'=0$	$\frac{\rho_o c}{S}\left(\frac{1}{4}(ka)^2 - j0.61ka\right)$	$0.61a$	NA
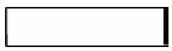	Rigid	∞	NA	NA
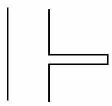	$u'=0$ Side Branch	NA	$\frac{8a}{3\pi}(1-1.25\xi)$	NA
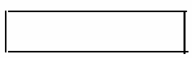	Thin Plate	$-i\omega\rho_p w$	NA	$0.47\frac{w}{a^2}\left(\frac{E}{\rho(1-\nu^2)}\right)^{1/2}$
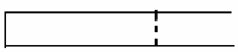	Perforated Plate	$\frac{j\rho c}{N\pi a^2}\tan\left(kw+\frac{16ak}{3\pi}(1-0.43a/q)\right)$	$\frac{8a}{3\pi}(1-0.43a/q)$	NA
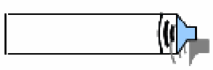	Speaker	$\frac{1}{S^2}\left(c + j(\omega m - k/\omega)\right)$	NA	$\frac{1}{2\pi}\sqrt{\frac{k}{m}}$

4.5 Cold Acoustic 1-D Model Exploration

Because of the greatly reduced computation time, we were able to vary parameters and see the impact on the overall acoustic response. We found that the large sidebranch where the speaker was mounted had a very large impact on predicting the 2nd and 3rd acoustic resonance peaks. We also found that the feedlines had a very small contribution to the overall acoustic character of the system. Therefore some of the feedlines were actually eliminated from the model. Another important factor was found to be the honeycomb/perforated plate section. This had a strong effect on the higher acoustic modes. Therefore we took great care in developing an equivalent cross-sectional area reduction as discussed in Section 4.4.

The overall length of the combustor was another key factor. So, determining an equivalent length as carefully as possible was a concern. Again because we simplified our model, we are much more able to explore it and determine the key geometric features.

Chapter 5

5 Validation of Cold Acoustic Model

As with any finite element model, validation of the model is a vital step. There are several methods that were utilized to validate the cold acoustic model. These methods involved checking the cold acoustic finite element results with both simple analytical solutions, as well as, reconciling the finite element model with experimental data.

5.1 Mode Shape Validation

The first method of validation is a comparison of the acoustic mode shapes. Mode shapes are the dominant standing wave patterns of the combustor and occur at the natural frequencies of the combustor. Mode shape comparison is generally the first check that should be done since it is quick and easy. This comparison is made by approximating the combustor as a straight duct with either open or closed ends. In the case of our laboratory combustor, we have the upstream-end closed and the downstream-end open. The analytical expression for the natural frequencies and mode shapes for the open-closed duct case are given below

$$f_n = \frac{(2n-1)c}{4L}, \tag{5.1}$$

$$\text{mode shape} = \cos\left(\frac{2\pi f_n L}{c}\right). \tag{5.2}$$

Table 5.1 and Fig. 5.1 show the natural frequencies and mode shapes of the analytically solved open-closed duct compared to the FE results of the laboratory combustor. From these comparisons, one can see that the "back of the envelope" analytical solution gives you a good check to see if your model is in the ball park. There is another simple rule of thumb that should be considered when comparing the simple analytical solution to the finite element solution. When abrupt changes in cross-sectional area are present, the actual natural frequency of the combustor will typically be lower than the natural frequencies calculated in Eq. (5.1) [6].

Table 5.1: Comparison of analytical and finite element natural frequencies

Mode Type	f_n Analytical Straight Duct Modal Solution	f_n Finite Element Modal Solution
¼ wave	69	42
¾ wave	207	186
5/4 wave (starting at side branch)	389	378
7/4 wave	482	459

The comparison shown in Fig. 5.1 is also useful to determine where modes of the FE model deviate from the simple duct model. Noting where deviations occur in relation to combustor geometry can be helpful in determining the contributions and couplings of geometric subsystems to the overall acoustic response. For example, one can see from the figure below that there are a couple of dramatic changes in cross-sectional area that have a large impact on the acoustic response. The side branch also has a significant impact on the 5/4 and 7/4 wave. Knowing that these are some key geometric features of the model, we can focus on making sure that we model these regions carefully and account for subtle but significant details such as the end correction discussed in the previous chapter.

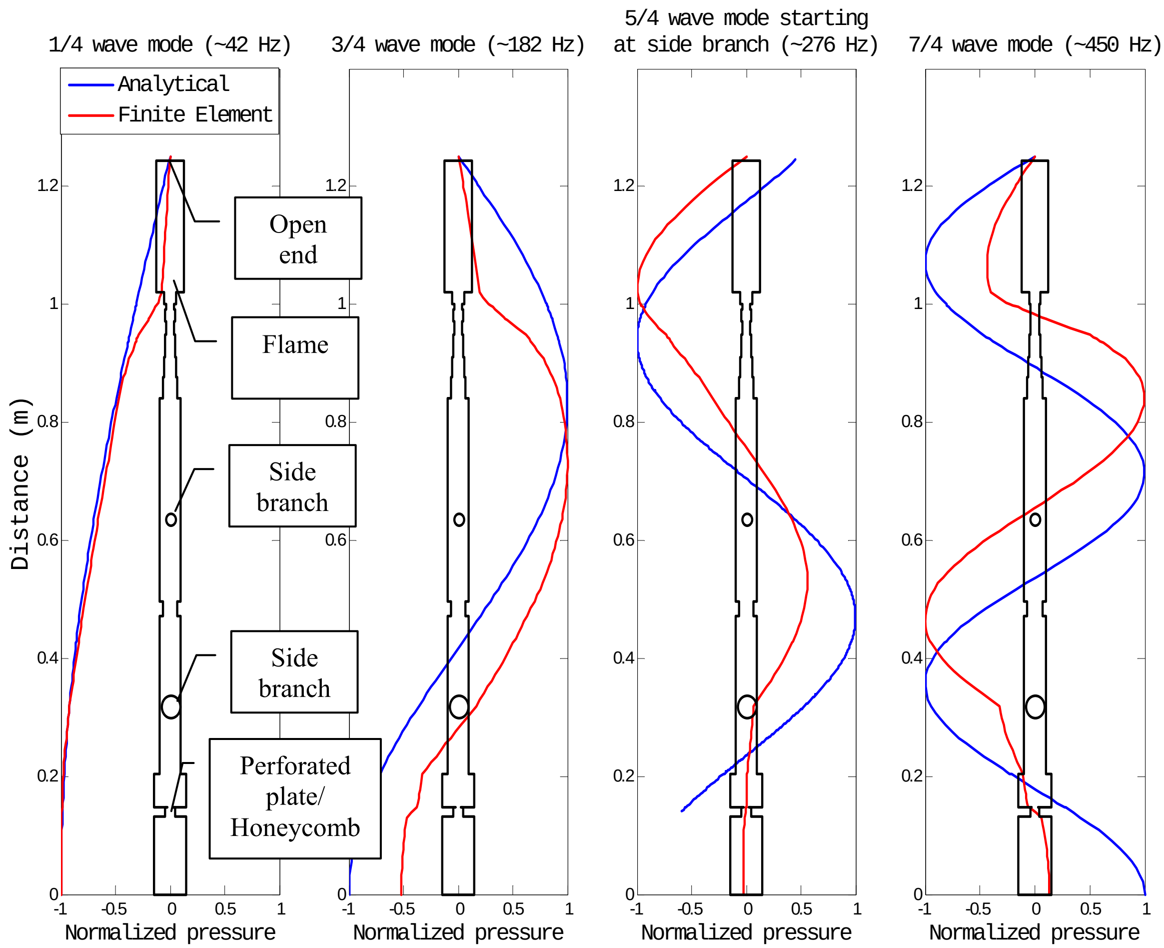

Fig. 5.1: Comparison between analytical and finite element acoustic mode shapes

Once the quick checks have been completed and the model refined, a comparison of the mode shapes and natural frequencies can be made between the FE results and the actual experimental results. This comparison is shown below in Table 5.2 and Fig. 5.2.

Table 5.2: Comparison of finite element and experimental resonance frequencies

Mode Type	f_n Finite Element Modal Solution	f_n Experimental Measurement	% Difference b/w Exp. and FE.
¼ wave	42	42	0.00
¾ wave	186	182	2.20
Longitudinal mode coupled w/ side branch	254	254	0.00
5/4 wave (starting at side branch)	378	376	0.53
7/4 wave	459	450	2.00

Modes can be visualized by spatially plotting the acoustic pressure at the resonance frequencies since the resonance frequencies are almost identical to the natural frequencies.

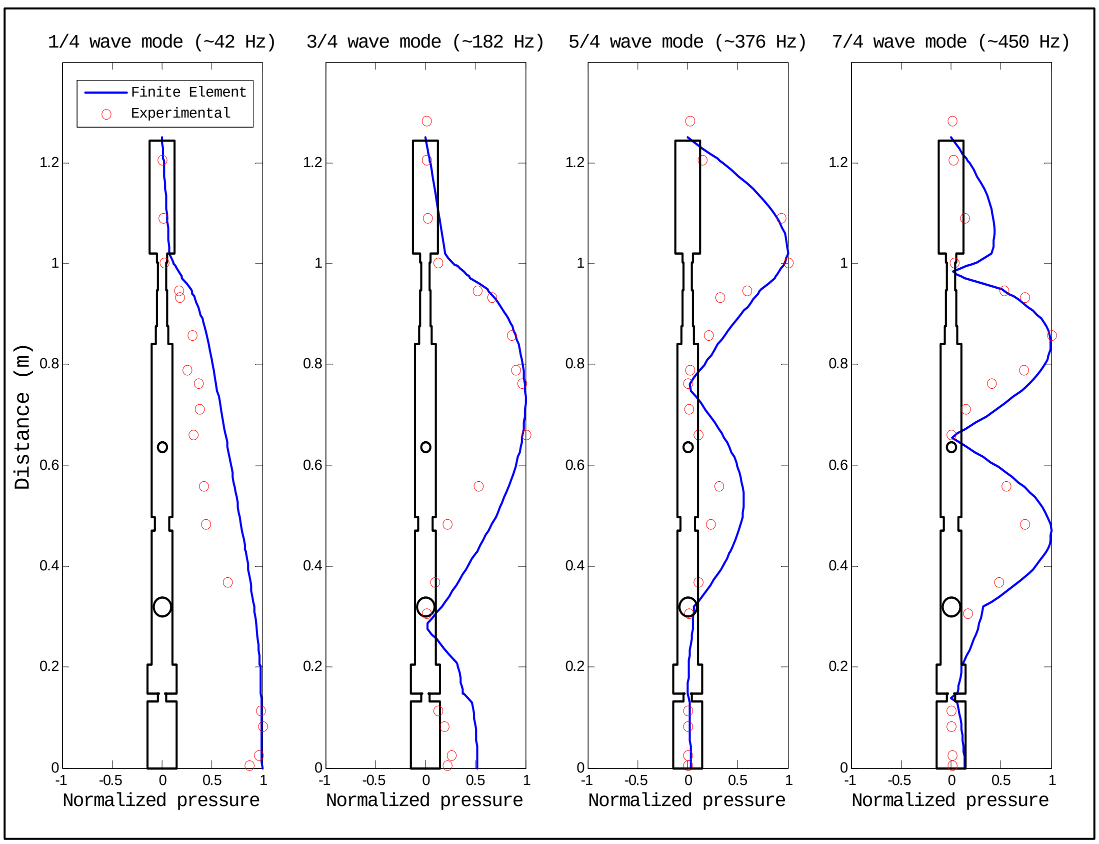

Fig. 5.2: Experimental and finite element mode shape comparison

In measuring the mode shapes experimentally, a speaker excited the combustor from the top and a microphone was attached to a thin rod and fed through the combustor to the different positions corresponding to approximate length-wise location of the red circles in the plot above. It is likely that some of the inaccuracy shown in the plot above is due to the measurement method rather than the FE model. While it is easy to determine the spatial location of "effective microphones" in the finite element model, determining the spatial location of the microphone for the measurements made in the combustor can be tricky. This is likely one of the reason for the differences in the plots. However, in general, the acoustic modes show very good spatial correlation between the experimental measurements and the FE results. This is impressive when one looks at the geometric complexities in the feed lines, swirler, perforated plate, and cross-sectional area changes.

5.2 Frequency Response Validation

Another means for model validation was done by measuring the frequency response function (FRF) of the acoustics at a couple different locations in the combustor. This was an important measurement since the FRF is merely a transformed version of the acoustic transfer functions that is one of the objectives of this study. The difference between the two functions is that the acoustic FRF is defined in the frequency domain while the transfer function is defined in the *s* or Laplace domain.

The frequency response was developed by exciting the acoustic waves with a speaker at the top of the combustor, and measuring the acoustic pressure and velocity with microphones at a few different locations. Just like a transfer function, the FRF is defined as the ratio of the output divided by the input for a given frequency range. In this case, the output was the acoustic pressure or velocity. The input was the speaker acceleration which was measured by placing an accelerometer on the speaker diaphragm. Fig. 5.3 shows the measurements involved in the FRF.

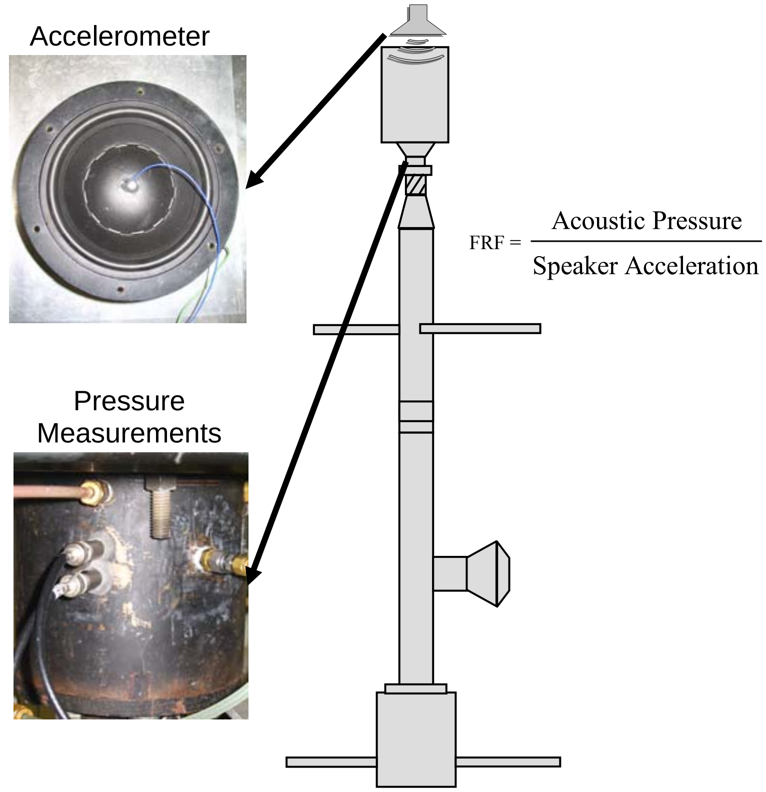

Fig. 5.3: Frequency response function measurements with acoustic pressure as the output and speaker acceleration as the input

The frequency response functions at various locations in the combustor were measured and compared to those taken from the FE model. The frequency response was determined at two specific locations, 3 ½ inches and 1 ½ feet upstream of the flame location. These locations were chosen because they represent the "Acoustics at Flame" and "Acoustics at Fuel Lines" FRF's or transfer functions needed for the closed-loop model (see Fig. 1.1). In both cases, the speaker was placed at the top of the combustor near the spatial location of the flame. An accelerometer was mounted to the speaker, and the output for the accelerometer acted as the input for the measured frequency response function. For the output, both pressure and velocity were measured. The pressure was measured using high-precision PCB microphones, and the velocity was measured using the two-microphone technique. The two-microphone technique determines the velocity by using the pressure gradient obtained by taking the ratio of the change in pressure over the distance between the two microphones

$$U(f) \cong \frac{i}{\omega\rho\Delta r}\left(P_2(f) - P_1(f)\right), \tag{5.3}$$

where r is the distance between the two microphones which was about two inches. The capital P and U represent the Fourier Transform of pressure and velocity respectively. Appendix A shows a more detailed description of the mathematics and signal processing that goes into determining the acoustic velocity.

In the following plots, magnitude is in dB determined by(A,1)

$$dB = 10\log\left(\frac{output}{input}\right), \tag{5.4}$$

relative phase in degrees, and coherence are plotted. The magnitude reveals the relative amplitude of the output to the input at each frequency. The relative phase angle provides some indication of time lag of the output relative to the input. Lastly, the coherence provides a measure of the correlation between the two signals. The ideal coherence is "1" meaning that the output is perfectly correlated with the input.

The first two comparisons in Fig. 5.4 and Fig. 5.5 show the frequency response 3 ½ inches from the flame location. As can be seen from these plots, both the magnitude and phase of the predicted acoustic FRF's correspond extremely well with the experimental measured FRF's. There is some deviation in the phase. However, this would be expected since the phase is more sensitive to the inherent noise in the measurement.

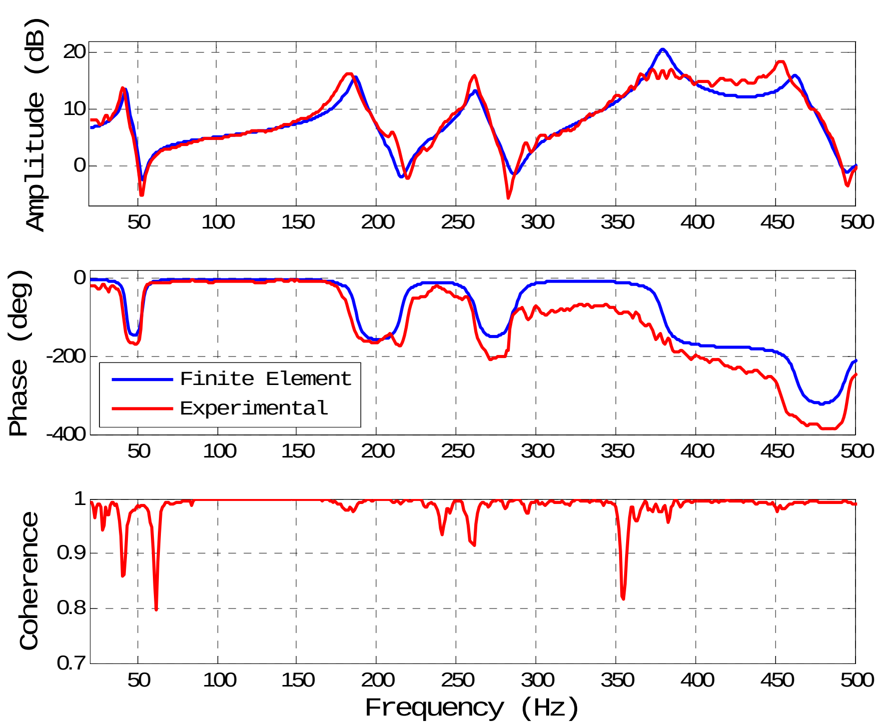

Fig. 5.4: Frequency response of (acoustic pressure 3 inches upstream of flame) /(speaker acceleration)

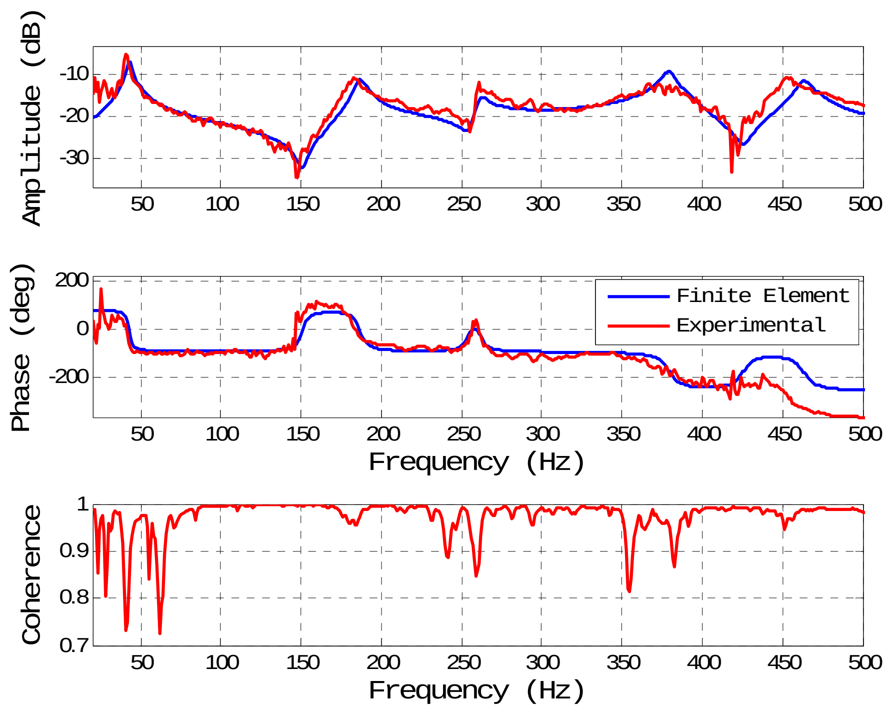

Fig. 5.5: Frequency response of (acoustic velocity 3 inches upstream of flame) /(speaker acceleration)

The second location where the FRF was compared was about a 1 ½ feet below the flame location. Fig. 5.6 indicates that the FE model and the experimental data are very highly correlated.

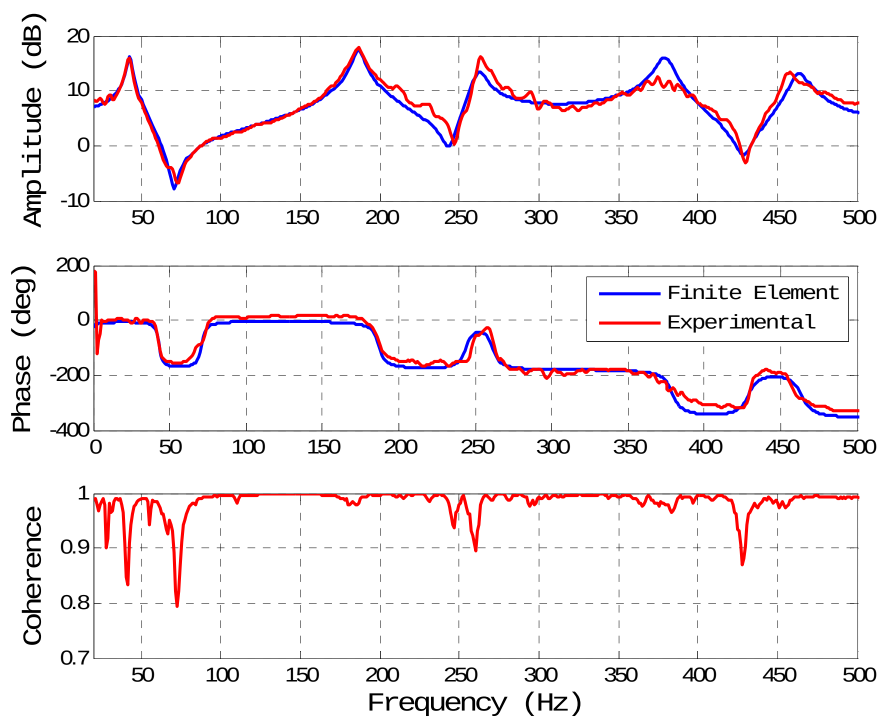

Fig. 5.6: Frequency response of (acoustic pressure 1 ½ feet upstream of flame) /(speaker acceleration)

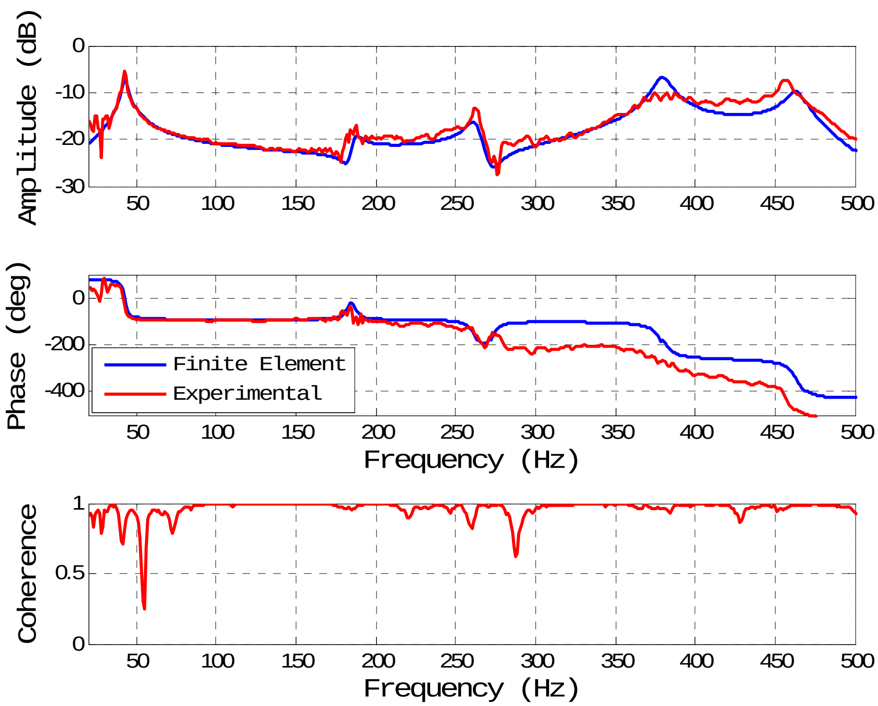

Fig. 5.7: Frequency response of (acoustic velocity 1 ½ ft upstream of flame) /(speaker acceleration)

As clearly seen from the plots above, the FE model does a great job capturing the cold acoustic response. In the following sections, the techniques and lessons presented above for cold acoustic modeling will continue to be utilized.

Chapter 6

6 Hot-acoustics Model

6.1 Introduction and Motivation for Temperature Dependent Acoustics

Temperature impacts both the speed of sound and the density of the medium. Consequently, temperature gradients can cause significant shifts in the mode shapes and natural frequencies. In addition, steep temperature gradients associated with combustion cause the reflection of sound waves.

Some work has been done in the area of temperature dependent acoustics. Sujith et al. have found analytical solutions to the temperature dependent acoustic fields for select temperature distributions. Part of this chapter's objective is to summarize the physics and mathematics that have been developed to date. Applying these mathematical solutions to several case studies, a thorough exploration of temperature dependent wave propagation is accomplished. This includes explaining the amplitude variations observed in temperature dependent acoustic fields. Lastly, acoustic wave reflection due to steep temperature gradients is carefully studied.

6.2 Analytical Solution to Temperature Dependent Acoustic Wave Equation

Perhaps the best way to begin understanding the effects of temperature on acoustics is to first examine the differential equation describing temperature dependent acoustic waves. One can derive this differential equation using the assumptions of a perfect, inviscid, adiabatic gas in a one-dimensional acoustic field [23,24].

The starting point for the derivation is the linearized equations of momentum and energy respectively

$$\frac{\partial u'}{\partial t}+\frac{1}{\rho}\frac{\partial p'}{\partial x}=0\,, \tag{6.1}$$

$$\frac{\partial p'}{\partial t}+\gamma\overline{p}\frac{\partial u'}{\partial x}=0\,. \tag{6.2}$$

To obtain a wave equation, differentiate Eq. (6.1) with respect to x and Eq. (6.2) with respect to t and remove cross derivative terms,

$$\frac{\partial^2 p'}{\partial x^2}-\frac{1}{\overline{\rho}}\frac{\partial\overline{\rho}}{\partial x}\frac{\partial p'}{\partial x}-\frac{\overline{\rho}}{\gamma\overline{p}}\frac{\partial^2 p'}{\partial t^2}=0\,. \tag{6.3}$$

Differentiating the ideal gas equation of state yields the following relationship between temperature and density,

$$\frac{1}{\rho}\frac{d\overline{\rho}}{dx}+\frac{1}{T}\frac{dT}{dx}=0\,. \tag{6.4}$$

Combining Eq. (6.3) and Eq. (6.4) yields the partial differential equation for temperature dependent acoustic waves,

$$\frac{\partial^2 p'}{\partial x^2}-\frac{1}{T}\frac{dT}{dx}\frac{\partial p'}{\partial x}-\frac{1}{\gamma r T}\frac{\partial^2 p'}{\partial t^2}=0\,. \tag{6.5}$$

Assuming a steady-state solution ($p'(x,t)=P'(x)e^{i\omega t}$), the following relationship is acquired

$$\frac{d^2P'}{dx^2}-\frac{1}{T}\frac{dT}{dx}\frac{dP'}{dx}-\frac{\omega^2}{\gamma r T}P'=0\,. \tag{6.6}$$

However, to obtain analytical solutions, one must transfer Eq. (6.6) into mean temperature space

$$\left(\frac{d\overline{T}}{dx}\right)^2\frac{d^2P'}{d\overline{T}^2}-\frac{1}{\overline{T}}\frac{d}{dx}\left(\overline{T}\frac{d\overline{T}}{dx}\right)\frac{dP'}{d\overline{T}}-\frac{\omega^2}{\gamma r}\frac{P'}{\overline{T}}=0\,. \tag{6.7}$$

Presuming that the mean temperature is known, Eq. (6.7) can be solved to provide general analytical solutions.

6.3 Temperature Dependency – Analytical Solution

In order to solve Eq. (6.7), the mean temperature distribution must be given. Sujith et al. have developed analytical solutions for polynomial and exponential temperature profiles [23,24,25,26,27]. The procedure is explained below. First, the case of an arbitrary polynomial temperature distribution will be examined

$$\overline{T}(x)=(ax+b)^n\,, \tag{6.8}$$

here n can be any real number. Taking the appropriate derivatives, Eq. (6.8) can be substituted into Eq. (6.7) to obtain the following equation

$$\frac{d^2P'}{d\overline{T}^2}+\frac{2n-1}{n}\frac{1}{\overline{T}}\frac{dP'}{d\overline{T}}+\frac{\omega^2}{a^2n^2\gamma r}\frac{1}{\overline{T}^{3-2/n}}P'=0\,. \tag{6.9}$$

At this point, substitutions can be made to get Eq. (6.9) into a recognizable form

$$P'=w\overline{T}^{\alpha}, \qquad z=\beta\overline{T}^{\sigma}\,, \tag{6.10}$$

$$\alpha=\frac{1}{2}\left(\frac{1}{n}-1\right), \qquad \beta=\frac{\omega}{an\sigma\sqrt{\gamma r}}, \qquad \sigma=\frac{1}{n}-\frac{1}{2}\,. \tag{6.11}$$

Transforming Eq. (6.9) so that w and z are the dependent and independent variables respectively, one obtains the following familiar equation

$$z^2 \frac{d^2 w}{dz^2} + z\frac{dw}{dz} + \left(z^2 - v^2\right) w = 0, \qquad v = \frac{1-n}{2-n}. \tag{6.12}$$

Equation (6.12) is known as Bessel's differential equation. Consequently, the solution is described in terms of Bessel functions [6],

$$w = C_1 J_v\left(z\right) + C_2 Y_v\left(z\right). \tag{6.13}$$

J_v and Y_v are Bessel functions of the first and second kind respectively. Transforming Eq. (6.13) back to a function of pressure and temperature provides an analytical solution for the pressure distribution

$$P' = \overline{T}^{\alpha}\left(C_1 J_v\left(\beta \overline{T}^{\sigma}\right) + C_2 Y_v\left(\beta \overline{T}^{\sigma}\right)\right). \tag{6.14}$$

Under steady-state conditions, the one-dimensional acoustic momentum relation given in Eq. (6.1) can be used to obtain an expression for acoustic velocity

$$U' = -\frac{1}{i\omega\overline{\rho}}\frac{dP'}{dx} = -\frac{1}{i\omega\overline{\rho}}\frac{dP'}{d\overline{T}}\frac{d\overline{T}}{dx}. \tag{6.15}$$

Next, substitute Eq. (6.14) into Eq. (6.15) to obtain the following equation for acoustic velocity

$$U' = -\frac{1}{i\omega\overline{\rho}}\left[\frac{d\left(\overline{T}^{\alpha}\right)}{dx}\left(C_1 J_v\left(\beta\overline{T}^{\sigma}\right) + C_2 Y_v\left(\beta\overline{T}^{\sigma}\right)\right) + \overline{T}^{\alpha}\frac{d\left(C_1 J_v\left(\beta\overline{T}^{\sigma}\right) + C_2 Y_v\left(\beta\overline{T}^{\sigma}\right)\right)}{dx}\right] an\left(ax+b\right)^{n-1}. \tag{6.16}$$

To simplify Eq. (6.16) above, the definition for the derivative of a Bessel function must be utilized. Letting $\left(\Im\right)$ represent J, Y, $H^{(1)}$, $H^{(2)}$ or any linear combination of these functions [28], the derivative of $\left(\Im\right)$ is given as follows

$$\frac{d^k \Im_v(z)}{dz^k} = \frac{1}{2^k}\left\{\Im_{v-k}\left(z\right) - \binom{k}{1}\Im_{v-k+2}\left(z\right) + \binom{k}{2}\Im_{v-k+4}\left(z\right) - \ldots + \left(-\right)^k \binom{k}{k}\Im_{v-k+2k}\left(z\right)\right\} \quad k = 0,1,2,\ldots. \tag{6.17}$$

Using the derivative definition above, Eq. (6.16) can be reduced to the following form

$$U' = -\frac{an\overline{T}^{\alpha-1/n}}{i\omega\overline{\rho}}\left\{\begin{aligned}&\alpha\left[C_1J_v\left(\beta\overline{T}^{\sigma}\right)+C_2Y_v\left(\beta\overline{T}^{\sigma}\right)\right]\\&\quad+\frac{\beta\sigma\overline{T}^{\alpha}}{2}\left[C_1\left(J_{v-1}\left(\beta\overline{T}^{\sigma}\right)-J_{v+1}\left(\beta\overline{T}^{\sigma}\right)\right)+C_2\left(Y_{v-1}\left(\beta\overline{T}^{\sigma}\right)-Y_{v+1}\left(\beta\overline{T}^{\sigma}\right)\right)\right]\end{aligned}\right\}. \tag{6.18}$$

It should be noted that Eqs. (6.14) and (6.18) are valid for all values of n except for n equals two. For n equals two, the variable v given in Eq. (6.12) becomes infinite. For this value of n, an alternate solution in terms of hypergeometric functions must be used [25].

By following the same procedure outlined in Eqs. (6.8) through (6.18), an analytical solution can also be found for the acoustic pressure and velocity of an exponential temperature distribution

$$\overline{T} = be^{-\tau x}, \tag{6.19}$$

$$P' = \frac{1}{\sqrt{T}}\left(c_1J_1\left(\omega\delta/\sqrt{\overline{T}}\right)+c_2Y_1\left(\omega\delta/\sqrt{\overline{T}}\right)\right), \quad \delta = 2/\sqrt{\gamma Rc^2}, \tag{6.20}$$

$$U' = -\frac{b\tau e^{-\tau x}\overline{T}^{-3/2}}{2i\omega\rho}\left\{\begin{aligned}&\left[C_1J_1\left(\frac{\omega\delta}{\sqrt{\overline{T}}}\right)+C_2Y_1\left(\frac{\omega\delta}{\sqrt{\overline{T}}}\right)\right]\\&\quad+\frac{\omega\delta}{\sqrt{\overline{T}}}\left[C_1\left(J_0\left(\frac{\omega\delta}{\sqrt{\overline{T}}}\right)-J_2\left(\frac{\omega\delta}{\sqrt{\overline{T}}}\right)\right)+C_2\left(Y_0\left(\frac{\omega\delta}{\sqrt{\overline{T}}}\right)+Y_2\left(\frac{\omega\delta}{\sqrt{\overline{T}}}\right)\right)\right]\end{aligned}\right\}. \tag{6.21}$$

6.4 Standing Wave Patterns and Natural Frequencies

Since analytical solutions have been established, one can explore the temperature dependency of acoustic standing wave patterns and natural frequencies. This can be done by considering an example with simple geometry and boundary conditions. See Fig. 6.1 below.

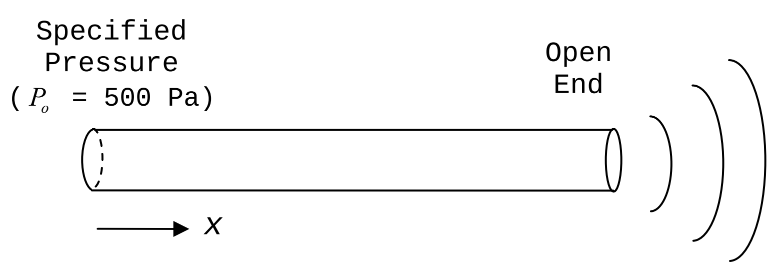

Fig. 6.1: Schematic of a case study performed with a straight duct open on one end and a pressure source on the other end. Different types of temperature distributions were examined

The simple case study outlined in the schematic above is used to examine the acoustic pressure and velocity fields for several different temperature profiles. To compare the acoustic fields, the standing wave patterns are plotted below for a frequency of 200 Hz. The selected frequency was arbitrarily chosen for this comparison.

Many times temperature profiles are approximated with an average temperature. This approximation can lead to significant errors. To demonstrate these errors, the pressure and velocity fields are compared for average and linear temperature distributions. This can be seen in Fig. 6.2 below. The acoustic fields for linear temperature profiles were calculated from Eqs. (6.14) and (6.18), and the acoustic fields for an average temperature are given in Eq. (6.22) below

$$P'(x) = P_o \frac{\sin\left(k\left(L-x\right)\right)}{\sin\left(kL\right)}, \qquad U'(x) = -\frac{iP_o}{\rho c}\frac{\cos\left(k\left(L-x\right)\right)}{\sin\left(kL\right)}. \tag{6.22}$$

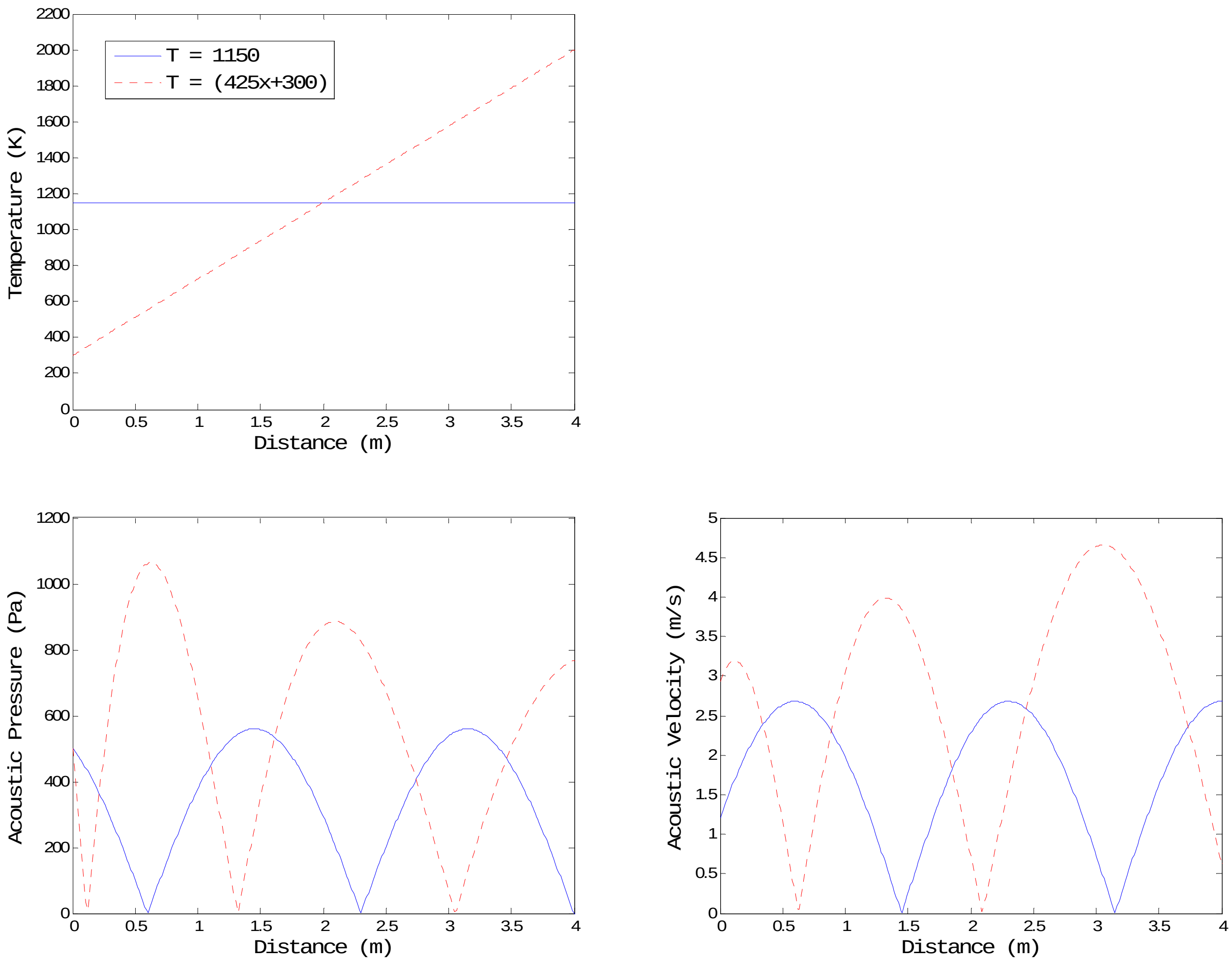

Fig. 6.2: **Standing wave patterns for a straight duct with different temperature profiles: (a) Pressure profile (b) Velocity profile**

The results in Fig. 6.2 show the dramatic differences in standing wave patterns. It is quite obvious from this result that assuming an average temperature leads to large errors when substantial temperature gradients are present.

To gain greater understanding of how temperature affects standing wave patterns, two more cases are shown with linear and polynomial temperature distributions. Fig. 6.3 below shows the pressure and velocity distributions for two different linear temperature profiles.

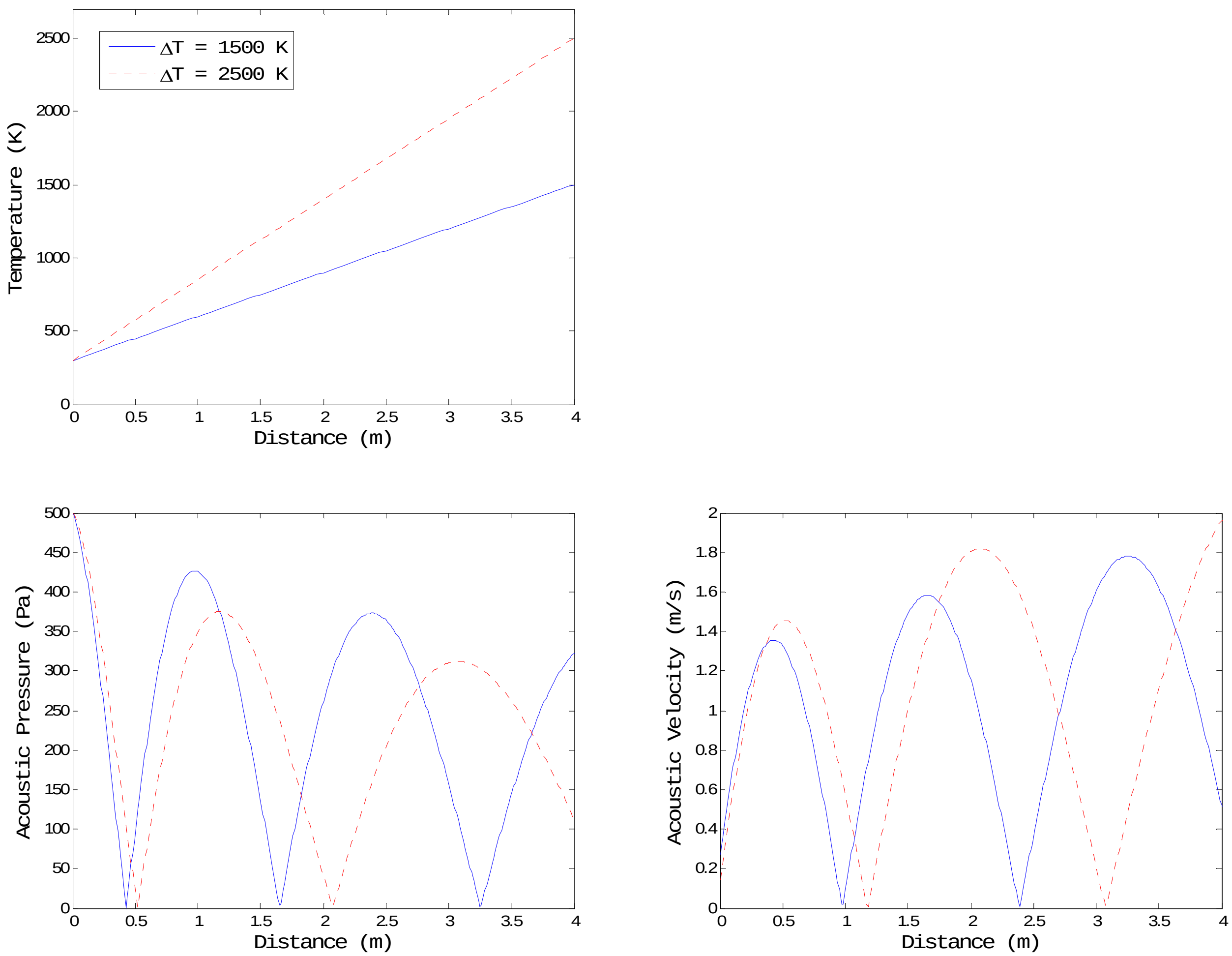

Fig. 6.3: **Standing wave patterns for a straight duct with linear temperature profiles: (a) Temperature distribution (b) Pressure profile (c) Velocity profile**

Fig. 6.3 shows how the variations in linear temperature profiles can produce significant differences in the standing wave patterns.

Wave patterns can also be examined for polynomial temperature profiles of the type shown in Eq. (6.8). Here the starting and ending temperatures will remain the same and two different values of power, n will be used.

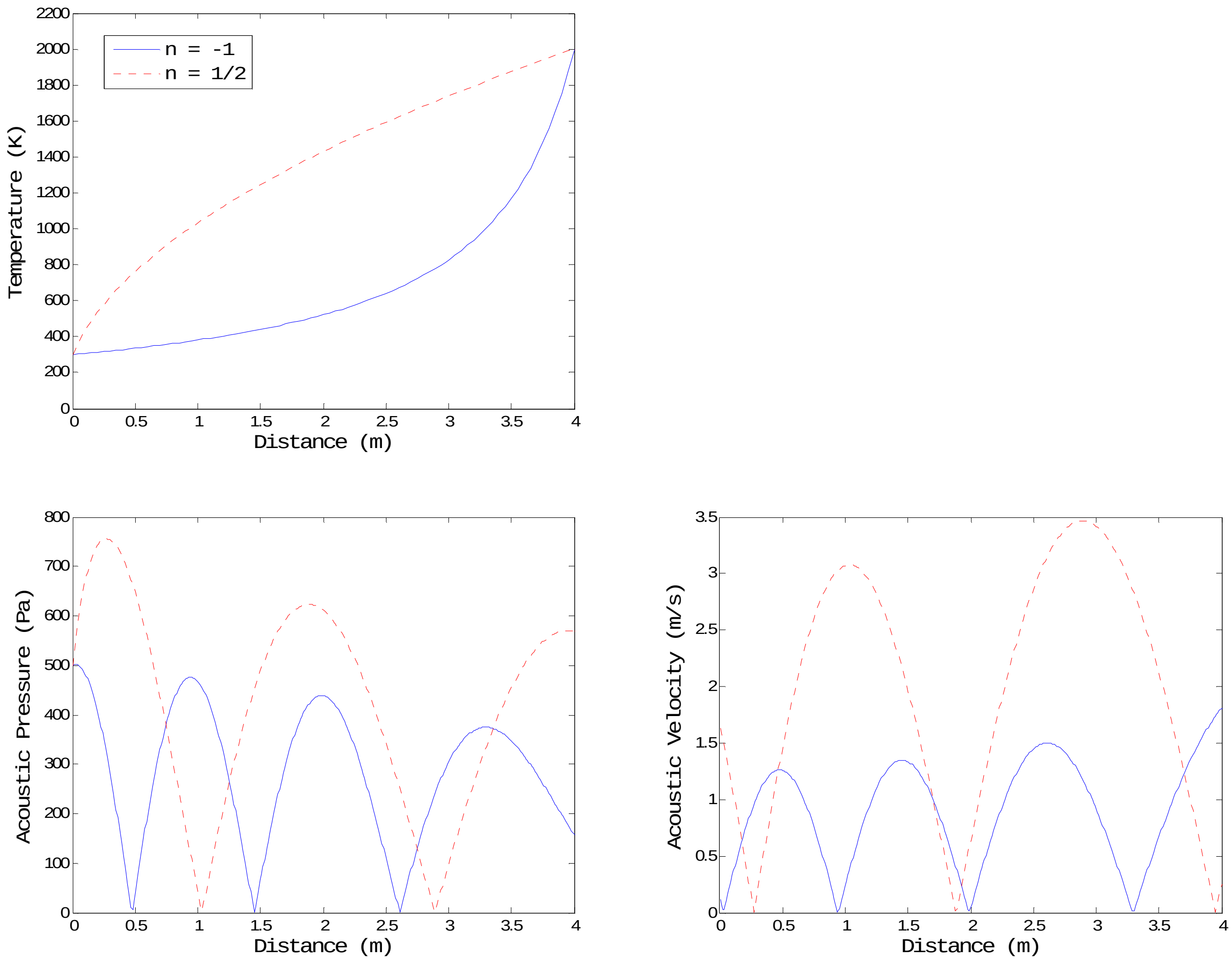

Fig. 6.4: **Standing wave patterns for a straight duct with polynomial temperature profiles: (a) Temperature distribution (b) Pressure profile (c) Velocity profile**

Even though the change in temperature is the same for both polynomials, it can again be seen that there is a significant change in the wave pattern. It is also interesting to note that the amplitudes of the standing pressure and velocity waves change with distance (x). This observation will be discussed in greater detail in section 5.

Temperature gradients not only effect the standing wave patterns, they also shift the natural frequencies (f_n). The natural frequencies are of interest because they lie extremely close to the resonance frequencies of the system due to the small amount of damping which is typically present in acoustic systems. The table below shows the first five natural frequencies of the duct for the temperature distributions shown in Fig. 6.2 through Fig. 6.4. The natural frequency comparison below is done for the case of the duct closed on the left end and open on the right end.

Table 6.1: Natural Frequency comparison

Case	Temperature Distribution	1st mode Hz	2nd mode Hz	3rd mode Hz	4th mode Hz	5th mode Hz
1	$\overline{T} = 1150$	42.5	127.6	212.6	297.7	382.7
2	$n = 1, \quad \Delta T = 1500$	40.8	107.7	177.0	246.8	316.9
3	$n = 1, \quad \Delta T = 2500$	51.2	130.7	213.5	297.1	381.1
4	$n = -1, \ \Delta T = 2000$	33.8	91.2	149.3	207.6	266.0
5	$n = 1/2, \ \Delta T = 2000$	50.1	135.4	221.6	308.2	395.0

Table 6.1 shows that the temperature distribution can have a large impact on the natural frequencies. As can be seen bin by comparing cases 2 and 3, the difference in the natural frequency due to temperature change increases as the difference in temperature increases. This result is expected. In addition, when comparing cases 4 and 5, both of the profiles have the same starting and ending temperatures, however, their slopes are different. Consequently, the differences in their natural frequencies are very significant, especially when considering higher modes. There is a difference of about 129 Hz between these two cases for the fifth natural frequency.

6.5 Reflection and Transmission Due to Temperature Change

When a plane wave encounters a change in the fluid medium, part of the incident wave is reflected backward and part is transmitted forward. This type of reflection occurs in combustion systems where sudden temperature gradients can appear local to a flame or an explosion. These temperature gradients create changes in the fluid properties which cause the acoustic waves to reflect. A standard way to quantify the reflected acoustic wave is the reflection coefficient. This quantity is defined below as the ratio of the amplitude of the reflected pressure wave over the amplitude of the incident pressure wave,

$$R = \frac{P_r}{P_i}. \tag{6.23}$$

The reflection coefficient can also be related to the acoustic impedance as shown below

$$(Z) = \overline{\rho}_1 c_1 \frac{1+R}{1-R} \tag{6.24}$$

In order to better understand how changes in the temperature gradients affect the reflection coefficient, three case studies were explored. The following three cases provide insight into how the reflection coefficient changes with frequency for different changes in temperature:

a) Reflection and transmission from one fluid to another: Assume a hot section and a cold section with a boundary at some location in the system separating the two mediums.

b) Reflection and transmission through a fluid layer: Here three separate sections are considered each with different mean temperatures. For this case, a cold and a hot section were used with a middle section at a transitional temperature.

c) Reflection and Transmission through a Temperature Gradient Region:
Using a similar approach as case two, one can again divide the system into three sections: cold, transitional, and hot. In this method, the temperature and fluid properties of the transitional section will smoothly evolve from cold to hot.

The first and second methods described above are commonly encountered in acoustic texts. However, the purpose in showing them in this thesis is to gain additional insights into how the variations of these first two cases affect the reflection coefficient. The third case is not commonly explored. A few studies have briefly mentioned reflected waves due to temperature gradients [24,25]. However, this section of the thesis will cover this topic in detail and draw novel conclusions that can be applied to more complex systems.

a) Reflection and Transmission from One Fluid to Another

This first case is the well known problem of an acoustic plane wave hitting a boundary separating two fluids with different impedances. Below is shown a simple schematic of the problem.

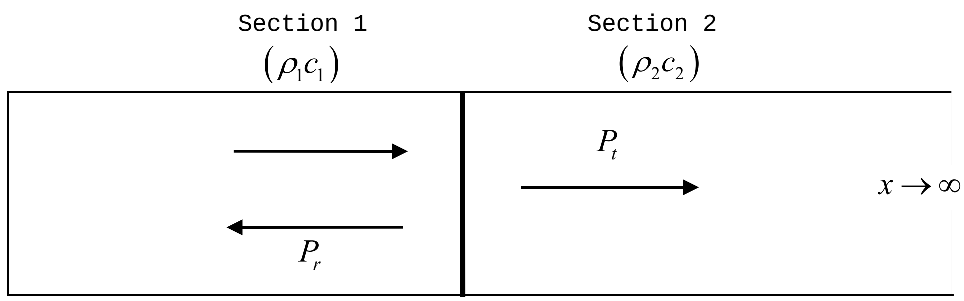

Fig. 6.5: **Schematic of the reflection and transmission of a plane wave incident on a boundary between two different fluids**

Using continuity of acoustic pressure and velocity at the interface between the two fluids, the relationship for the reflection coefficient due to two different fluids can be found

$$R = \frac{P_r}{P_i} = \frac{\rho_2 c_2 - \rho_1 c_1}{\rho_2 c_2 + \rho_1 c_1}. \tag{6.25}$$

The mathematical expression shown above indicates that the reflection coefficient, in this case, is constant over all frequencies with a value depending only on the characteristic impedance, $(\rho_i c_i)$ of the sections. Since the characteristic impedance is dependent on temperature, the reflection coefficient is plotted below for different jumps in temperature.

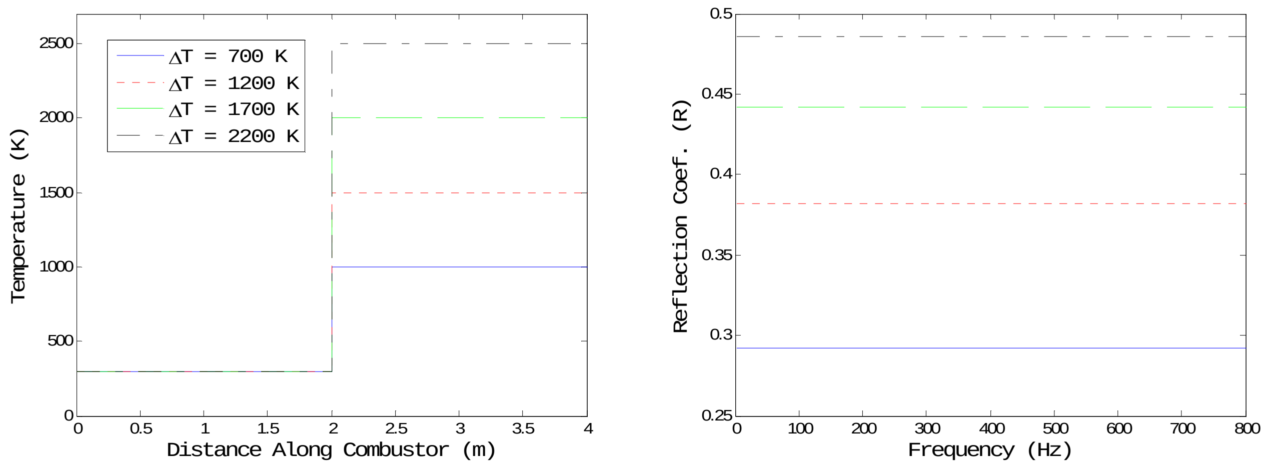

Fig. 6.6: **Reflection coefficients due to different jumps in temperature (a) Temperature distributions (b) Reflection coefficients**

Two important observations can be deduced from Fig. 6.6. First it can be seen that the reflection coefficient is constant over all frequencies. Secondly, as the temperature difference increases, the reflection coefficient also increases. However, it should be noted that the increase in the reflection coefficient is not linear. One can see from Fig. 6.7 below that the sensitivity of the reflection coefficient to changes in temperature is smaller as change in temperature becomes greater. The temperature changes shown in the figure below are higher than what is actually attainable in a real combustor, and is simply shown here to demonstrate the nonlinear behavior of the reflection coefficient. In addition, it should be noted the results shown in the figure below are frequency independent as long as the plane wave assumption is valid.

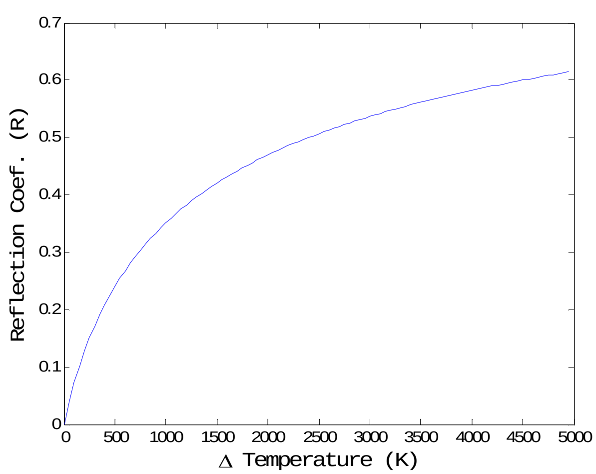

Fig. 6.7: **The relationship between the reflection coefficient and changes in temperature**

In the following two case studies, the reflection coefficient can be seen to have a similar behavior as that shown in Fig. 6.7.

b) Reflection and Transmission through a Fluid Layer

The second case study can also be found in acoustic texts. The description of the problem can be best described by the schematic shown below in Fig. 6.8.

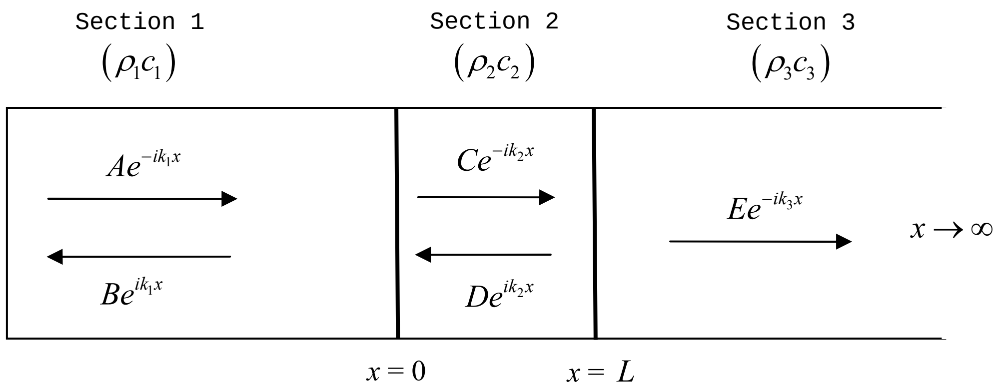

Fig. 6.8: Schematic of the reflection and transmission of a plane wave incident on a fluid layer

The analytical expression for the reflection coefficient for this second case is given below

$$R = \frac{(1-\rho_1 c_1/\rho_3 c_3)\cos(k_2 L) + i(\rho_2 c_2/\rho_3 c_3 - \rho_1 c_1/\rho_2 c_2)\sin(k_2 L)}{(1+\rho_1 c_1/\rho_3 c_3)\cos(k_2 L) + i(\rho_2 c_2/\rho_3 c_3 + \rho_1 c_1/\rho_2 c_2)\sin(k_2 L)}. \quad (6.26)$$

From Eq. (6.26), one can see that the reflection coefficient will have a frequency dependent wave form. The shape of this oscillatory reflection coefficient will be based on the length of section 2 and the ratios of characteristic acoustic impedance. As stated in the first case, the characteristic impedance is varied by changing the temperatures of the sections. In addition, the length of the second section is varied. Fig. 6.9 and Fig. 6.10 show the results.

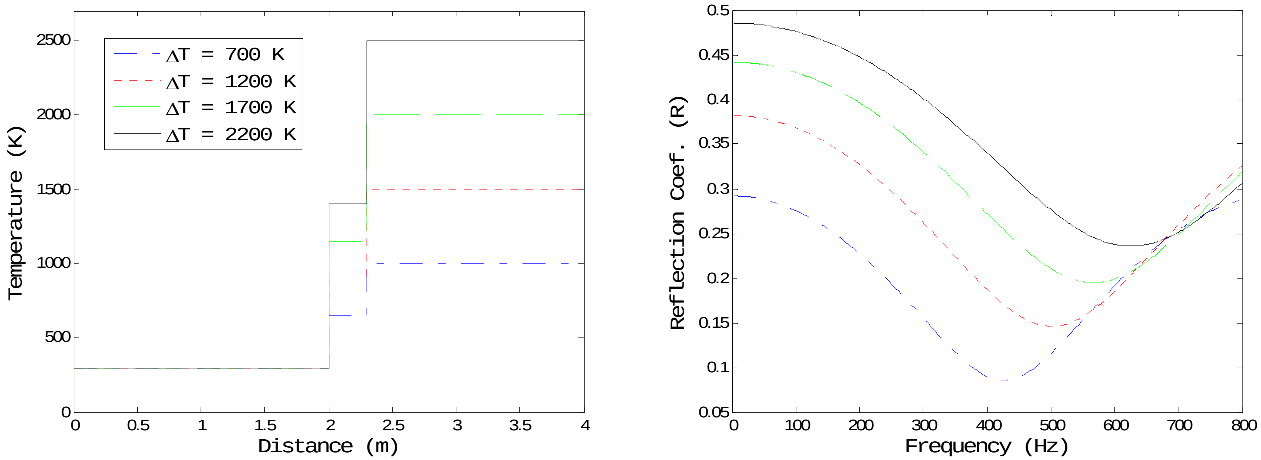

Fig. 6.9: **Change in reflection coefficient due to changes in the temperatures of the sections; with the length of the second section equal to 0.3 meters (a) Temperature distributions (b) Reflection coefficients**

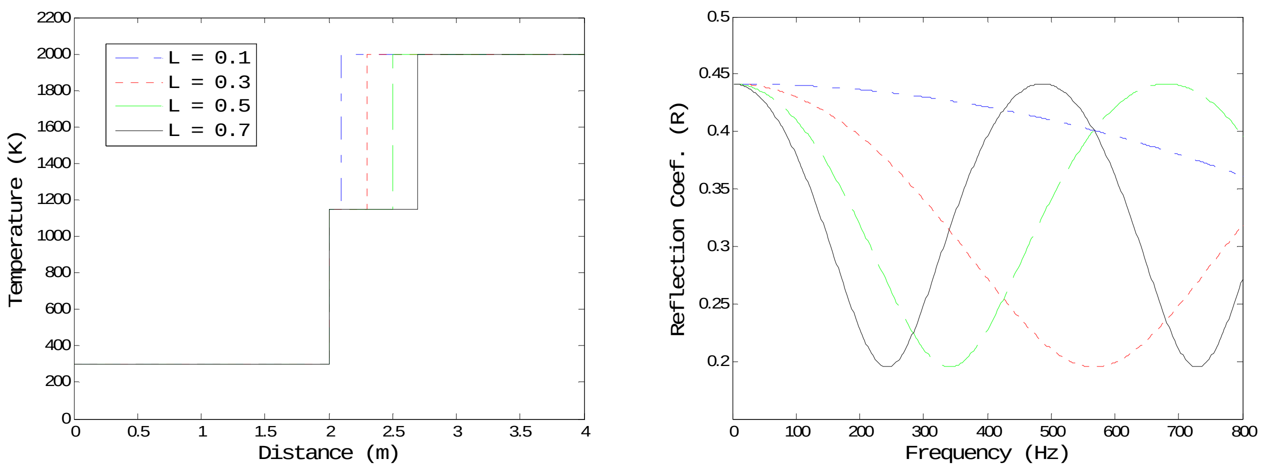

Fig. 6.10: **Change in reflection coefficient due to changes in the length of section 2 (a) Temperature distributions (b) Reflection coefficients**

Some general conclusions can be drawn from the figures above. As expected from the previous example, the reflection coefficient amplitude increases with the increased change in temperature in a similar manner as shown in Fig. 6.7. Secondly, as the length of section two is increased, as seen in Fig. 6.10, the wavelength of the reflection coefficient decreases. In addition, Fig. 6.9 shows that the reflection coefficient wavelength also decreases slightly as the temperature change becomes smaller.

c) Reflection and Transmission through a Temperature Gradient Region

The last case presented here provides the closest representation to the temperature profile of an actual combustion system with a flame. This case study, will again involve three sections. The difference as mentioned earlier, is that the temperature and fluid properties of the second section will transition smoothly from section 1 to section 2. To represent this smooth transition a linear temperature profile will be used initially. For the latter examples, an arbitrary polynomial temperature profile of the type shown in Eq. (6.8) will be assumed. The schematic below shows a representation of the problem.

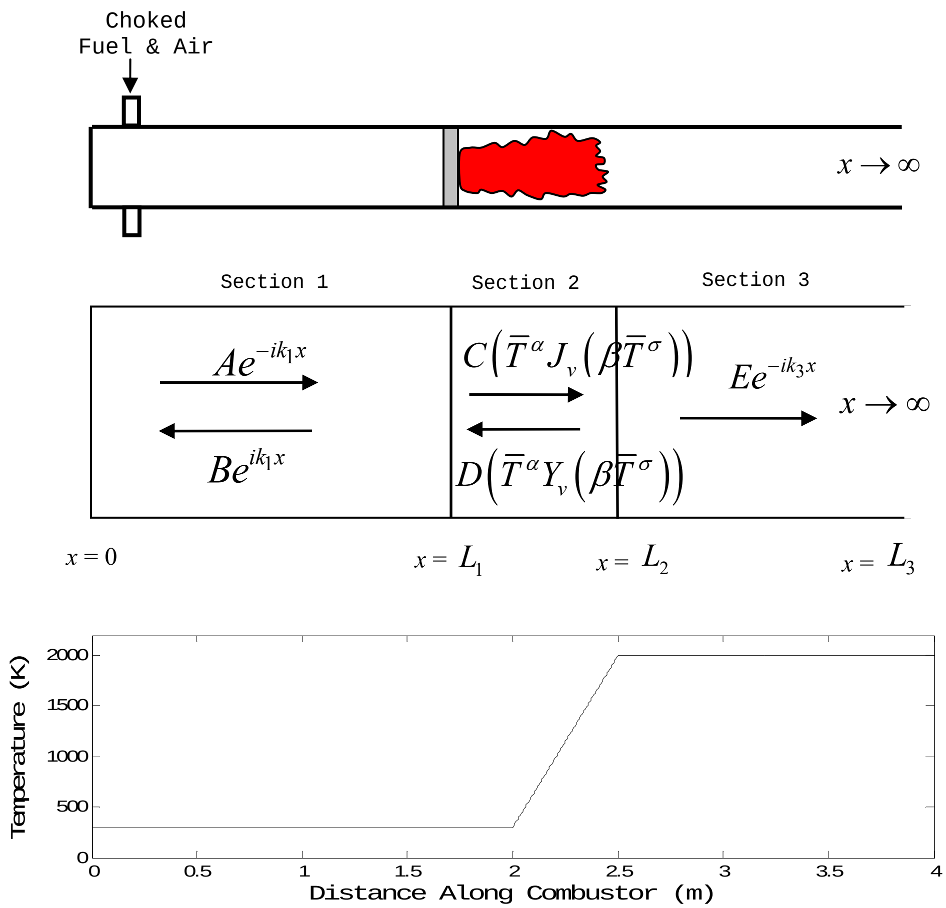

Fig. 6.11: **Schematic of the reflection and transmission of a plane wave incident on a temperature gradient region**

This case is substantially more complex than the first two cases and Eqs. (6.14) and (6.18) derived in section three must be used. The procedure to find the reflection coefficient is outlined below.

Continuity of acoustic pressure at $x = 0$

$$A + B = P_0 . \tag{6.27}$$

Continuity of acoustic pressure and velocity at $x = L_1$

$$Ae^{-ik_1L_1} + Be^{ik_1L_1} = C\left(\bar{T}_1^{\alpha}J_v\left(\beta\bar{T}_1^{\sigma}\right)\right) + D\left(\bar{T}_1^{\alpha}Y_v\left(\beta\bar{T}_1^{\sigma}\right)\right), \tag{6.28}$$

$$\frac{Ae^{-ik_1L_1}-Be^{ik_1L_1}}{\bar{\rho}c}=-\frac{an\bar{T}_1^{\alpha-1/n}}{i\omega\bar{\rho}}\left\{\begin{array}{l}\alpha\left[CJ_v\left(\beta\bar{T}_1^{\sigma}\right)+DY_v\left(\beta\bar{T}_1^{\sigma}\right)\right]\\+\dfrac{\beta\sigma\bar{T}_1^{\alpha}}{2}\left[\begin{array}{l}C\left(J_{v-1}\left(\beta\bar{T}_1^{\sigma}\right)-J_{v+1}\left(\beta\bar{T}_1^{\sigma}\right)\right)\\+D\left(Y_{v-1}\left(\beta\bar{T}_1^{\sigma}\right)-Y_{v+1}\left(\beta\bar{T}_1^{\sigma}\right)\right)\end{array}\right]\end{array}\right\}. \tag{6.29}$$

From continuity of acoustic pressure and velocity at $x = L_2$

$$C\left(\bar{T}_2^{\alpha}J_v\left(\beta\bar{T}_2^{\sigma}\right)\right)+D\left(\bar{T}_2^{\alpha}Y_v\left(\beta\bar{T}_2^{\sigma}\right)\right)=Ee^{-ik_3L_2}, \tag{6.30}$$

$$-\frac{an\bar{T}_2^{\alpha-1/n}}{i\omega\bar{\rho}}\left\{\begin{array}{l}\alpha\left[CJ_v\left(\beta\bar{T}_2^{\sigma}\right)+DY_v\left(\beta\bar{T}_2^{\sigma}\right)\right]\\+\dfrac{\beta\sigma\bar{T}_2^{\alpha}}{2}\left[\begin{array}{l}C\left(J_{v-1}\left(\beta\bar{T}_2^{\sigma}\right)-J_{v+1}\left(\beta\bar{T}_2^{\sigma}\right)\right)\\+D\left(Y_{v-1}\left(\beta\bar{T}_2^{\sigma}\right)-Y_{v+1}\left(\beta\bar{T}_2^{\sigma}\right)\right)\end{array}\right]\end{array}\right\}=\frac{Ee^{-ik_3L_2}}{\bar{\rho}c}. \tag{6.31}$$

With the above five equations, the 5 complex wave coefficients (*A, B*, *C*, *D*, and *E*) may be found. With these quantities the reflection coefficient upstream of the temperature gradient can be determined from the following equation

$$R=\frac{B}{A}e^{2ik_1x}. \tag{6.32}$$

The results of several different temperature profiles are shown in Fig. 6.12 through Fig. 6.17. In each case, the reflection coefficient is defined at (x = 1 m).

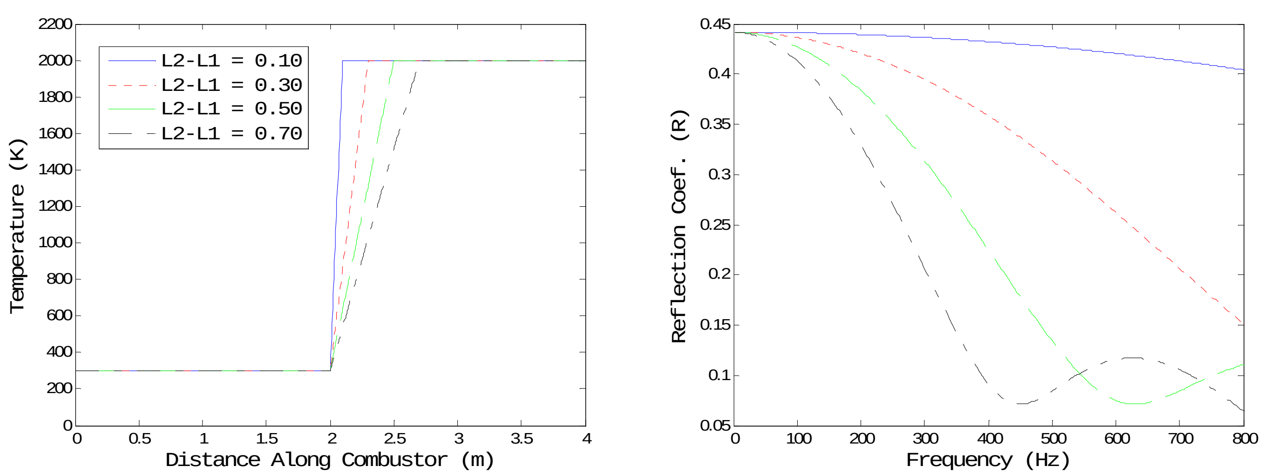

Fig. 6.12: **Comparison of the reflection coefficient as the value $\left(L_2-L_1\right)$ is changed. (a) Temperature distribution (b) Reflection Coefficient**

It was mentioned above, in case two, that as the length of the middle section $\left(L_2-L_1\right)$ increases, the wavelength of the reflection coefficient decreases. A similar phenomenon occurs with the smooth transition case. However, in this case, the magnitude of the reflection coefficient seems to resemble the response of a first order low-pass filter. Furthermore, as the length of the temperature gradient section increases, the bandwidth of the reflection coefficient is reduced. This can be observed easier if the frequency range is expanded and plotted in bode format; logarithmic frequency verses the reflection coefficient in decibels.

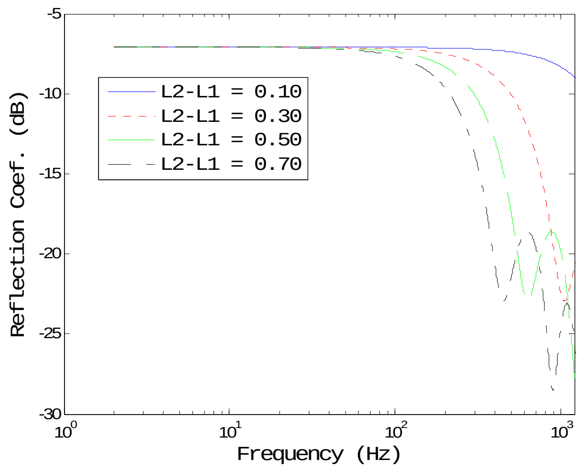

Fig. 6.13: **Comparison of the bandwidth of the reflection coefficient as the value $(L_2 - L_1)$ is changed**

As can be seen from the figure above, the bandwidth of the reflection coefficient continues to increase as the transitional section becomes smaller. Eventually, the limiting value of $(L_2 - L_1)$ equaling zero will be reached. As can be seen from the first case study in this section, the reflection coefficient would be independent of frequency until the plane wave assumption is no longer valid.

Another important area to investigate is the change in temperature.

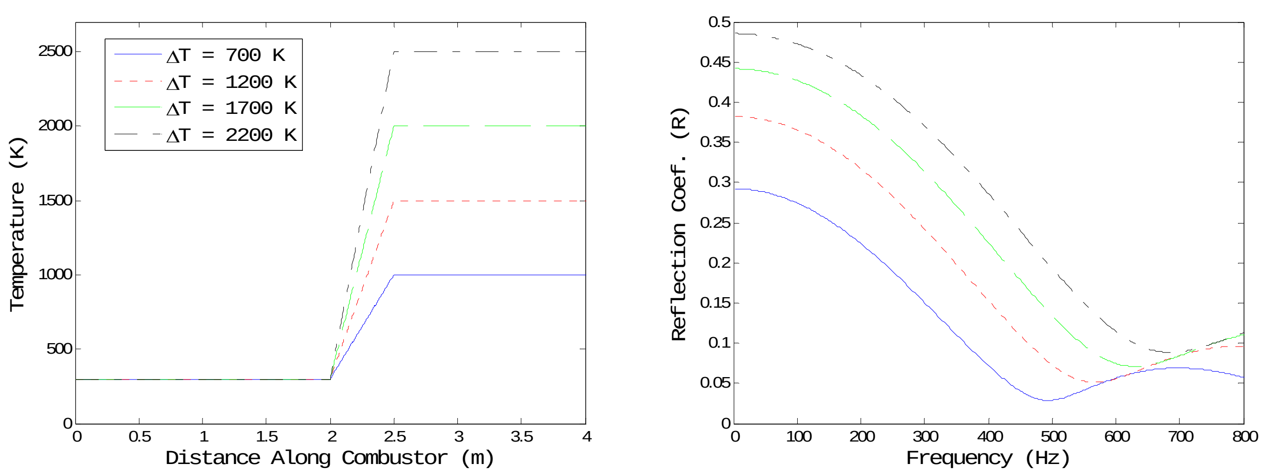

Fig. 6.14: **Comparison of the reflection coefficient as the change in temperature is increased. (a) Temperature distribution (b) Reflection coefficient**

Fig. 6.14 shows that as the change in temperature increases, the magnitude of the reflection coefficient also increases. Again, the manner in which the reflection coefficient increases is similar to the relationship shown in Fig. 6.7. It can therefore be concluded from these cases that the low frequency magnitude of the reflection coefficient (sometimes referred to as the DC gain) is only a function of the change in temperature. It should also be noted that the bandwidth slightly increases as the temperature increases which is similar to the results found in Fig. 6.9.

To further show that the bandwidth is predominantly a function of the length of section two and that the low frequency magnitude is a function of change in temperature, the slope of the temperature profile is fixed. Consequently, both the length and temperature are increased by the same proportion, eliminating slope as a variable.

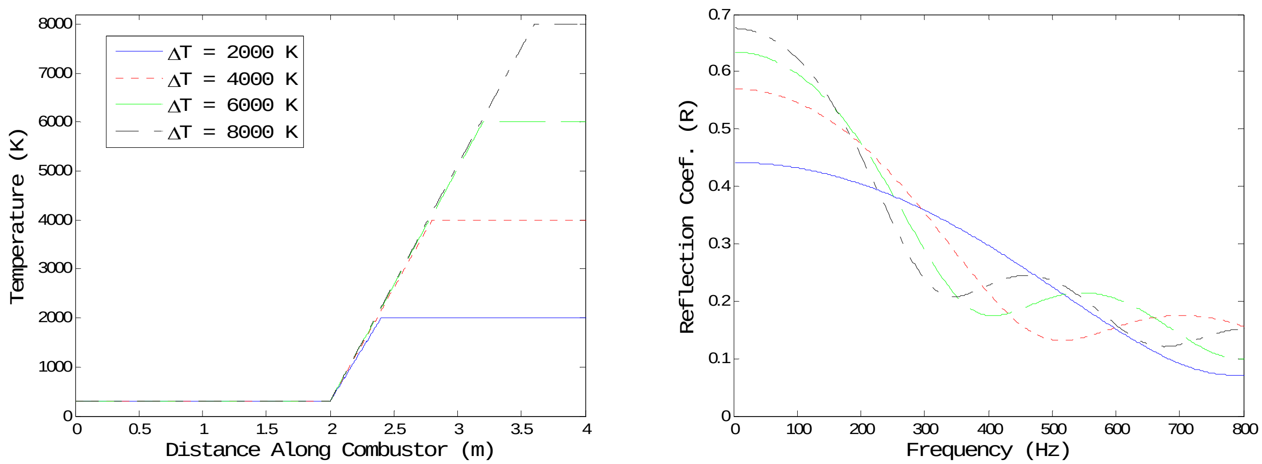

Fig. 6.15: Comparison of the reflection coefficient as the temperature profile slope is held constant. (a) Temperature distribution (b) Reflection coefficient

By examining Fig. 6.15, one can see again that the bandwidth increases as the length of section two decreases. Likewise, the conclusion that the low frequency magnitude or DC gain is a function of temperature is also supported.

One can now asses how the reflection coefficient responds to changes in the slope of the temperature profile while maintaining the same length and temperature change. This can be investigated by changing the power of a polynomial temperature distribution (n). The results are shown in the figures below.

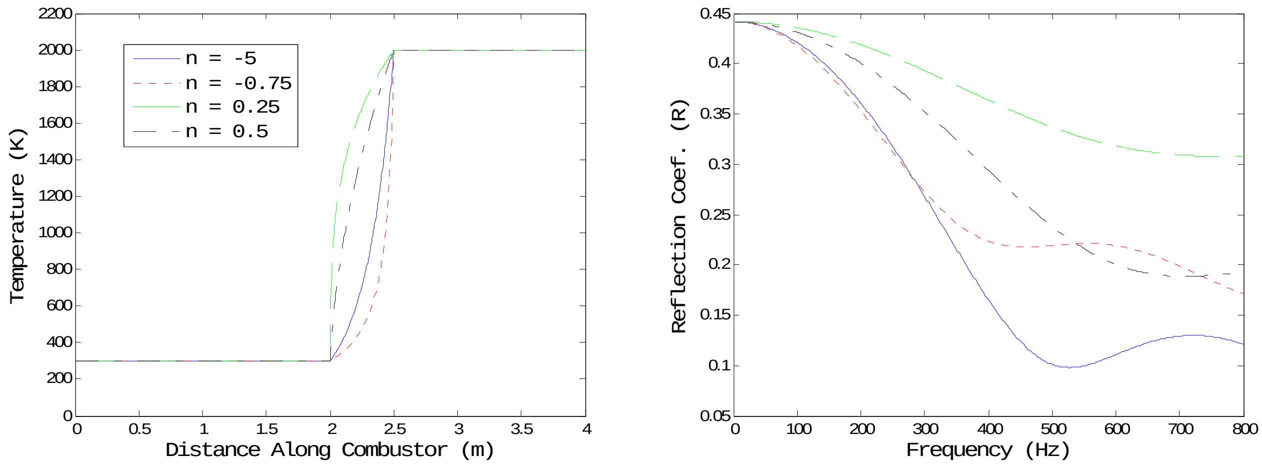

Fig. 6.16: **Comparison of the reflection coefficient as the power of the polynomial temperature distribution is changed.** $\left(L_2 - L_1\right) = 0.5\ m$. **(a) Temperature distribution (b) Reflection coefficient**

It appears that changing the slope of temperature distribution, effects the frequency dependent roll-off of the reflection coefficient. In order to better visualize this, Fig. 6.17 is shown in bode plot format although phase angle is not presented.

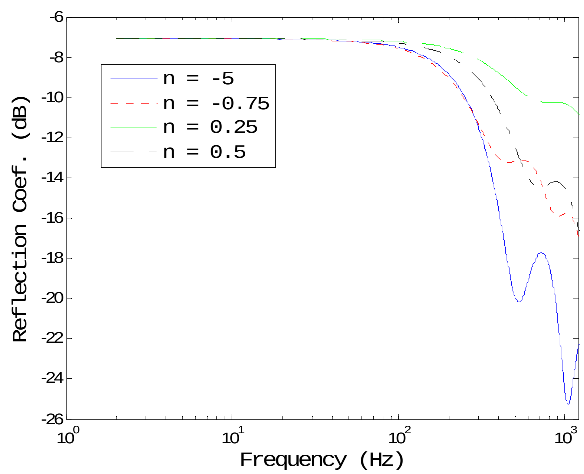

Fig. 6.17: **Comparison of the roll-off of the reflection coefficient for different values of *n***

Fig. 6.17 illustrates that the rate at which the reflection coefficient decreases is significantly affected by the slope of the temperature profile. It shows that when there is a steep initial slope the roll-off is the smallest. In addition, the steeper the average slope, the smaller the roll-off will be.

Table 6.2 below shows a summary of all the results that were shown in the three case studies.

Table 6.2: Summary of the case studies explored in this section

Case Study	Length	Slope	Δ Temp.	Bandwidth	DC Gain	Roll-off
1	NA	NA	↑	Infinite	↑	NA
2	↑	NA	Same	↓	Same	NA
2	Same	NA	↑	↑	↑	NA
3	↑	↓	Same	↓	Same	NA
3	Same	↑	↑	↑	↑	NA
3	↑	Same	↑	↓	↑	NA
3	Same	↑	Same	Same	Same	↓

In wrapping up this section, it is also interesting to observe that the reflection coefficient is independent of whether the acoustic wave is going from a high temperature to a low temperature or vise versa. The figure below shows this result.

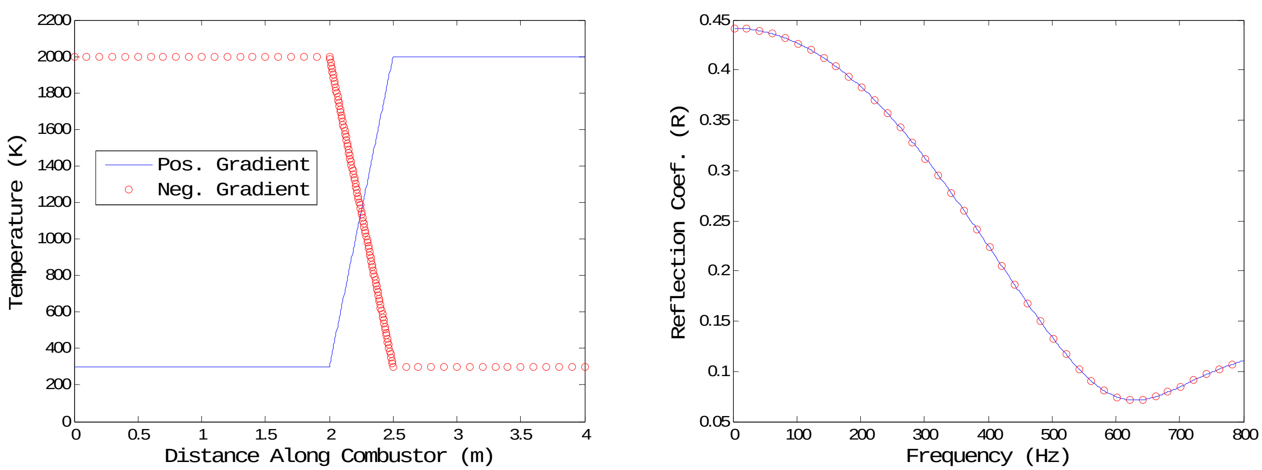

Fig. 6.18: **Comparison of the reflection coefficient with a positive and negative gradient. (a) Temperature distribution (b) Reflection coefficient**

The result from Fig. 6.18 shows that the reflection coefficient is the same independent of the direction the acoustic wave is traveling. This result is significant in the context of a combustor with hot and cold sections as shown in Fig. 6.19 below. In this example, the reflection due to the flame affects the right and left traveling waves identically. This result is based on the assumption of an ideal, inviscid, isentropic fluid. The biggest assumption here is an inviscid fluid. We know this is not really true, and furthermore, the damping in the system might be temperature dependent which could change the results presented in Fig. 6.18 to some degree.

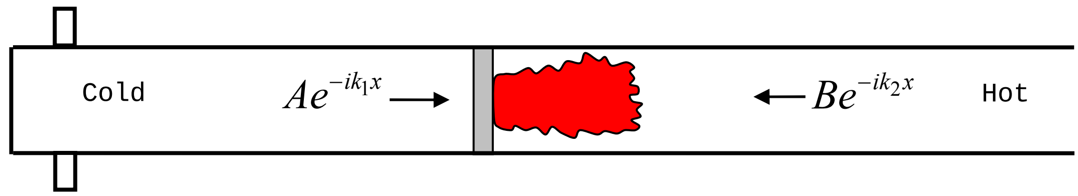

Fig. 6.19: **Schematic of the reflection and transmission of a plane wave incident on a temperature gradient region**

6.6 Finite Element Treatment of Large Temperature Gradients

In this section, finite element solutions are compared to the analytical solutions as a means of validating the finite element results. Some case studies with simple geometries were used to make this comparison. In doing so, such areas as standing wave patterns, impedance, and reflection coefficients were checked. In all cases, the analytical and finite element methods yield almost identical results. The convergence of the finite element solution was also examined as the mesh size was reduced.

In ABAQUS, the temperature profile can be accounted for in the finite element model by spatially mapping the temperature dependent bulk modulus and density to the combustor geometry. The equivalent result is the combustor being broken into many small discontinuities with incident, reflected, and transmitted waves at each discontinuity, see Fig. 6.20 below. As the mesh is refined to represent the temperature profile well, this finite element method approximates the analytical solutions in the previous sections very well.

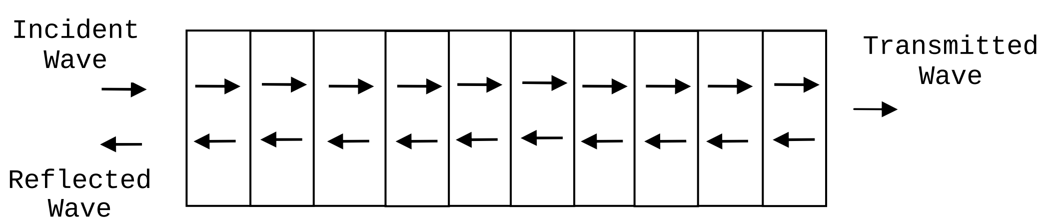

Fig. 6.20: Finite element representation where there are incident and reflected waves at each node due to change in the temperature dependent properties

6.6.1 Temperature Dependent Acoustic Properties

Density is one acoustic property that is altered by the temperature profile. In the combustion process, the fluid mixture is predominantly air with air-to-fuel ratios typically ranging from about 20 to 40. During combustion, the medium is heated resulting in a low density gas. It has been experimentally determined that the ideal-gas equation of state closely approximates the $P-v-T$ behavior of the real gasses at low densities [20]. Therefore it can generally be assumed that the fluid medium in a combustion system follows the ideal-gas relation

$$P = \rho r T \,. \tag{6.33}$$

An equation for the mean density in terms of mean temperature and pressure can be found by rearranging Eq. (6.33)

$$\bar{\rho} = \frac{\bar{P}}{r\bar{T}}, \qquad r = \frac{R_u}{M}. \tag{6.34}$$

Secondly, the speed of sound of the medium is altered by the temperature. Since most acoustic process are nearly isentropic, adiabatic, and reversible, the acoustic behavior of an ideal gas is commonly expressed as follows

$$\frac{P}{\bar{P}} = \left(\frac{\rho}{\bar{\rho}}\right)^{\gamma}, \qquad \gamma = \frac{C_p}{C_v}. \tag{6.35}$$

The thermodynamic speed of sound is defined as

$$c^2 = \frac{K}{\bar{\rho}}. \tag{6.36}$$

The variable K is the bulk modulus of the fluid and under adiabatic conditions can be expressed as

$$\bar{K} = \bar{\rho}\left(\frac{\partial P}{\partial \rho}\right)_{\bar{\rho}}. \tag{6.37}$$

Substituting Eq. (6.37) into Eq. (6.36), one gets

$$c^2 = \left(\frac{\partial P}{\partial \rho}\right)_{\bar{\rho}}. \tag{6.38}$$

Solving for P in Eq. (6.35) and substituting it into Eq. (6.38) we obtain the following

$$\bar{c}^2 = \frac{\gamma \bar{P}}{\bar{\rho}}. \tag{6.39}$$

Lastly substituting in Eq. (6.34), the speed of sound can be expressed only a function of the temperature, the specific gas constant, and the ratio of specific heats

$$\bar{c} = \sqrt{\gamma r \bar{T}} \,. \tag{6.40}$$

It should be noted that the ratio of specific heats, γ, is almost constant over a wide range of temperatures. For simplicity, it will be considered constant in this analysis.

The last acoustic property that will need to be examined is the bulk modulus. The stress-strain relationship for fluids is given by the bulk modulus and is defined as follows

$$\bar{K} = -\frac{\Delta V/V}{\bar{P}}. \tag{6.41}$$

For an adiabatic process, it can be defined by combining Eqs. (6.37) and (6.38) or (6.36) and (6.39)

$$\bar{K} = \bar{\rho}\left(\bar{c}\right)^2 = \frac{\bar{P}}{\cancel{\gamma}\cancel{\bar{T}}}\gamma\cancel{\gamma}\cancel{\bar{T}} = \gamma\bar{P}. \tag{6.42}$$

If we assume that the mean pressure in the combustor is essentially constant, then our adiabatic bulk modulus is constant with respect to temperature. Therefore, we can account for temperature change though the density or the speed of sound. One does not need to specify both. In this research, the temperature profile was accounted for by spatially mapping the temperature dependent density to the combustor geometry. The three main assumptions that we have made in coming to this conclusion are the assumptions of a perfect, invisid, isentropic gas.

6.6.2 Finite Element Convergence

The following simple example was used to check the accuracy and convergence of the finite element code in the presence of temperature gradients. The case study in this section again consists of a straight duct that is 4 meters long. It has a closed end at (x = 0) and an open end at (x = L). In addition, the following boundary conditions were enforced for all of the temperature distributions shown below:

$$\begin{array}{ll} x = 0 & x = L \\ P_1 = 500\ Pa & P_2 = 0\ Pa \\ T_1 = 300\ K & T_2 = 2000\ K \end{array} \tag{6.43}$$

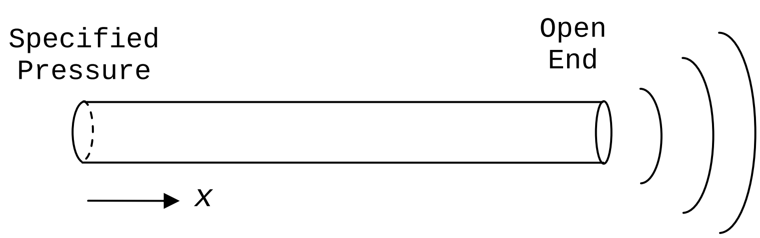

Fig. 6.21: Schematic of a case study performed with a straight duct open on one end and pressure source on the other Several different types of temperature distributions were examined.

Below we will investigate polynomial temperature distributions of the form

$$\bar{T} = \left(ax + b\right)^n. \tag{6.44}$$

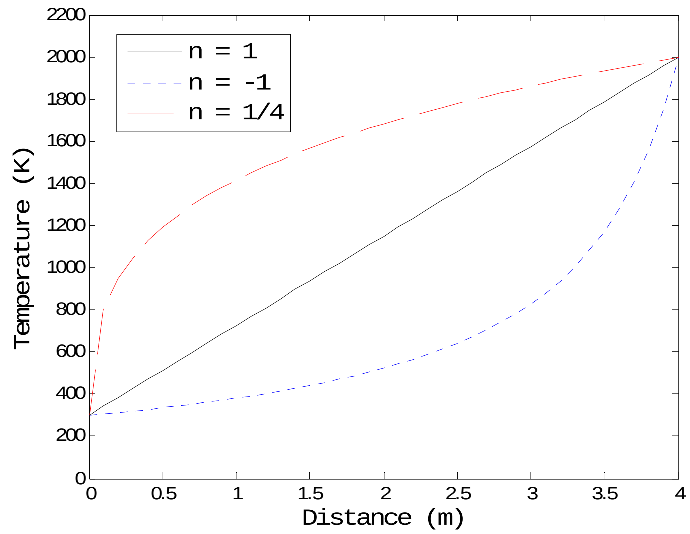

Fig. 6.22: Polynomial temperature distributions for different powers of *n*

The following plots below show the comparison between the finite element results and the analytical results for the temperature profiles shown in Fig. 6.22. For the following plots, quadratic elements were used with an element size of 0.1 meters.

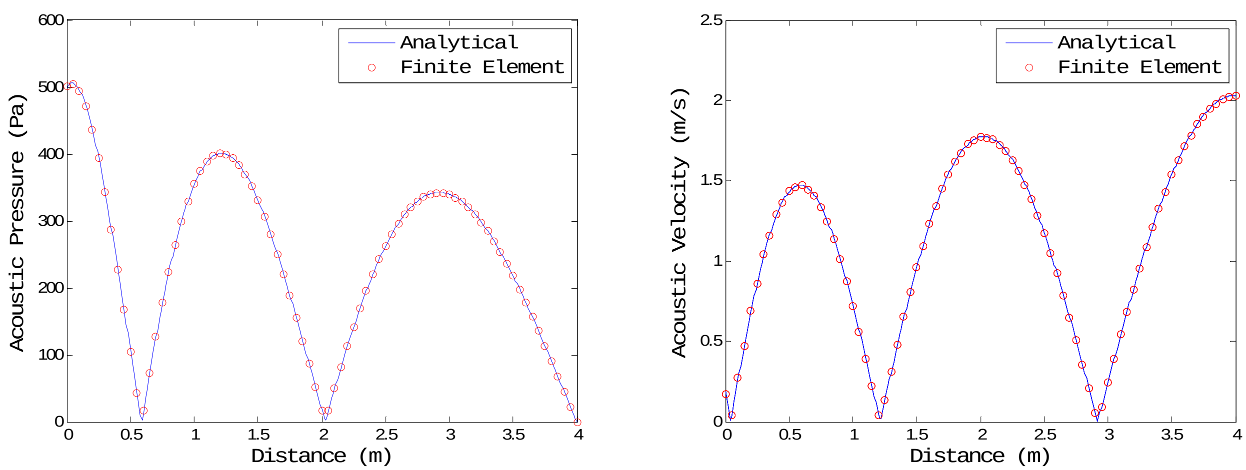

Fig. 6.23: Comparison between analytical and finite element solutions for a linear temperature profile (n = 1) at a frequency of 200 Hz and an element size of 0.1 meters: (a) Pressure distribution (b) Velocity Distribution

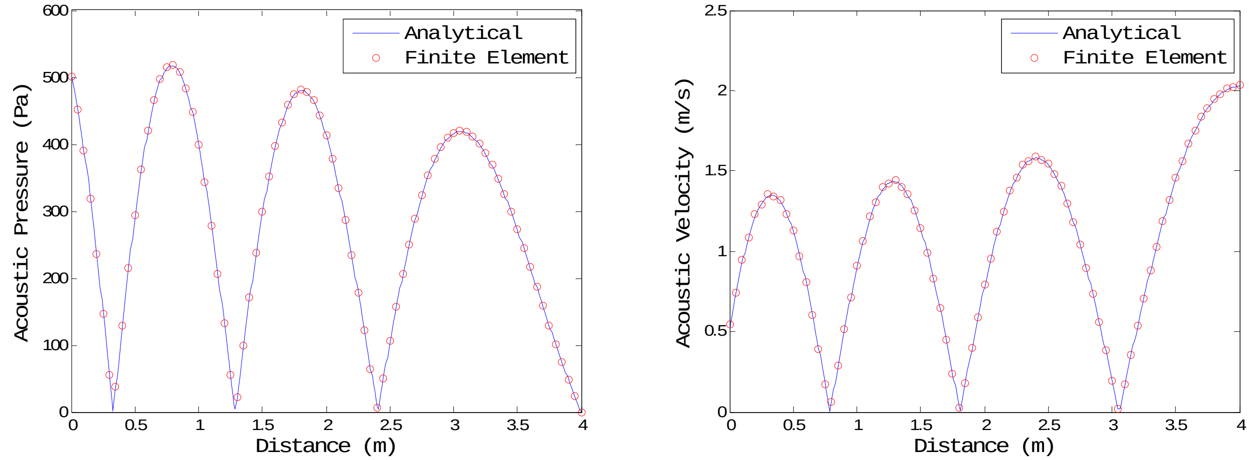

Fig. 6.24: Comparison between analytical and finite element solutions for a polynomial temperature profile (n = -1) at a frequency of 200 Hz and an element size of 0.1 meters: (a) Pressure distribution (b) Velocity Distribution

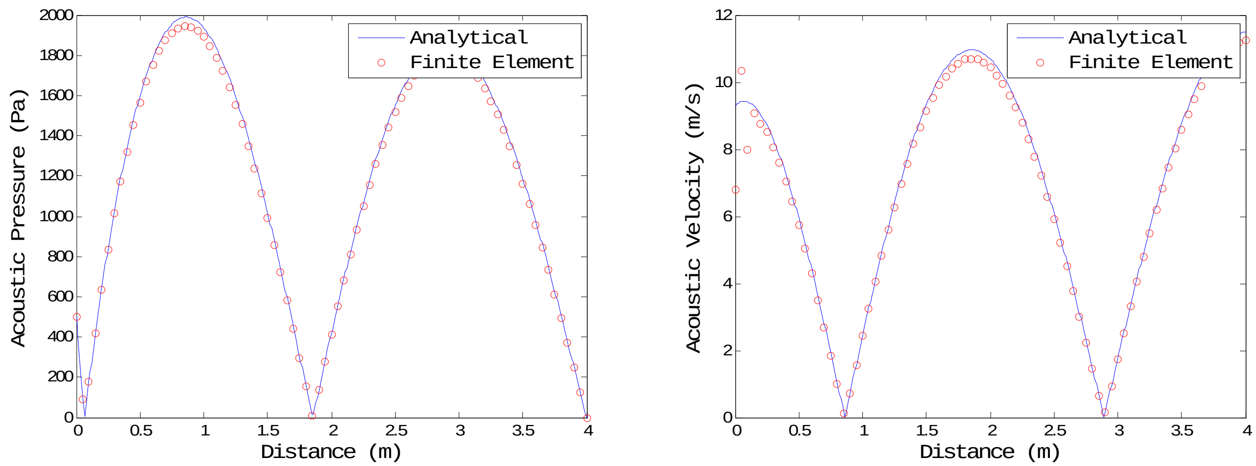

Fig. 6.25: Comparison between analytical and finite element solutions for a polynomial temperature profile (n = 0.25) at a frequency of 200 Hz and an element size of 0.1 meters: (a) Pressure distribution (b) Velocity Distribution

It can be seen that the finite element solution in Fig. 6.23 and Fig. 6.24 match the analytical solution exactly. However, careful examination of Fig. 6.25 shows some discrepancies between the analytical and FE solution. One also notices from the dramatic increase in amplitude in both the pressure and velocity that the temperature gradient of n = ¼ has caused the natural frequency to shift close to 200 Hz. Therefore, it is apparent that the system is near a resonant frequency.

A refinement of the mesh was attempted to see if better results could be achieved near the resonant frequencies. After refining the mesh, quadratic elements were used with an element size of 0.0001 meters. At this point the solution had converged and the results can be seen below.

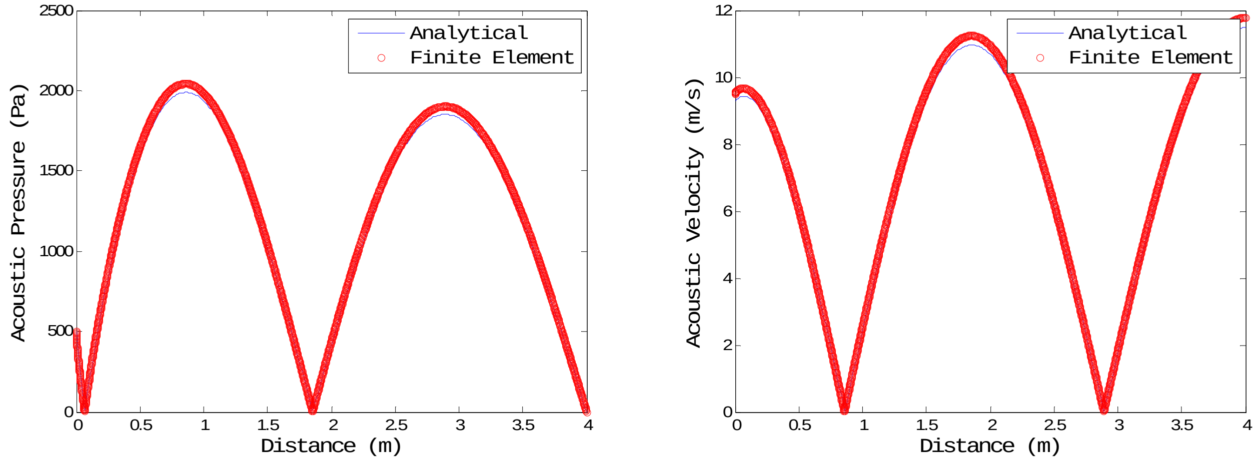

Fig. 6.26; Comparison between analytical and finite element solutions for a polynomial temperature profile (n = 0.25) at a frequency of 200 Hz and an element size of 0.0001 meters: (a) Pressure distribution (b) Velocity Distribution

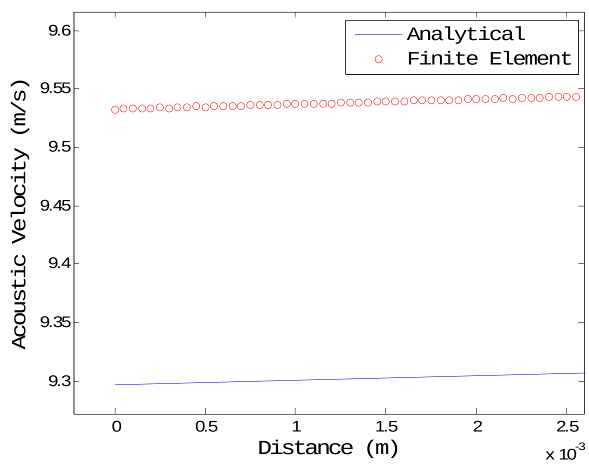

Fig. 6.27: Zoomed in look at Fig. 6.26 near $x = 0$

Although the solution has now converged, there is still some error involved which occurs mainly at the peaks in amplitude. This small error can be attributed to high sensitive in the FE model near resonance. Near resonant frequencies, very small change in model parameters, meshing, and numerical round-off can create finite error in the solution. Since the resonance phenomenon is a mathematical singularity, one would expect some inaccuracies near this frequency. This is important point to keep in mind, particularly when comparing and validating FE models.

6.6.3 Reflection Coefficient and Impedance

The acoustic impedance and reflection coefficient are two properties that are very important to capture appropriately in order to obtain an accurate acoustic response. The simple case study of a straight duct with a source at the left end and the right end being open is used to compare the finite element estimates of the reflection and impedance coefficients with the analytical values.. In addition, a steep temperature gradient is located in the middle of the duct. A comparison between the analytical and FE solution is shown below at the location of x equaling one meter.

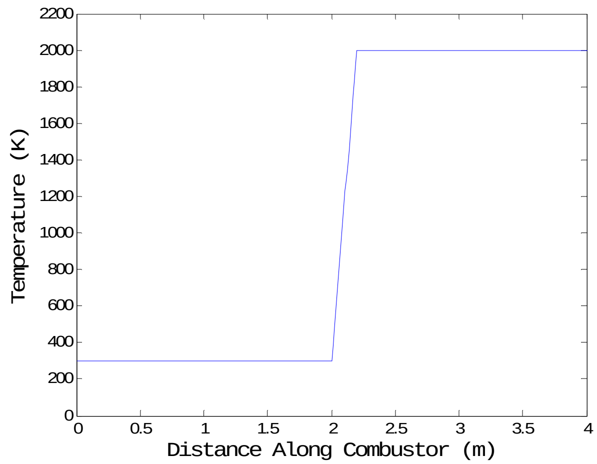

Fig. 6.28: Linear temperature profile with a steeper slope near the center of the duct. Temperature goes from 300 K to 2000 K in 0.2 meters.

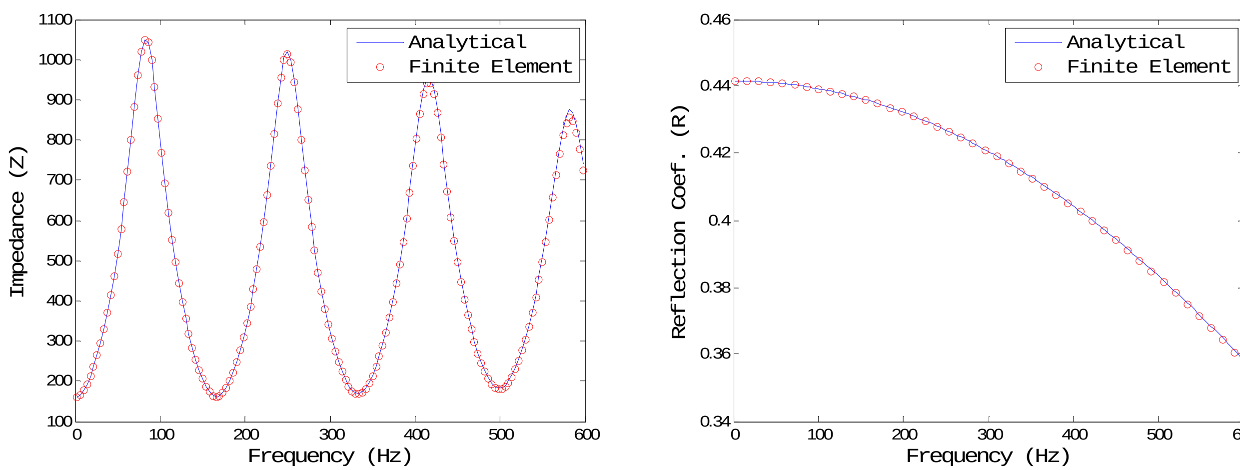

Fig. 6.29: Comparison between analytical and finite element solutions for a linear temperature profile shown in Fig. 6.28. Measurements taken at x = 1 meter and an element size of 0.05 meters: (a) Impedance (b) Reflection Coefficient

Comparing the finite element results for the temperature profile developed from n = -1/4.

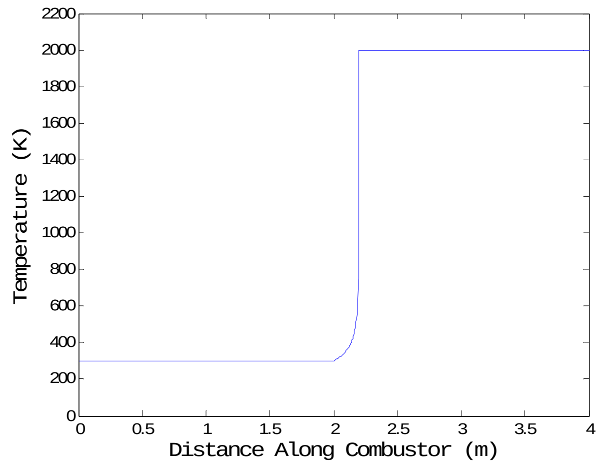

Fig. 6.30: Polynomial temperature profile with (n = -1/4) near the center of the duct. Temperature goes from 300 K to 2000 K in 0.2 meters.

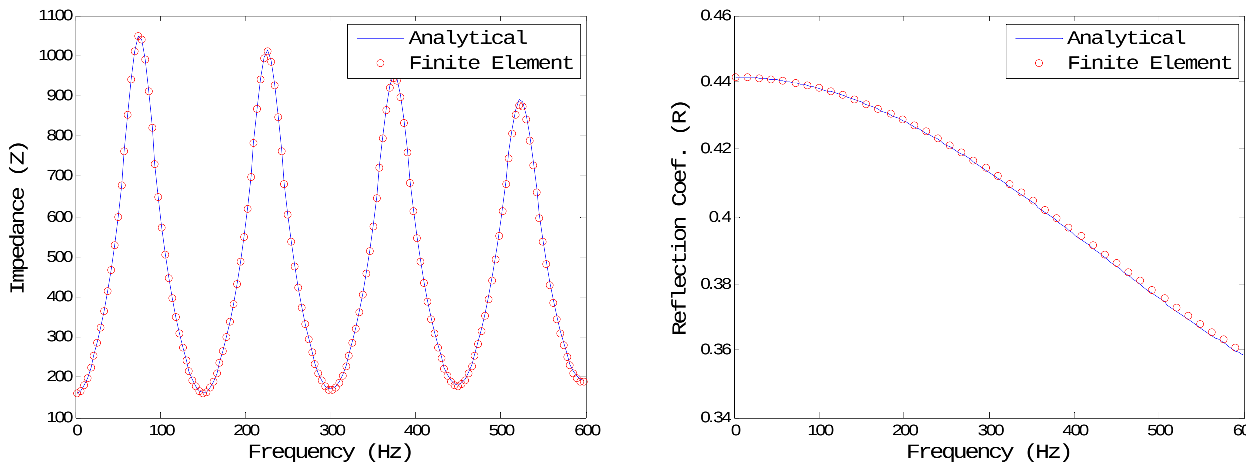

Fig. 6.31: Comparison between analytical and finite element solutions for a linear temperature profile shown in Fig. 6.30. Measurements taken at *x* = 1 meter and an element size of 0.05 meters local to the flame region: (a) Impedance (b) Reflection Coefficient

As can be seen from Fig. 6.29 and Fig. 6.31, the finite element solution lies right on top of the analytical solution. Therefore, ABAQUS automatically accounts for the reflection and impedance due to temperature change.

6.7 Determination of Temperature Profile

The temperature field can then be approximated either using numerical methods, experimental data, or some combination of these two. Since the sub-fluid volume has already been created for solving the cold acoustic finite element model, it would be reasonable to modify the element type, source, and boundary conditions and run a heat transfer simulation to get the temperature profile. However, for simplicity, in this study the temperature profile was simply measured using thermocouples distributed throughout the laboratory combustor and incorporating the numerically calculated adiabatic flame temperature. Once the temperature was measured with the thermocouples, a curve was fit through the measured temperatures. The temperature profile can be seen below in Fig. 6.32.

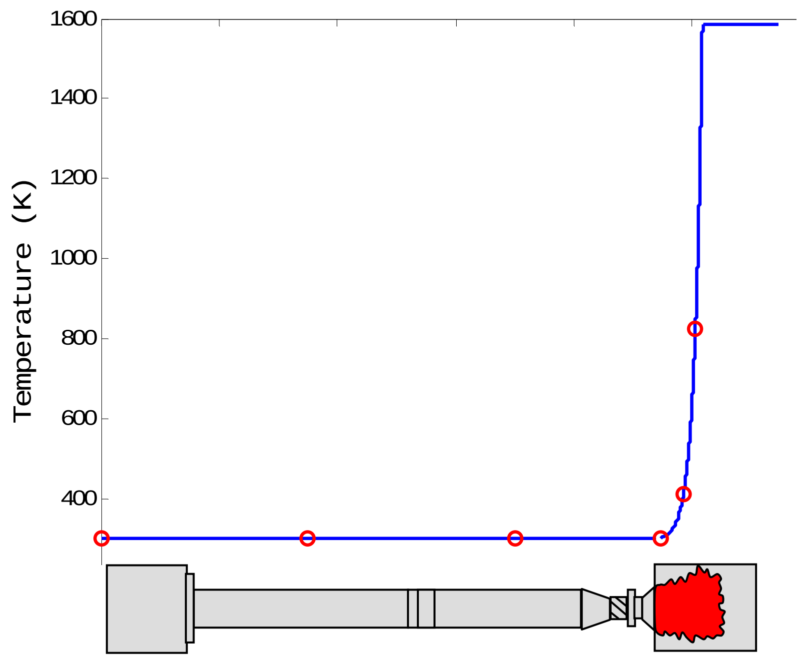

Fig. 6.32: Temperature profile for laboratory combustor

The flame is anchored at a spatial coordinate of about one meter. One can see the constant temperature profile at this location at about 1600 K. It is somewhat difficult to accurately measure the temperature of the flame. Therefore, it was assumed that the temperature is constant through the flame and the adiabatic flame temperature was used as an approximation. The adiabatic flame temperature and heat release rate was calculated using the common numerical Olikara and Borman routines [29]. Calculating these quantities at a flowrate of 25 SCFM and varying the equivalence ratio, the relationships shown below in Fig. 6.33 were found. The flowrate of 25 SCFM was a typical flow rate generally used while running experimental tests.

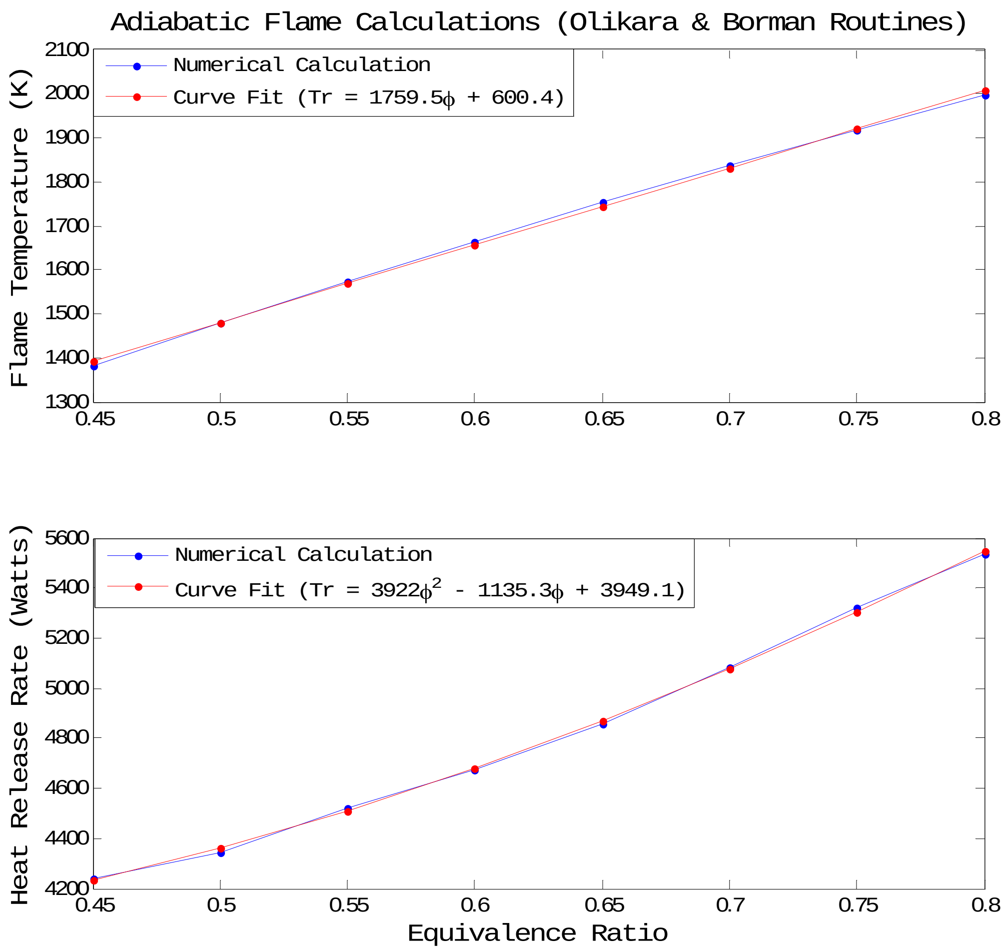

Fig. 6.33: Adiabatic flame temperature calculated using some standard numerical techniques

As seen in the Fig. 6.33 above, both the heat release rate and flame temperature can be found for any equivalence ratio. The approximate flame temperature was then used to complete the temperature distribution. As stated previously, once the temperature profile is known, it can be mapped to the acoustic FE model through the density and speed of sound

$$\overline{\rho} = \frac{\overline{P}}{r\overline{T}}, \qquad \overline{c} = \sqrt{\gamma r \overline{T}}\,. \tag{6.45}$$

6.8 Summary

From the sections above, it should be apparent that the temperature profile has a substantial impact on the acoustic characterization. It was also shown that the temperature profile could be accounted for in an FE model through the density and bulk modulus. Furthermore, it should also be apparent that the finite element method captures the effects of temperature extremely well. This includes not only the pressure and velocity distributions, but also the acoustic wave reflection and impedance. However, one does need to take precautions that the mesh has converged. This is particularly important for steep temperature gradients and around resonance frequencies. In the actual combustor, the temperature profile can be either calculated numerically or measured experimentally. Once the profile is determined, it can be mapped to the acoustic properties.

Chapter 7

7 Flame as an Acoustic Source

Characterizing the flame as an acoustic source which can then be implemented in a finite element package such as ABAQUS was an important task in this research. The approach taken here derives the full reacting wave equation from the basic conservation laws. We then simplify the reactive wave equation to we get it into an appropriate form to implement in the FE model.

7.1 Derivation of Full Reacting Flow Equations from First Principals

We begin by examining the conservation equations for our reacting flow system. Similar types of analysis have also been performed by Poinsot and Kuo [6, 30]. In this analysis, an effort has been made to go through the derivations as generally as possible and then make the appropriate simplifying assumptions at the end. Following this pattern, if some of the simplifying assumptions that are made at the end of this section are not appropriate for the readers system, he or she can easily determine that and adapt the equations to be as general as needed.

Before beginning the mathematical derivation, it should be noted that all of the analysis in this section uses Einstein's notation sometimes referred to as tensor index notation. This was done as a means of reducing the space that the equations take up. In this notation, the indices are written as subscripts using the Roman alphabet, namely *i*, *j*, and *k*. Typically the indices are 1, 2, and 3 representing the three dimensions of Euclidean space. For example, the term, x_i, represents the spatial position vector $[x_1, x_2, x_3]$ which is commonly expressed as $[x, y, z]$. Another important rule associated with this notation is that any index variable appearing twice in a single term implies that we are summing over all possible values. As an example, the term $\partial u_i / \partial x_i$ is the divergence of the velocity tensor, u_i. For more information on this type of notation, one can refer to most any basic continuum mechanic book. As a suggestion, chapter two of *Elements of Continuum Mechanics*, by Romesh Batra is a good reference [31].

7.1.1 Equation of Continuity

To start, we show the standard equation of continuity for the fuel-air mixture in the spatial description of motion and written in tensor form

$$\frac{\partial \rho}{\partial t} + \frac{\partial \left(\rho u_i\right)}{\partial x_i} = 0 . \qquad (7.1)$$

One can also write the conservation equation for each species in the mixture,

$$\frac{\partial\left(\rho Y_k\right)}{\partial t}+\frac{\partial}{\partial x_i}\left(\rho Y_k\left(u_i+V_{ki}\right)\right)=\dot{\omega}_k \qquad k=1,2,3,\ldots N \tag{7.2}$$

where Y_k is the mass fraction, V_{ki} is the diffusion velocity, and $\dot{\omega}_k$ is the reaction rate for each species, k. The diffusion velocity is a measure of the velocity of the kth species relative to the local velocity of the mixture.

7.1.2 Conservation of Momentum

Next we present the traditional conservation of momentum equation for a continuous medium

$$\frac{D\left(\rho u_i\right)}{Dt}=\frac{\partial\sigma_{ij}}{\partial x_j}+\rho b_i\,. \tag{7.3}$$

where σ_{ij} is the stress tensor and b_i represents the body forces. In general, the body force can be separated into a body force on each species

$$\frac{D\left(\rho u_i\right)}{Dt}=\frac{\partial\sigma_{ij}}{\partial x_j}+\rho\sum_{k=1}^{N}Y_k f_{ki} \tag{7.4}$$

In order to utilize Eq. (7.4), we need to determine a relationship between the stress tensor, pressure, and velocity. This can be done by making the basic assumption that we are dealing with a continuous, isotropic, and homogeneous medium. We will also assume that we have a Newtonian fluid. This simply means that we are assuming that the shear stress is linearly proportional to the rate of angular momentum. From these assumptions we obtain the following constitutive relationship

$$\sigma_{ij}=-p\delta_{ij}+\left(\mu'-\frac{2}{3}\mu\right)\frac{\partial u_k}{\partial x_k}\delta_{ij}+\mu\left(\frac{\partial u_i}{\partial x_j}+\frac{\partial u_j}{\partial x_i}\right). \tag{7.5}$$

As an observation, one should note that if we plug the constitutive relationship into the conservation of momentum equation and neglect all of the viscous terms, body forces, and convective terms in the material derivative we obtain the Euler's equation commonly used by acousticians

$$\frac{\partial u_i'}{\partial t}=-\frac{1}{\rho}\frac{\partial p'}{\partial x_i}\,. \tag{7.6}$$

7.1.3 Conservation of Energy

Out of the three conservation laws, the conservation of energy is significantly more complicated. Further more, the form that we will use in this analysis is not commonly seen, and it is not intuitive. For these reasons, a careful derivation of our form of the energy equation is laid out.

The first thing we do is imagine all of the different forms of energy transfer that can take place in a finite fluid volume. In doing this we come up with the relationship below

$$\begin{Bmatrix}\text{Rate of}\\ \text{accumulation}\\ \text{of internal and}\\ \text{kinetic energy}\end{Bmatrix}=\begin{Bmatrix}\text{Net rate of influx}\\ \text{of internal and}\\ \text{kinetic energy}\\ \text{by convection}\end{Bmatrix}+\begin{Bmatrix}\text{Net rate of}\\ \text{heat addition}\\ \text{due to}\\ \text{heat flux}\end{Bmatrix} \\ +\begin{Bmatrix}\text{Rate of}\\ \text{heat added by}\\ \text{heat source}\end{Bmatrix}+\begin{Bmatrix}\text{Net rate of work}\\ \text{done on system}\\ \text{by surroundings}\end{Bmatrix} \tag{7.7}$$

Writing this in mathematical terms, the conservation of energy can be expressed as

$$\left\{\frac{\partial}{\partial t}(\rho E)\right\}=\left\{-\frac{\partial}{\partial x_i}(\rho E u_i)\right\}-\left\{\frac{\partial q_i}{\partial x_i}\right\}+\left\{\dot{Q}\right\}+\left\{\frac{\partial\left(\sigma_{ij}u_i\right)}{\partial x_j}+\rho\sum_{k=1}^{N}Y_k f_{k,i}\left(u_i+V_{k,i}\right)\right\}. \tag{7.8}$$

We can combine the energy terms on the left hand side and expand them out using the chain rule of calculus,

$$\rho\frac{\partial E}{\partial t}+E\frac{\partial\rho}{\partial t}+E\frac{\partial\left(\rho u_i\right)}{\partial x_i}+\rho u_i\frac{\partial E}{\partial x_i}=-\frac{\partial q_i}{\partial x_i}+\dot{Q}+\frac{\partial\left(\sigma_{ij}u_i\right)}{\partial x_j}+\rho\sum_{k=1}^{N}Y_k f_{k,i}\left(u_i+V_{k,i}\right). \tag{7.9}$$

From continuity, we can eliminate part of the left hand side of this equation

$$E\left(\frac{\partial\rho}{\partial t}+\frac{\partial\left(\rho u_i\right)}{\partial x_i}\right)=0. \tag{7.10}$$

Thus we are left with the following

$$\rho\frac{\partial E}{\partial t}+\rho u_i\frac{\partial E}{\partial x_i}=-\frac{\partial q_i}{\partial x_i}+\dot{Q}+\frac{\partial\left(\sigma_{ij}u_i\right)}{\partial x_j}+\rho\sum_{k=1}^{N}Y_k f_{k,i}\left(u_i+V_{k,i}\right). \tag{7.11}$$

The variable E, in the above equation, represents the total stored energy per unit mass

$$E=e+\frac{u_i u_i}{2}, \tag{7.12}$$

where e is the specific internal energy, and the second term is the kinetic energy. We can substitute the above relationship into the left hand side of Eq. (7.11)

$$\rho\frac{\partial e}{\partial t}+\rho\frac{\partial}{\partial t}\left(\frac{u_i u_i}{2}\right)+\rho u_i\frac{\partial e}{\partial x_i}+\rho u_i\frac{\partial}{\partial x_i}\left(\frac{u_i u_i}{2}\right)=-\frac{\partial q_i}{\partial x_i}+\dot{Q}+\frac{\partial\left(\sigma_{ij}u_i\right)}{\partial x_j}+\rho\sum_{k=1}^{N}Y_k f_{k,i}\left(u_i+V_{k,i}\right). \tag{7.13}$$

We can now utilize the conservation of momentum equation to simplify the above expression. Multiplying Eq. (7.4) by the velocity vector, we obtain the mechanical-energy equation

$$\rho\frac{\partial}{\partial t}\left(\frac{u_i u_i}{2}\right)+\rho u_j\frac{\partial}{\partial x_j}\left(\frac{u_i u_i}{2}\right)-u_i\frac{\partial\sigma_{ij}}{\partial x_j}-\rho\sum_{k=1}^{N}Y_k f_{ki}u_i=0. \tag{7.14}$$

Utilizing Eq. (7.14), we can simplify Eq. (7.13) to the following form

$$\rho\frac{D(e)}{Dt}=-\frac{\partial q_i}{\partial x_i}+\dot{Q}+\sigma_{ij}\frac{\partial u_i}{\partial x_j}+\rho\sum_{k=1}^{N}Y_k f_{k,i}V_{k,i}. \tag{7.15}$$

To get the above energy balance into a more useful state we would like to express the energy in terms of enthalpy. We can do this by using the relationship between energy and enthalpy

$$e=h+\frac{p}{\rho}. \tag{7.16}$$

In order to make the above relationship useful, we must take its total derivative

$$\frac{D(\rho e)}{Dt}=\frac{D(\rho h)}{Dt}-\frac{Dp}{Dt}. \tag{7.17}$$

Using the chain rule of calculus and factoring like terms we obtain the following expression

$$\rho\frac{De}{Dt}=(h-e)\frac{D\rho}{Dt}+\rho\frac{Dh}{Dt}-\frac{Dp}{Dt}. \tag{7.18}$$

The continuity equation, Eq. (7.1) can also be expressed as

$$\frac{D\rho}{Dt}=-\rho\frac{\partial u_i}{\partial x_i}. \tag{7.19}$$

We can then substitute the above expression along with the relationship that $(e-h)=p/\rho$ into Eq. (7.18)

$$\rho\frac{De}{Dt}=\rho\frac{Dh}{Dt}-\frac{Dp}{Dt}-p\frac{\partial u_i}{\partial x_i}. \tag{7.20}$$

Equation (7.20) can now be substituted into Eq. (7.15) to obtain the following equation

$$\rho\frac{Dh}{Dt}=\frac{Dp}{Dt}+p\frac{\partial u_i}{\partial x_i}-\frac{\partial q_i}{\partial x_i}+\dot{Q}+\sigma_{ij}\frac{\partial u_i}{\partial x_j}+\rho\sum_{k=1}^{N}Y_k f_{k,i}V_{k,i}. \tag{7.21}$$

We can simplify this expression even further by separating enthalpy into its sensible and chemical parts

$$h = h_s + \sum_{k=1}^{N} \Delta h_{f,k} Y_k \,. \tag{7.22}$$

where h_f is the enthalpy of formation and h_s is the sensible enthalpy which is equal to $\int_{T_o}^{T} C_p dT$. The total derivative of Eq. (7.22) is then expressed as

$$\rho \frac{Dh}{Dt} = \rho C_p \frac{DT}{Dt} + \sum_{k=1}^{N} h_{sk} \dot{\omega}_k + \sum_{k=1}^{N} \Delta h_{fk} \dot{\omega}_k \,. \tag{7.23}$$

where $\dot{\omega}_k$ is the reaction rate for each species and is defined as $\rho DY_k / Dt$. The last two terms in the expression above can be grouped together and defined as the heat release rate

$$\sum_{k=1}^{N} h_k \dot{\omega}_k = \sum_{k=1}^{N} h_{sk} \dot{\omega}_k + \sum_{k=1}^{N} h_{f,k} \dot{\omega}_k \,. \tag{7.24}$$

We can now substitute Eq. (7.23) into Eq. (7.21) and acquire the following relationship

$$\rho C_p \frac{DT}{Dt} = -\sum_{k=1}^{N} h_k \dot{\omega}_k + \frac{Dp}{Dt} + p \frac{\partial u_i}{\partial x_i} - \frac{\partial q_i}{\partial x_i} + \dot{Q} + \sigma_{ij} \frac{\partial u_i}{\partial x_j} + \rho \sum_{k=1}^{N} Y_k f_{k,i} V_{k,i} \,. \tag{7.25}$$

From here, there are a couple more steps to get the energy equation into its most suitable form. The first step is to introduce the viscous tensor,

$$\tau_{ij} = \sigma_{ij} + p\delta_{ij} \tag{7.26}$$

The second step is to expand out the heat flux term,

$$q_i = -\lambda \frac{\partial T}{\partial x_i} + \sum_{k=1}^{N} h_k Y_k V_{ki} + R_u T \sum_{k=1}^{N} \sum_{l=1}^{N} \left(\frac{X_l \alpha_k}{W_k D_{kl}} \right) \left(V_{ki} - V_{li} \right) \tag{7.27}$$

where the last term is called the Dufour effect which show concentration gradients in terms of diffusion velocities. However, in most all cases the Dufour effect is so small that it is negligible and is included in Eq. (7.27) only for the sake of completeness.

If we plug in the above two expressions into Eq. (7.25) and simplify, we obtain the following result,

$$\rho C_p \frac{DT}{Dt} = -\sum_{k=1}^{N} h_k \dot{\omega}_k + \frac{Dp}{Dt} + \frac{\partial}{\partial x_i} \left(\lambda \frac{\partial T}{\partial x_i} \right) - \left(\rho \sum_{k=1}^{N} C_{pk} Y_k V_{ki} \right) \frac{\partial T}{\partial x_i} + \dot{Q} + \tau_{ij} \frac{\partial u_i}{\partial x_j} + \rho \sum_{k=1}^{N} Y_k f_{k,i} V_{k,i} \tag{7.28}$$

The conservation of energy equation is now in a form that will be most suitable for us to use. For completeness, we give a brief description of each of the terms in the equation:

$\rho C_p \dfrac{DT}{Dt}$ = Part of the total derivative of sensible enthalpy

$-\sum_{k=1}^{N} h_k \dot{\omega}_k$ = Heat release rate due to species k

$\frac{Dp}{Dt}$ = Material derivative of the total pressure

$\frac{\partial}{\partial x_i}\left(\lambda \frac{\partial T}{\partial x_i}\right)$ = Heat diffusion term expressed using Fourier's law of heat conduction

$\left(\rho \sum_{k=1}^{N} C_{pk} Y_k V_{ki}\right)\frac{\partial T}{\partial x_i}$ = Heat diffusion term associated with species having different enthalpies

$\dot{Q}$ = Heat source term (ex: electric spark, laser, radiative term)

$\tau_{ij}\frac{\partial u_i}{\partial x_j}$ = Viscous tensor multiplied by the velocity gradient (viscous heating source term)

$\rho \sum_{k=1}^{N} Y_k f_{k,i} V_{k,i}$ = Power Produced by volume forces on each species k

7.2 Wave Equation for Reacting Flows

At this point, we are ready to develop the reacting flow wave equation from the conservation laws we have developed above [6]. There are several ways to approach this task. In the discussion below, we outline one method to arrive at the reacting flow wave equation. It is done by first dividing Eq. (7.28) by $\rho C_p T$

$$\frac{1}{T}\frac{DT}{Dt} = \frac{1}{\rho C_p T}\left(-\sum_{k=1}^{N} h_k \dot{\omega}_k + \frac{Dp}{Dt} + \frac{\partial}{\partial x_i}\left(\lambda \frac{\partial T}{\partial x_i}\right) - \left(\rho \sum_{k=1}^{N} C_{pk} Y_k V_{ki}\right)\frac{\partial T}{\partial x_i} + \dot{Q} + \tau_{ij}\frac{\partial u_i}{\partial x_j} + \rho \sum_{k=1}^{N} Y_k f_{k,i} V_{k,i}\right). \tag{7.29}$$

Now we can take a look at the left hand side of the above equation and manipulate it by using the ideal gas equation of state, $p = \rho r T$ and the chain rule of calculus

$$\frac{1}{T}\frac{DT}{Dt} = \frac{\rho r}{p}\frac{D}{Dt}\left(\frac{p}{\rho r}\right) = \left(\frac{1}{p}\frac{Dp}{Dt} + r\frac{D\left(\frac{1}{r}\right)}{Dt} + \rho\frac{D\left(\frac{1}{\rho}\right)}{Dt}\right). \tag{7.30}$$

Substituting the above expression back into Eq. (7.29) and combining the two pressure terms we get

$$\left(\left(1-\frac{r}{C_p}\right)\frac{1}{p}\frac{Dp}{Dt}+r\frac{D\left(\frac{1}{r}\right)}{Dt}+\rho\frac{D\left(\frac{1}{\rho}\right)}{Dt}\right)=\frac{1}{\rho C_p T}\left(\begin{array}{c}-\sum_{k=1}^{N}h_k\dot{\omega}_k+\frac{\partial}{\partial x_i}\left(\lambda\frac{\partial T}{\partial x_i}\right)-\left(\rho\sum_{k=1}^{N}C_{pk}Y_kV_{ki}\right)\frac{\partial T}{\partial x_i}\\ +\dot{Q}+\tau_{ij}\frac{\partial u_i}{\partial x_j}+\rho\sum_{k=1}^{N}Y_kf_{k,i}V_{k,i}\end{array}\right).$$

(7.31)

Using the properties that $r=C_p-C_v$ and $\gamma=C_p/C_v$, we can get the following equation

$$\left(\frac{1}{\gamma}\frac{1}{p}\frac{Dp}{Dt}+r\frac{D\left(\frac{1}{r}\right)}{Dt}+\rho\frac{D\left(\frac{1}{\rho}\right)}{Dt}\right)=\frac{1}{\rho C_p T}\left(\begin{array}{c}-\sum_{k=1}^{N}h_k\dot{\omega}_k+\frac{\partial}{\partial x_i}\left(\lambda\frac{\partial T}{\partial x_i}\right)-\left(\rho\sum_{k=1}^{N}C_{pk}Y_kV_{ki}\right)\frac{\partial T}{\partial x_i}\\ +\dot{Q}+\tau_{ij}\frac{\partial u_i}{\partial x_j}+\rho\sum_{k=1}^{N}Y_kf_{k,i}V_{k,i}\end{array}\right). \quad (7.32)$$

Next, using the quotient rule and the chain rule of calculus, we can simplify to the following form

$$\left(\frac{1}{\gamma}\frac{D\ln p}{Dt}+\frac{1}{r}\frac{Dr}{Dt}+\frac{1}{\rho}\frac{D\rho}{Dt}\right)=\frac{1}{\rho C_p T}\left(\begin{array}{c}-\sum_{k=1}^{N}h_k\dot{\omega}_k+\frac{\partial}{\partial x_i}\left(\lambda\frac{\partial T}{\partial x_i}\right)-\left(\rho\sum_{k=1}^{N}C_{pk}Y_kV_{ki}\right)\frac{\partial T}{\partial x_i}\\ +\dot{Q}+\tau_{ij}\frac{\partial u_i}{\partial x_j}+\rho\sum_{k=1}^{N}Y_kf_{k,i}V_{k,i}\end{array}\right). \quad (7.33)$$

At this point, we can use the continuity equation to get rid of the total derivative of density and replacing it with the gradient of velocity

$$\frac{1}{\gamma}\frac{D\ln p}{Dt}+\frac{\partial u_i}{\partial x_i}=\frac{1}{\rho C_p T}\left(\begin{array}{c}-\sum_{k=1}^{N}h_k\dot{\omega}_k+\frac{\partial}{\partial x_i}\left(\lambda\frac{\partial T}{\partial x_i}\right)-\left(\rho\sum_{k=1}^{N}C_{pk}Y_kV_{ki}\right)\frac{\partial T}{\partial x_i}\\ +\dot{Q}+\tau_{ij}\frac{\partial u_i}{\partial x_j}+\rho\sum_{k=1}^{N}Y_kf_{k,i}V_{k,i}\end{array}\right)+\frac{1}{r}\frac{Dr}{Dt} \quad (7.34)$$

We can also express the conservation of momentum, Eq. (7.3), in terms of the natural log of pressure. In this case we simply need to utilize the ideal gas law, the speed of sound relationship, $c^2=\gamma p/\rho$, and some calculus and algebra manipulation

$$\rho\frac{Du_i}{Dt}+\frac{c^2}{\gamma}\frac{\partial\ln p}{\partial x_i}=\frac{1}{\rho}\frac{\partial\tau_{ij}}{\partial x_j}+\sum_{k=1}^{N}Y_kf_{ki}\ . \quad (7.35)$$

Finally, we can cleverly combine Eq. (7.34) and Eq. (7.35) by subtracting the material derivative of Eq. (7.34) from the divergence of Eq. (7.35). This provides us with the reacting wave equation in terms of $\ln p$

$$\frac{\partial}{\partial x_i}\left(\frac{c^2}{\gamma}\frac{\partial \ln p}{\partial x_i}\right)-\frac{D}{Dt}\left(\frac{1}{\gamma}\frac{D\ln p}{Dt}\right)=\frac{\partial}{\partial x_i}\left(\frac{1}{\rho}\frac{\partial \tau_{ij}}{\partial x_i}\right)+\frac{\partial}{\partial x_i}\left(\sum_{k=1}^{N}Y_k f_{ki}\right)-\frac{\partial}{\partial x_i}\left(\frac{Du_i}{Dt}\right)-\frac{D}{Dt}\left[\frac{D\ln r}{Dt}\right]+\frac{D}{Dt}\left(\frac{\partial u_i}{\partial x_i}\right)$$
$$-\frac{D}{Dt}\left[\frac{1}{\rho C_p T}\left(-\sum_{k=1}^{N}h_k\dot{\omega}_k+\frac{\partial}{\partial x_i}\left(\lambda\frac{\partial T}{\partial x_i}\right)-\left(\rho\sum_{k=1}^{N}C_{pk}Y_k V_{ki}\right)\frac{\partial T}{\partial x_i}+\dot{Q}+\tau_{ij}\frac{\partial u_i}{\partial x_j}+\rho\sum_{k=1}^{N}Y_k f_{k,i}V_{k,i}\right)\right]$$

(7.36)

The derivatives on the two velocity terms on the right hand side of the equation can be expanded and then simplified to a single term resulting in the following equation

$$\frac{\partial}{\partial x_i}\left(\frac{c^2}{\gamma}\frac{\partial \ln p}{\partial x_i}\right)-\frac{D}{Dt}\left(\frac{1}{\gamma}\frac{D\ln p}{Dt}\right)=\frac{\partial}{\partial x_i}\left(\frac{1}{\rho}\frac{\partial \tau_{ij}}{\partial x_i}\right)+\frac{\partial}{\partial x_i}\left(\sum_{k=1}^{N}Y_k f_{ki}\right)-\frac{\partial u_j}{\partial x_i}\frac{\partial u_i}{\partial x_j}-\frac{D}{Dt}\left[\frac{D\ln r}{Dt}\right]$$
$$-\frac{D}{Dt}\left[\frac{1}{\rho C_p T}\left(-\sum_{k=1}^{N}h_k\dot{\omega}_k+\frac{\partial}{\partial x_i}\left(\lambda\frac{\partial T}{\partial x_i}\right)-\left(\rho\sum_{k=1}^{N}C_{pk}Y_k V_{ki}\right)\frac{\partial T}{\partial x_i}+\dot{Q}+\tau_{ij}\frac{\partial u_i}{\partial x_j}+\rho\sum_{k=1}^{N}Y_k f_{k,i}V_{k,i}\right)\right]$$

(7.37)

The equation above is the acoustic wave equation for reacting flows. This is, of course, a very complicated differential equation and must be simplified to be able to utilize it in a practical way. Until this point, the assumptions made have been general and not very limiting. The next section will go into some of the simplifying assumptions that are appropriate for this research. It is understandable that assumptions which are made below may not apply generally, and one might have to come back to Eq. (7.37) and make appropriate assumptions based on the application.

7.2.1 Simplifying Assumptions

We can take the wave equation for reactive flows given above and analyze the different terms in the equation

$$\frac{\partial}{\partial x_i}\left(\frac{c^2}{\gamma}\frac{\partial \ln p}{\partial x_i}\right)-\frac{D}{Dt}\left(\frac{1}{\gamma}\frac{D\ln p}{Dt}\right)=\underset{\boxed{1}}{\left[\frac{\partial}{\partial x_i}\left(\frac{1}{\rho}\frac{\partial \tau_{ij}}{\partial x_i}\right)\right]}+\underset{\boxed{2}}{\left[\frac{\partial}{\partial x_i}\left(\sum_{k=1}^{N}Y_k f_{ki}\right)\right]}-\underset{\boxed{3}}{\left[\frac{\partial u_j}{\partial x_i}\frac{\partial u_i}{\partial x_j}\right]}-\underset{\boxed{4}}{\left[\cancel{\frac{D}{Dt}\left[\frac{D\ln r}{Dt}\right]}\right]}$$
$$-\frac{D}{Dt}\left\{\frac{1}{\rho C_p T}\left(\underset{\boxed{5}}{\left[-\sum_{k=1}^{N}h_k\dot{\omega}_k\right]}+\underset{\boxed{6}}{\left[\frac{\partial}{\partial x_i}\left(\lambda\frac{\partial T}{\partial x_i}\right)\right]}-\underset{\boxed{7}}{\left[\left(\rho\sum_{k=1}^{N}C_{pk}Y_k V_{ki}\right)\frac{\partial T}{\partial x_i}\right]}+\underset{\boxed{8}}{\left[\dot{Q}\right]}+\underset{\boxed{9}}{\left[\tau_{ij}\frac{\partial u_i}{\partial x_j}\right]}+\underset{\boxed{10}}{\left[\rho\sum_{k=1}^{N}Y_k f_{k,i}V_{k,i}\right]}\right)\right\}$$

(7.38)

In the wave equation above, the right hand side of the equation can be considered source terms. These source terms are not the stereotypical source terms that one would find in the study of acoustics. The pressure waves can be thought of as fluctuations in entropy due to the following processes:

1. Viscous work
2. Body forces
3. Velocity fluctuations or turbulent flow noise
4. Variations in the gas constant (assumed negligible)
5. Chemical Reaction
6. Heat conduction
7. Heat diffusion term associated with species having different enthalpies
8. Volumetric heat source
9. Viscous heating source term
10. Power production associated with species different volume forces

The key when using Eq. (7.38) is identifying the dominant sources for the system. For example, in a diffusion flame, the transport processes are more significant. For a premixed and prevaporized flame, many have postulated that the reaction process dominates. In fact, Kotake [32] shows a simple order-of-magnitude analysis for a premixed combustion process in which he found that the predominant source terms were number 3 and 5. For this research, we will make the same assumption and only keep the chemical reaction term and the turbulence term

$$\frac{\partial}{\partial x_i}\left(\frac{c^2}{\gamma}\frac{\partial \ln p}{\partial x_i}\right)-\frac{D}{Dt}\left(\frac{1}{\gamma}\frac{D\ln p}{Dt}\right)=\frac{D}{Dt}\left(\frac{1}{\rho C_p T}\sum_{k=1}^{N}h_k\dot{\omega}_k\right)-\frac{\partial u_j}{\partial x_i}\frac{\partial u_i}{\partial x_j}. \qquad (7.39)$$

For this particular research, we are dealing with relatively low-speed flows. Because of this some additional simplifying assumptions can be made [6]. To see this, let us take the quantity, f that oscillates harmonically $f=e^{-i(\omega t-kx)}$. If we examine the total derivative of this function f, we find the following result

$$\frac{Df}{Dt}=\frac{\partial f}{\partial t}+u_j\frac{\partial f}{\partial x_j}=\left(-i\omega+u_j ik\right)f=-i\omega\left(1-\frac{u_j}{c}\right)f=-i\omega\left(1-M\right)f\,, \qquad (7.40)$$

where M is the Mach number. We can see from the expression above that when the Mach number is small the convective terms in the total derivative can be considered negligible, $\left(D/Dt\sim\partial/\partial t\right)$. In addition, in low-speed flows the turbulent flow noise is small compared to those associated with chemical heat release fluctuations and therefore the last term in equation (7.39) can be neglected. Utilizing the above assumptions and utilizing the definition $\gamma = C_p / C_v$, the following form of the wave equation can be expressed

$$\frac{\partial}{\partial x_i}\left(c^2 \frac{\partial \ln p}{\partial x_i}\right) - \frac{\partial^2 \ln p}{\partial t^2} = \frac{\partial}{\partial t}\left(\frac{1}{\rho C_v T}\sum_{k=1}^{N} h_k \dot{\omega}_k\right). \tag{7.41}$$

At this point, we can linearize the above equation by considering the mean and fluctuating part of pressure, $p = \overline{p} + p'$

$$\frac{\partial}{\partial x_i}\left[c^2 \frac{\partial}{\partial x_i}\left\{\ln \overline{p} + \ln\left(1 + \frac{p'}{\overline{p}}\right)\right\}\right] - \frac{\partial^2}{\partial t^2}\left\{\ln \overline{p} + \ln\left(1 + \frac{p'}{\overline{p}}\right)\right\} = \frac{\partial}{\partial t}\left(\frac{1}{\rho C_v T}\sum_{k=1}^{N} h_k \dot{\omega}_k\right). \tag{7.42}$$

First we can make the assumption that the mean pressure is essentially constant in time and space. Secondly, we can use the Tailor series approximation and only retain first order terms $\ln\left(1 + p'/\overline{p}\right) = p'/\overline{p}$

$$\frac{1}{\overline{p}}\frac{\partial}{\partial x_i}\left(c^2 \frac{\partial p'}{\partial x_i}\right) - \frac{1}{\overline{p}}\frac{\partial^2 p'}{\partial t^2} = \frac{\partial}{\partial t}\left(\frac{1}{\rho C_v T}\sum_{k=1}^{N} h_k \dot{\omega}_k\right). \tag{7.43}$$

From here, we can make our final simplification by using the ideal gas law to eliminate mean pressure from the expression. In addition, we can make the assumptions that only plane waves are propagating in the x_1 direction

$$\frac{\partial}{\partial x_1}\left(c^2 \frac{\partial p'}{\partial x_1}\right) - \frac{\partial^2 p'}{\partial t^2} = \left(\gamma - 1\right)\frac{\partial}{\partial t}\left(\sum_{k=1}^{N} h_k \dot{\omega}_k\right). \tag{7.44}$$

This is sometimes simplified further by assuming that all specific heats are the same. Doing this results in the sensible enthalpy term going to zero

$$\frac{\partial}{\partial x_1}\left(c^2 \frac{\partial p'}{\partial x_1}\right) - \frac{\partial^2 p'}{\partial t^2} = \left(\gamma - 1\right)\frac{\partial}{\partial t}\left(\sum_{k=1}^{N} h_{fk} \dot{\omega}_k\right). \tag{7.45}$$

However, in this work we will not assume that specific heats are all the same and therefore Eq. (7.44) will be the expression that we use.

7.3 Flame compared to a loudspeaker

The wavelengths associated with most longitudinal combustion oscillations are usually large compared to the size of the combustion zone. When this is the cases, the flame can be considered "compact" compared to acoustic wavelengths. The following analysis uses the idea of a "compact" flame to define jump conditions for acoustic quantities through the flame front [6]. Fig. 7.1 shows a simplified drawing of our "compact" flame.

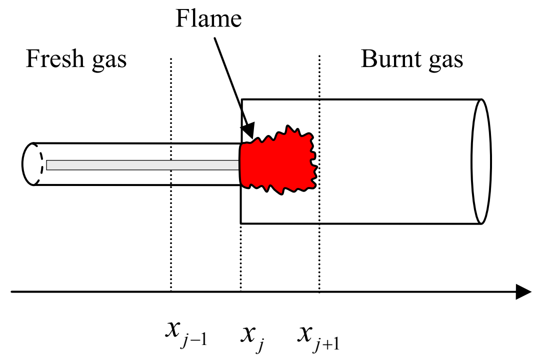

Fig. 7.1: Schematic of compact flame

For this analysis, we need to utilize the relationship between acoustic pressure and velocity given in Eq. (7.6), as well as the energy relationship found from Eq. (7.34). In the expressions below, the simplifying assumptions that were outlined in the section above are also used in this analysis

$$\frac{\partial u}{\partial t} = -\frac{1}{\rho}\frac{\partial p'}{\partial x}, \tag{7.46}$$

$$\frac{1}{\gamma p_o}\frac{\partial p'}{\partial t} + \frac{1}{S}\frac{\partial}{\partial x_1}\left(Su\right) = \frac{\gamma - 1}{\gamma p_o}\frac{\partial \dot{Q}}{\partial t}. \tag{7.47}$$

where $\frac{\partial \dot{Q}}{\partial t}$ is equal to $\frac{\partial}{\partial t}\left(\sum_{k=1}^{N} h_{fk}\dot{\omega}_k\right)$ and S is the cross-sectional area. In the equations above, the subscript 1 has been dropped from the acoustic velocity and it is simply implied that the acoustic waves are propagating in as plane waves in the x_1 direction. We can integrate equation (7.46) and (7.47) from x_{j-1} to x_{j+1} and taking the limit where x_{j-1} and x_{j+1} approach x_j and we obtain the following:

$$p'(x_{j-1}) - p'(x_{j+1}) = 0, \tag{7.48}$$

$$S_{j+1}u'(x_{j+1}) - S_{j-1}u'(x_{j-1}) = \frac{\gamma - 1}{\rho_j c^2{}_j}\frac{\partial \dot{Q}}{\partial t}. \tag{7.49}$$

From Eq. (7.48), we find that the pressure does not change across the flame. However, Eq. (7.49) shows that the acoustic velocity does change across the flame. Consequently, the thin flame acts as a volume flow rate source similar to a "loudspeaker". This effect is due to the strong expansion of the fluids in the combustion zone.

7.4 Flame as a Volumetric Acceleration

We can further compare the flame to a loudspeaker by looking at the differential equation. First, we can take a look at the 1-D acoustic wave equation with the flame as the source. From Eq. (7.44), we have the following expression

$$\frac{\partial}{\partial x_1}\left(c^2 \frac{\partial p'}{\partial x_1}\right) - \frac{\partial^2 p'}{\partial t^2} = (\gamma - 1)\frac{\partial}{\partial t}\left(\sum_{k=1}^{N} h_k \dot{\omega}_k\right). \tag{7.50}$$

We can compare the above equation to the differential wave equation with a loud speaker as the source

$$\frac{\partial}{\partial x_1}\left(c^2 \frac{\partial p'}{\partial x_1}\right) - \frac{\partial^2 p'}{\partial t^2} = \gamma \overline{p}\frac{A_s}{A_c} a_o, \tag{7.51}$$

where a_o is the acceleration of the speaker diaphragm, A_s is the cross-sectional area of the speaker, and A_c is the cross-sectional area of the combustor. Equating the right hand side of Eqs. (7.50) and (7.51), we obtain the following expression

$$(\gamma - 1)\frac{\partial}{\partial t}\left(\sum_{k=1}^{N} h_k \dot{\omega}_k\right) = \gamma \overline{p}\frac{A_s}{A_c} a_o. \tag{7.52}$$

Here we can assume that the cross-sectional area of the flame and combustor are essentially equal $(A_s \approx A_c)$. Using this assumption and rearranging the above equation, we get the following relationship

$$\frac{\partial}{\partial t}\left(-\sum_{k=1}^{N} h_k \dot{\omega}_k\right) = \frac{\partial \dot{Q}}{\partial t} = \frac{\gamma \overline{p}}{(\gamma - 1)} a_o. \tag{7.53}$$

Here we have also replaced the heat release rate term in parenthesis with $\dot{Q}$ for simplicity.

Our end goal is to get a transfer function between the acoustic velocity as the output and the flame heat release rate as the input. In addition, we would like to replace the heat release rate with an equivalent acceleration source. This can be achieved by taking the Laplace transform of Eq. (7.53) and solving for the appropriate transfer function. The acoustic transfer function then becomes

$$TF = \frac{u'}{\dot{Q}} = \frac{\gamma \overline{p}}{s(\gamma - 1)}\left(\frac{u'}{a_o}\right), \tag{7.54}$$

where s is the Laplace transform variable. In ABAQUS, an acceleration source is integrated over the surface and therefore making the source term a volumetric acceleration, VA. Equation (7.54), in terms of a volumetric acceleration, is expressed as follows

$$TF = \frac{u'}{\dot{Q}} = \frac{\gamma \overline{p} A_c}{s(\gamma-1)} \left(\frac{u'}{VA} \right), \tag{7.55}$$

where A_c is the cross-sectional area of the combustor at the flame location.

In order to properly obtain the transfer function given in Eq. (7.55), we need to break it into two separate transfer functions as shown in the schematic below.

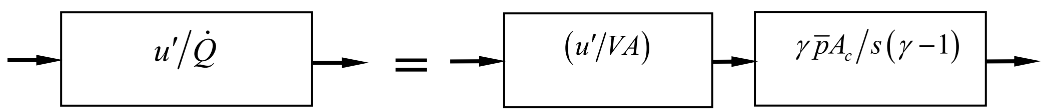

Fig. 7.2: The acoustic transfer function can be broken into two transfer function as shown in the schematic

In ABAQUS, we can model the flame as a volumetric acceleration of amplitude $(1+0i)\, m^3/s^2$. The acoustic velocity at a given point of interest in the model will be the FRF of the velocity with respect to the volumetric acceleration source. This FRF extracted from the model can be transformed to the Laplace domain through the use of curve fitting routines. MATLAB has a very good routine called "invfreqs". This command finds the transfer function that corresponds to a given complex frequency response. Consequently, we can obtain the transfer function, (u'/VA) which will have the following form

$$\frac{u'}{VA} = \frac{a_n\ s^n + a_{n-1}\ s^{n-1} + \ldots \qquad + a_1\ s + a_o}{b_n s^n + b_{n-1}\ s^{n-1} + \ldots \qquad + b_1\ s + b_o} \tag{7.56}$$

The other transfer function, $\gamma \overline{p} A_c / s(\gamma-1)$, is simply a constant with a negative 90 degrees phase shift. The phase shift is due to the Laplace variable, s in the denominator. Since the two transfer functions shown in Fig. 7.2 are in series, they are simply multiplied together resulting in the appropriate acoustic transfer function, $u'/\dot{Q}$.

As was mentioned in the Introduction, the acoustic transfer functions were extracted immediately upstream of the flame and at the fuel lines. This was the method used in this research to obtain the acoustic transfer functions for the reduced-order thermoacoustic model.

Chapter 8

8 Validation of Hot-acoustics

8.1 Experimental Procedure

Experimental validation of the hot-acoustic FE model was needed to ensure that our approximation of the physics discussed in Chapters 6 and 7 was adequate. This type of experimental validation is challenging since it can be difficult to measure the flame as an acoustic source. Likewise, it can also be challenging to make measurements at high temperature conditions.

Under the hot conditions, measuring the modes shapes would have been very complicated. Consequently, the method of choice for validating the hot-acoustic model was to measure frequency response functions. This was done using pressure or velocity as the output and the dynamic heat release as an input. The pressure was measured with a microphone, and the velocity measurement used the two microphone technique described earlier.

The dynamic heat release was quantified by measuring *OH** chemiluminescence. *OH** is an intermediate species created in hydrocarbon flames which has been shown by Haber et. al [33] to be a good indicator of the heat release rate. Using an optical bandpass filter and photomultiplier tube, one can focus in on the specific wavelength of light emitted by OH*, 307.81 *nm*. In our laboratory combustion rig, the flame is surrounded by a clear quartz section which provided an optical path for the photomultiplier tube to pick up the incident radiation of the flame. Lee and Santavicca, as well as others, have also used this method for measuring dynamic heat release of flames [34].

The pressure, velocity, and the dynamic heat release measurements were recorded using either an HP Digital Signal Analyzer or National Instruments Data Acquisition hardware and software. In processing the FRF's, about 100 averages were performed. Fig. 8.1 below shows the instruments that were used and the locations were the measurements were taken.

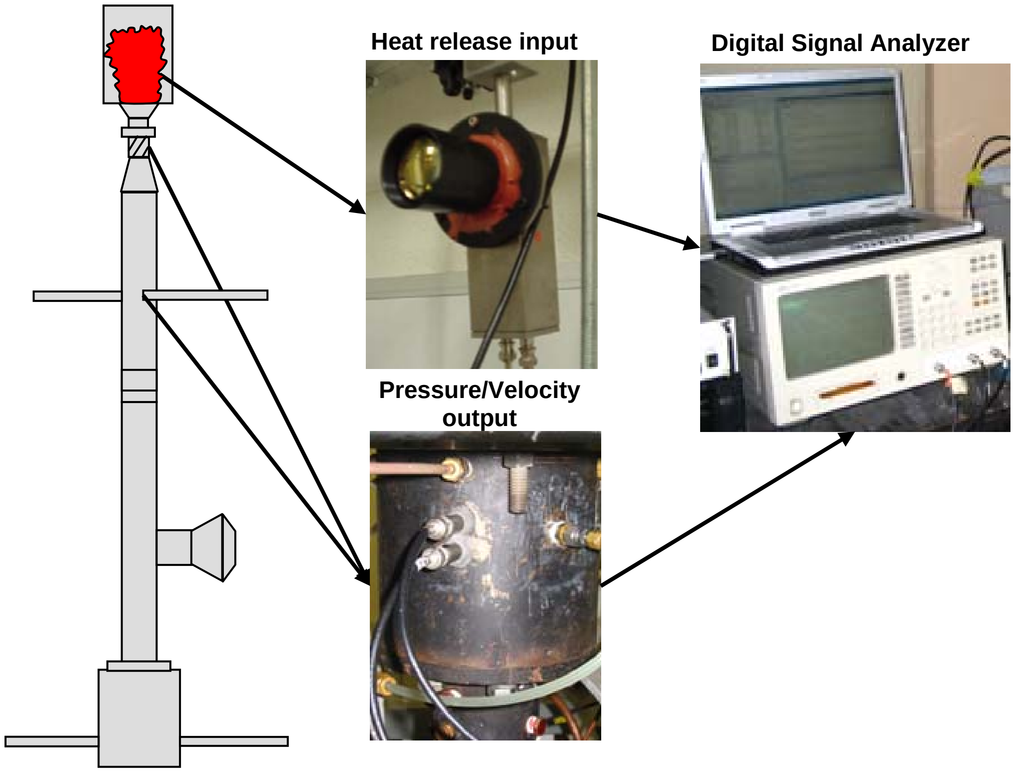

Fig. 8.1: High temperature experimental acoustic validation

Since the combustor is inherently a feedback system in order to obtain the acoustic transfer functions or FRF's, we need to ensure that we had broken the feedback loop and were measuring just the open loop acoustic frequency response. This can be seen by looking at the block diagram of the simple feedback model which involves only the flame dynamics and the acoustics.

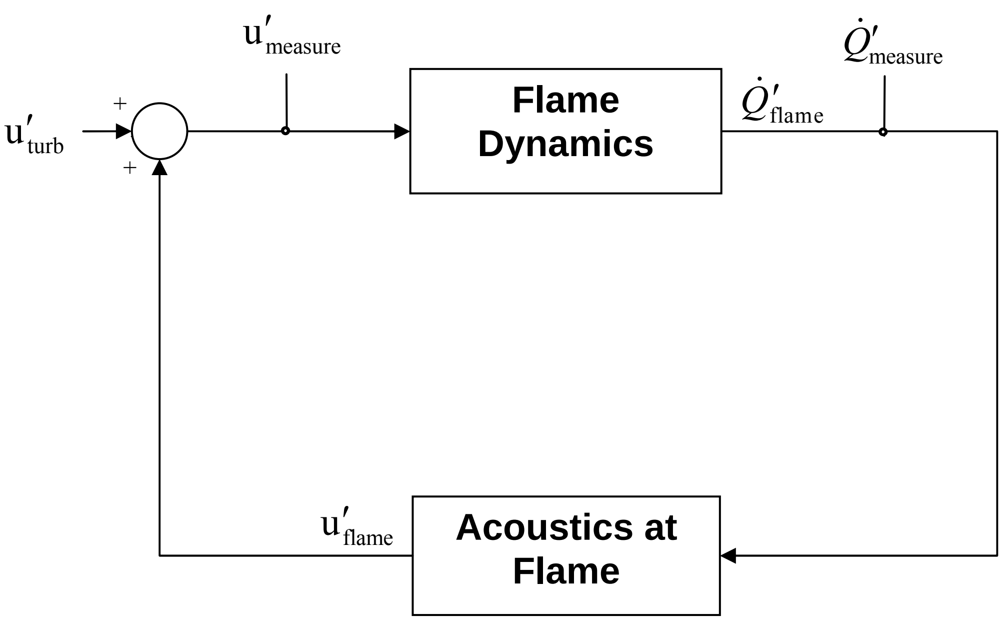

Fig. 8.2: Block diagram of simple model of the thermoacoustic feedback system

The acoustic frequency response function can be found by taking $\dot{Q}'_{meas}$ as the input and u'_{meas} as the output

$$FRF = \frac{u'_{meas}}{\dot{Q}'_{meas}} \tag{8.1}$$

As can be seen from the block diagram, $\dot{Q}'_{meas}$ is equal to $\dot{Q}'_{flame}$. In addition, we can get the following relationship for the acoustic velocity

$$u'_{meas} = u'_{flame} + u'_{turb}\,. \tag{8.2}$$

Since the flowrate is relatively low (25 SCFM), we can consider u'_{turb} to be negligible compared to u'_{flame}. Therefore, we obtain

$$u'_{meas} = u'_{flame}\,. \tag{8.3}$$

With this knowledge, the measured frequency response function can be simplified to

$$TF = \frac{u'_{flame}}{\dot{Q}'_{meas}}\,. \tag{8.4}$$

This is the open loop frequency response function that we are trying to predict with the finite element acoustic model. The case shown above refers to velocity as the acoustic output. However, pressure could also be used as the output since velocity is proportional to the gradient of pressure.

Frequency response functions with both pressure and velocity as the output were measured and shown below. The results from these measurements are compared in the to the hot-acoustic FE model.

8.2 Results

In Fig. 8.3 through Fig. 8.6, a comparison is made between the experimental data and the FE model results. In these figures, plots of different FRF's are shown. It can be seen in these comparisons that there is pretty good correlation in both magnitude and phase between the hot-acoustic finite element model and the experimental data. However, particularly with the velocity and in the lower frequency range of the pressure, the experimental FRF's suffer from excessive noise in the signal. In the pressure signal, this can be seen particularly between 0 and 100 Hz where the coherence has dropped to almost zero. Since the coherence has been lost in the lower frequency range, the magnitude and phase in this region would not be expected to match.

The velocity measurement also comes out to be very noisy. This is mainly due to our two microphone measurement technique. Using this technique, the two microphone pressure signals are subtracted (see appendix A). Since the two signals are very close to each other, any noise inherent in the signals will be amplified in the resulting velocity.

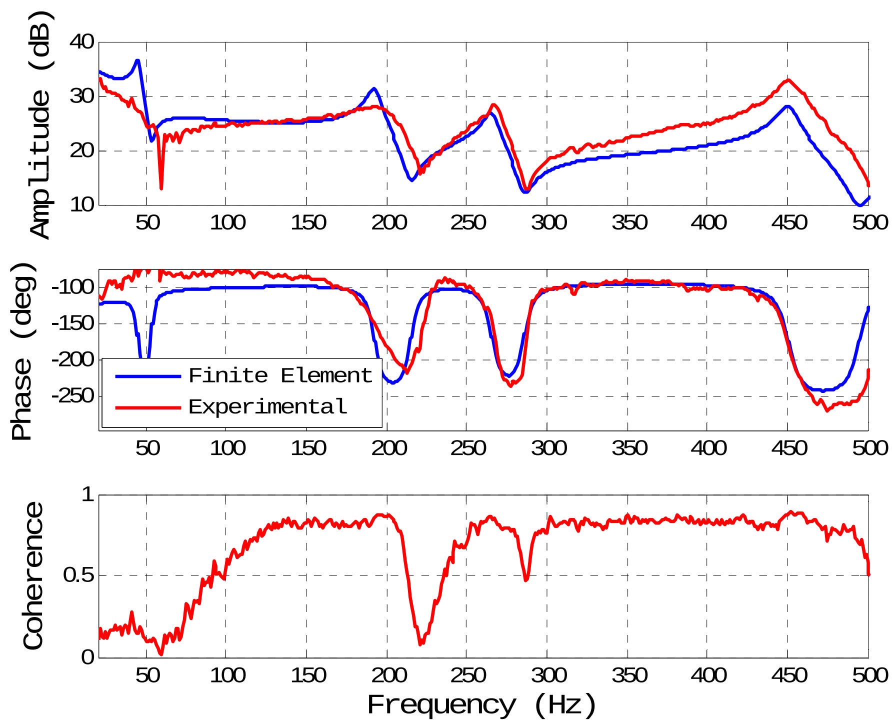

Fig. 8.3: Frequency Response plot with flame acting as the acoustic source and a microphone measuring the acoustic pressure 3" upstream of the flame

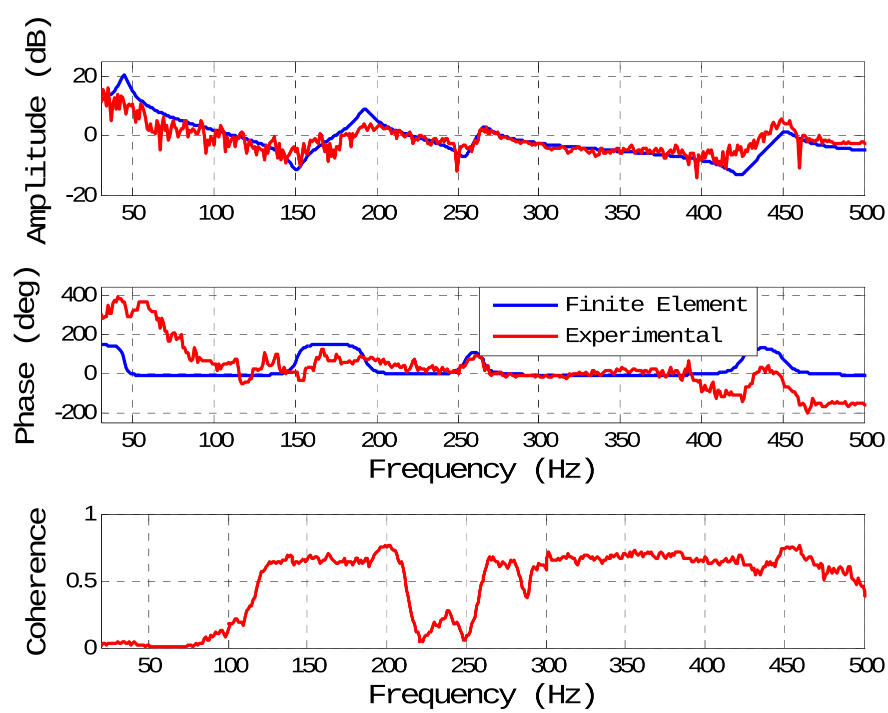

Fig. 8.4: Frequency Response plot with flame acting as the acoustic source and a two microphone probe measuring the acoustic velocity 3" upstream of the flame

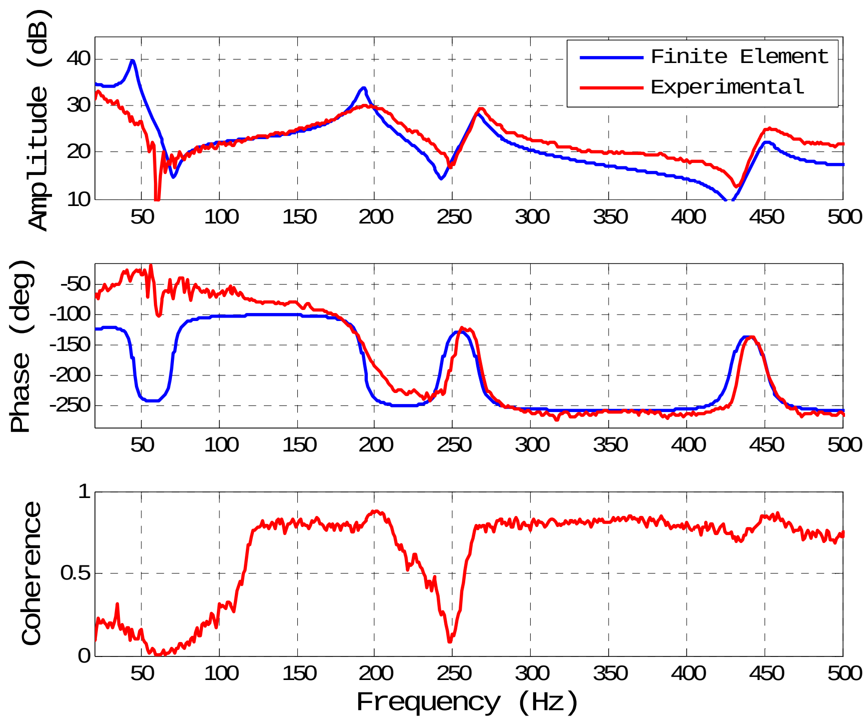

Fig. 8.5: Frequency Response plot with flame acting as the acoustic source and a microphone measuring the acoustic pressure a foot and a half upstream of the flame

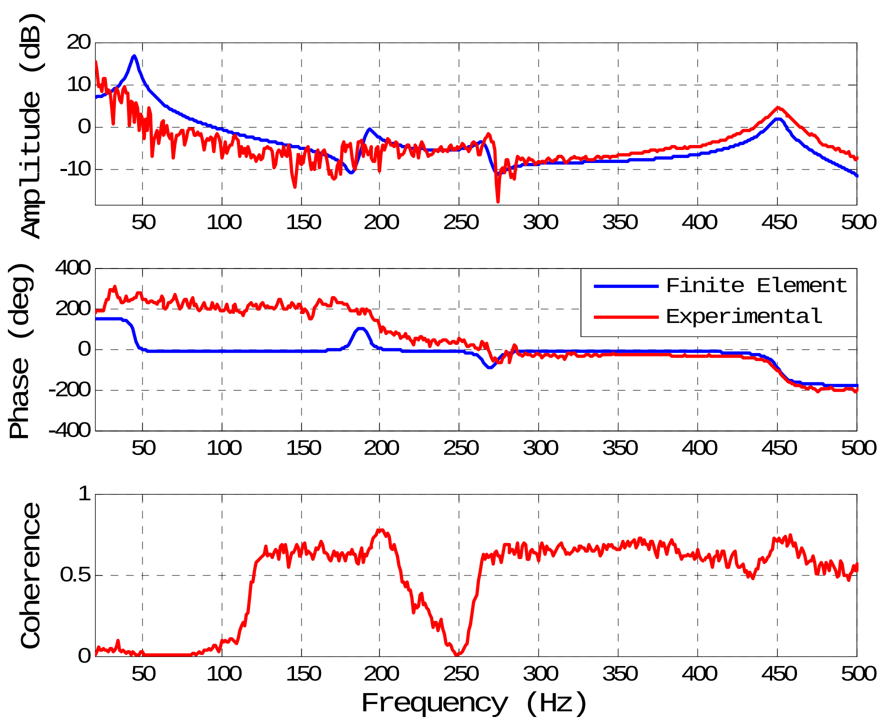

Fig. 8.6: Frequency Response plot with flame acting as the acoustic source and a two microphone probe measuring the acoustic velocity a foot and a half upstream of the flame

There are several possibilities for why the coherence is so low in the lower frequency range. The most sensible reason is that the flame and consequently the acoustics are not excited at these frequencies. The flame is driven by the inherent turbulence in the system. In our experimental rig, the turbulent structures are relatively small and therefore having high corresponding frequency content. Consequently, the flame is barely exciting the acoustics in this lower frequency range, below 100 Hz.

8.3 Validation of Extended Combustor

An extension to the combustor was added to allow the combustor to go unstable. This was beneficial by providing a means to investigate stability trends and issues. A detailed discussion of thermoacoustic stability insights will be given in Chapter 9. In this chapter, we will utilize our modified laboratory combustor to further validate the hot-acoustic FE modeling. The figure below show the modified combustor with the extended section highlighted with a dashed red box.

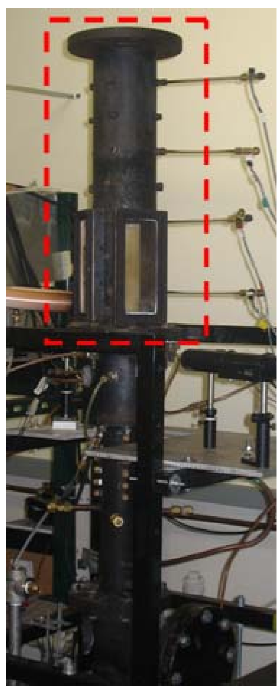

Fig. 8.7: Picture of the laboratory combustor with an extended section outlined in red

The modified rig now has an extended section downstream of the flame. This allows us to investigate a model which contains more temperature dependency, due to the fact that about half of the combustor is now heated and the other half is still about room temperature. The actual temperature profile was approximated using the estimated adiabatic flame temperature and thermocouple measurements. The Fig. below shows the resulting estimated temperature profile.

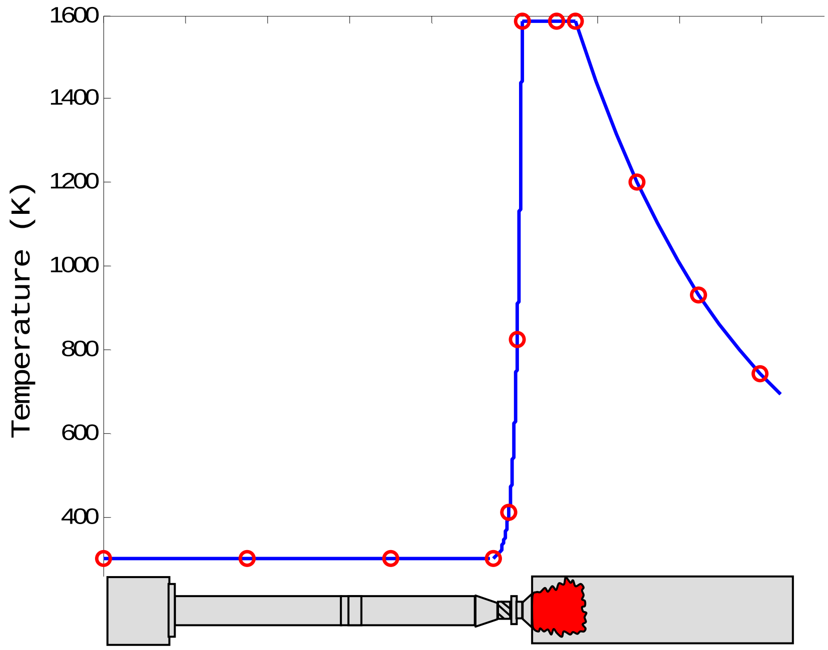

Fig. 8.8: Temperature distribution with an extended section added downstream of the flame

The frequency response function method of validation was utilized. Once again, the pressure and velocity were used as the output of the FRF and heat release rate was used as the input. However, this time the measurements were only taken at one location, 3 ½ inches upstream of the flame.

With the addition of the extended section, some complexity was added to the dynamic heat release measurement. Now, instead of the flame being completely visible, it was only visible through a 3” x 8” window. This resulted in a lack of visibility for the PMT. Consequently, the signal to noise ratio for the *OH** dynamic heat release measurement was significantly reduced. The result of loss of *OH** signal intensity can be seen in the figures below with increased noise in the magnitude and phase and less coherence. This is especially evident in the velocity FRF.

The pressure measurement was again made with a PCB microphone. However, the velocity data for this test was taken with a hotwire. This was done because the signal to noise ratio was so low that the two microphone probe renders essentially unusable results. The hotwire improves the quality of the FRF data somewhat, although as shown below, it is not very good data with very low coherence. However, the pressure FRF data is still relatively good and one can see that there is good correlation between the model and the experimental results. It would be difficult to determine the exact cause the deviations in the model. However, it should be noted that the temperature distribution used in the FE model was a very rough approximation and might not have been a good estimate of the actual temperature distribution that was present when this data was recorded. As seen in Chapter 6, the temperature profile can have a large impact on the accuracy of the acoustic response.

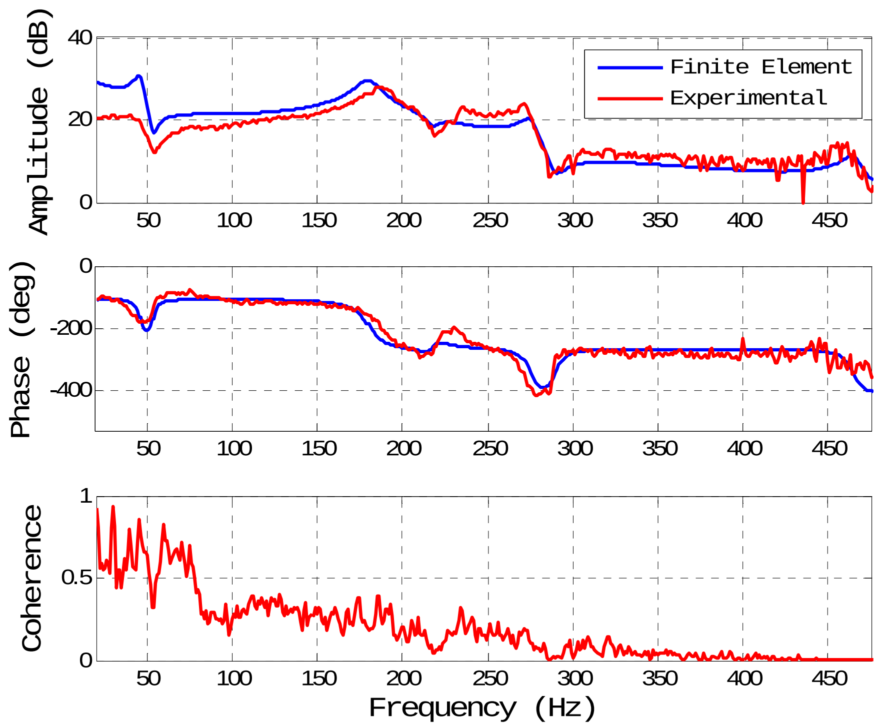

Fig. 8.9: FRF plot for the combustor with an extended section and with flame acting as the acoustic source and a microphone measuring the acoustic pressure 3" upstream of the flame

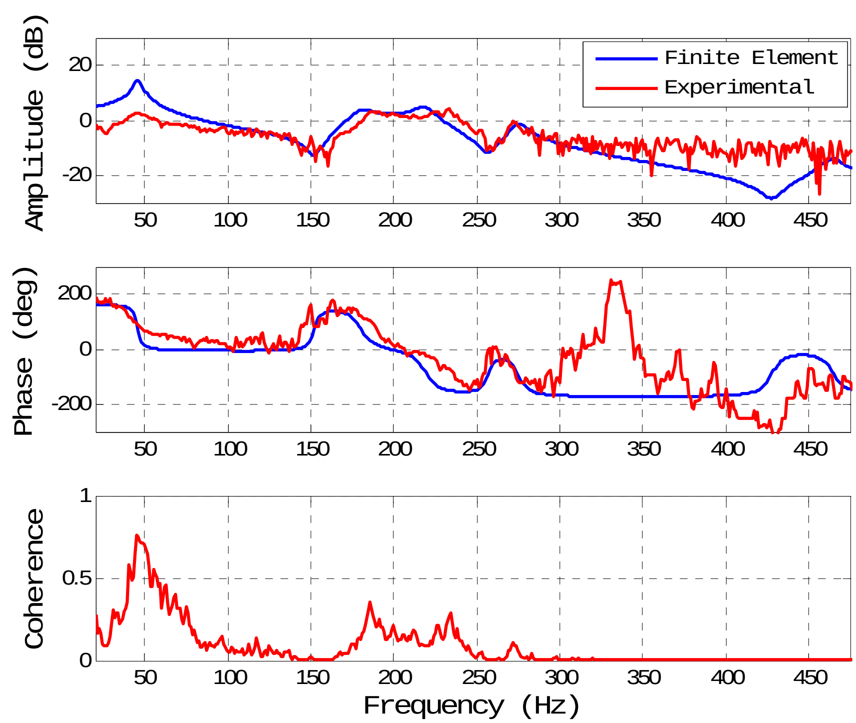

Fig. 8.10: FRF plot for the combustor with an extended section and with flame acting as the acoustic source and a hotwire measuring the acoustic velocity 3" upstream of the flame

It can be observed in the two figures above that the coherence in the lower frequency range does not drop off as much for this extended combustor. This might be explained using the same argument presented previously that the acoustic waves which are excited depend on the fluid dynamics of the flame region. Now that the downstream section of the combustor has been extended, it is conceivable that, local to the flame, the combustor might be capable of sustaining larger fluid dynamic turbulent or wave structures which would correspond to lower frequencies of flame excitation. This would explain the improved coherence in the lower frequency range.

In summary, as can be seen from this chapter, the complete hot-acoustic finite element model has good correlation with the experimental data. This seems to indicate that both the FE representation of the temperature gradients and the flame as an acoustic source are adequate for our laboratory combustor system.

Chapter 9

9 Insights and Application

In this chapter, some insights into system stability are made by looking at the acoustic FRF's and the reduced-order model. In addition, application to an industrial size gas turbine engine is briefly explored.

9.1 Insights for System Stability

The original configuration of the combustor, as seen in Fig. 4.1, had the flame essentially open to atmospheric pressure. Under this configuration, the acoustic energy near the flame was relatively low. Therefore, the combustor was unable to go unstable. In order for the laboratory combustor to go unstable, an extended section was added downstream of the flame. A picture of the extended section is shown in Fig. 8.7. With this extension, the acoustic waves near the flame can have a much higher intensity. In dynamic systems terminology, extending the combustor allowed us to turn up the gain of the system. Consequently, the laboratory combustor could go unstable at certain operating conditions. This chapter will provide some insights into system stability predictions.

To fully understand the stability limits of a combustion system, the full closed-loop model must be explored. However, one can still gain insight into the stability of the system by examining the only acoustics. In doing this, let us first take note of the acoustic resonant frequencies and compare them to the experimentally observed instability frequencies. The first four columns of the table below are the acoustic resonance frequencies at different locations determined by the FE model. The last column shows the two dominant instability frequencies of the combustor. One can see that the two instability frequencies are close to the 2nd and 3rd acoustic resonant frequencies predicted by the FE model.

One would expect instability frequency to deviate a little from the acoustic resonance as the acoustics couple with the flame dynamics. From a controls point of view, the flame dynamics couple with the acoustics to alter the roots of the characteristic equation. The roots of the characteristic equation mathematically predict the instability frequency. However, in general, the instability frequencies are very close to the acoustic resonances of the system.

Table 9.1: A list of the acoustic pressure and velocity resonance frequencies determined from the FE model and the experimentally determined dominant instability frequencies

Pressure upstream	Pressure downstream	velocity upstream	velocity downstream	instability frequency
45 Hz	44 Hz	46 Hz	44 Hz	
180 Hz	179 Hz	182 Hz	178 Hz	184 Hz
227 Hz	220 Hz	218 Hz	219 Hz	230 Hz
274 Hz	277 Hz	276 Hz	278	
464 Hz		465 Hz		
604 Hz		610 Hz		

To get a better feel for the relative strength of these different resonance peaks, we can look at the frequency response plots for pressure and velocity at the different locations. Fig. 9.1 and Fig. 9.2 show the FRF's of the acoustic pressure relative to the flame heat release. The FRF's are taken 3" upstream and 4" downstream of the flame respectively.

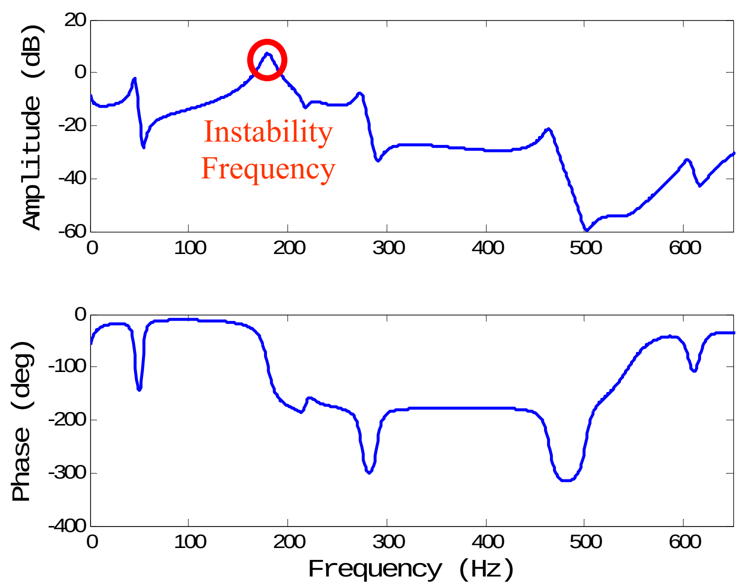

Fig. 9.1: FRF from FE model for the acoustic pressure 3" upstream from the flame relative to the heat release of the flame

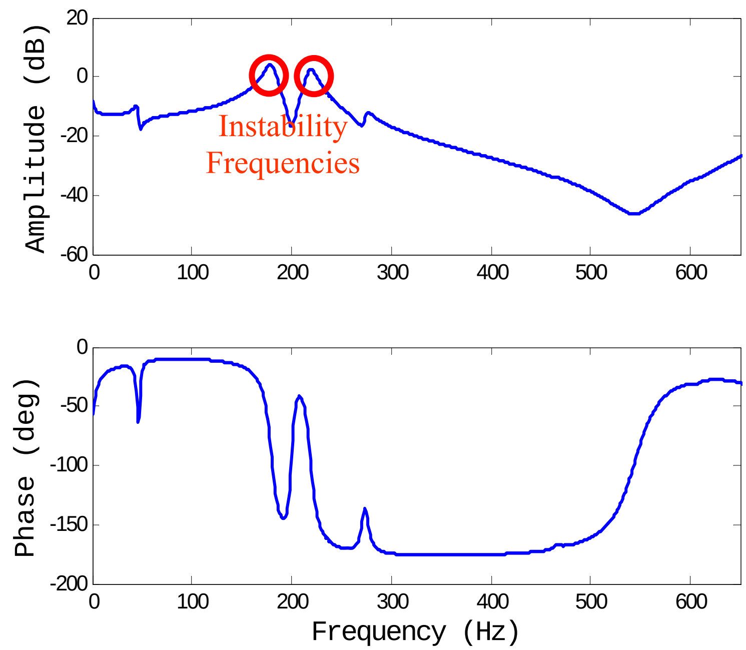

Fig. 9.2: FRF from FE model for the acoustic pressure 4 inches downstream of the flame relative to the heat release of the flame

There are several interesting characteristics that we can observe from looking at these two plots. In both, the highest peak is about 180 Hz. In comparison, the most dominant thermoacoustic instability experimentally observed in our rig occurs at about 184 Hz. The second most dominant instability occurs at 230 Hz which is also a strong peak in Fig. 9.2. From these two plots, we can see that the strength of the acoustic pressure modes might be an indication as to which acoustic modes might go unstable.

Another interesting point can be observed by looking at the acoustic velocity FRF's. When examining linear feedback systems, we can get an indication for stability by looking at a quantity called phase margin. This criterion states that the system will go unstable whenever there is a 180 degree phase crossing and a corresponding magnitude greater than 1-DB. In order for the condition of phase margin to be valid, the acoustic and flame dynamic FRF's would need to be combined. However, one can get some indication of were potential stability problems would occur by looking at places in the acoustic FRF that have significant phase lag with a corresponding large relative magnitude. When such acoustics are coupled with the flame dynamics, the system becomes ripe for instability.

Fig. 9.3 and Fig. 9.4 show the acoustic velocity relative to the heat release of the flame. These plots were taken 3" upstream and 4" downstream of the flame respectively. As annotated on the plots, large phase lag can be observed between the frequencies of 180 and 230. These two frequencies are very close to the two experimentally determined instability frequencies of the laboratory combustor.

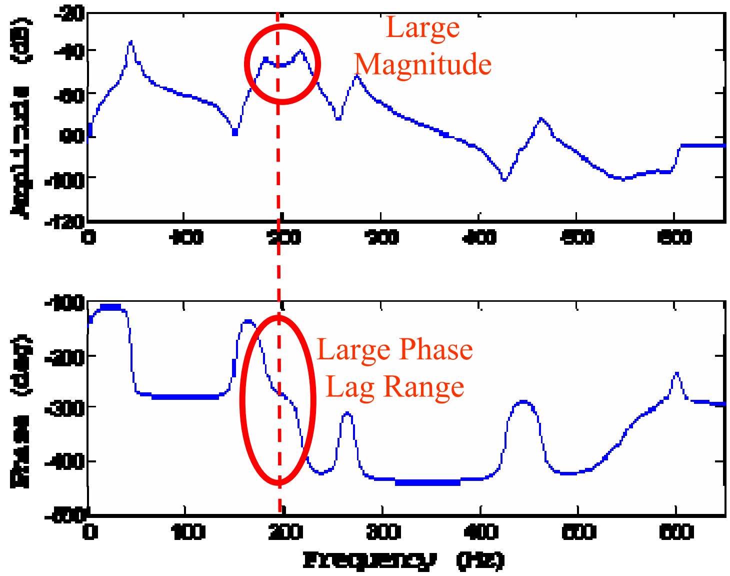

Fig. 9.3: FRF from finite element model for the acoustic velocity 3 inches upstream from the flame relative to the heat release of the flame

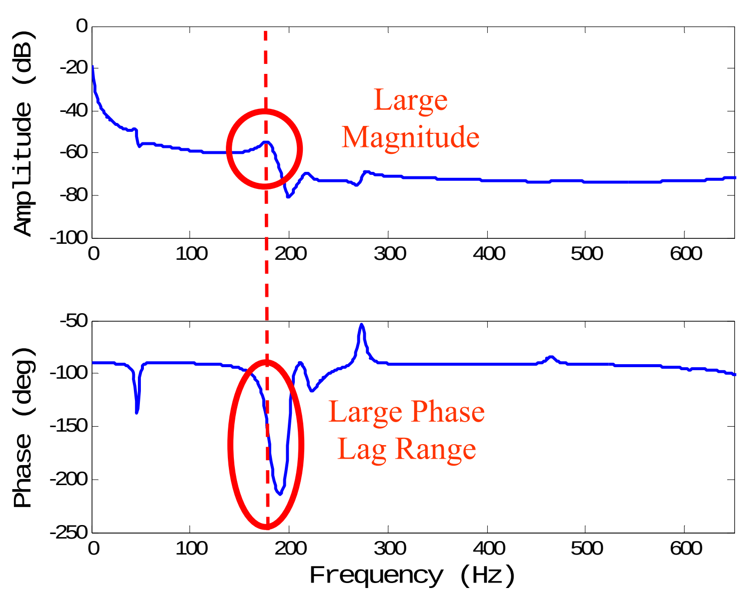

Fig. 9.4: FRF from finite element model for the acoustic velocity 4 inches downstream of flame relative to the heat release of the flame

By simply looking at the FRF plots of pressure and velocity relative to the heat release of the flame, one can get a feel for the likelihood of instability and the potential frequencies where those instabilities might occur.

As stated above, in order to have a more confident prediction of where and when instability might occur, the acoustics needs to be combined with the other dynamics in the closed-loop reduced-order model. The other dynamics consist of the flame, mixing, and time delay as shown in Fig. 1.1. In a collaborative effort with Chris Martin of the VACCG, the acoustic transfer functions described in this thesis were combined with the flame dynamic model developed by Martin [10]. The result of this effort is a stability map which can be seen in the figure below. This plot maps the stability of the combustor with respect to the mean operating conditions. The x-axis in this plot is the mean equivalence ratio and the y-axis is the mean mass flow rate. The red lines on this graph represent the stability limits, and the black line represents the flame blow out limits. In addition, the green circles on the plot represent the experimentally observed operation conditions at which the combustor has gone unstable. One can see that the general behavior of the model and the experimental data are well correlated.

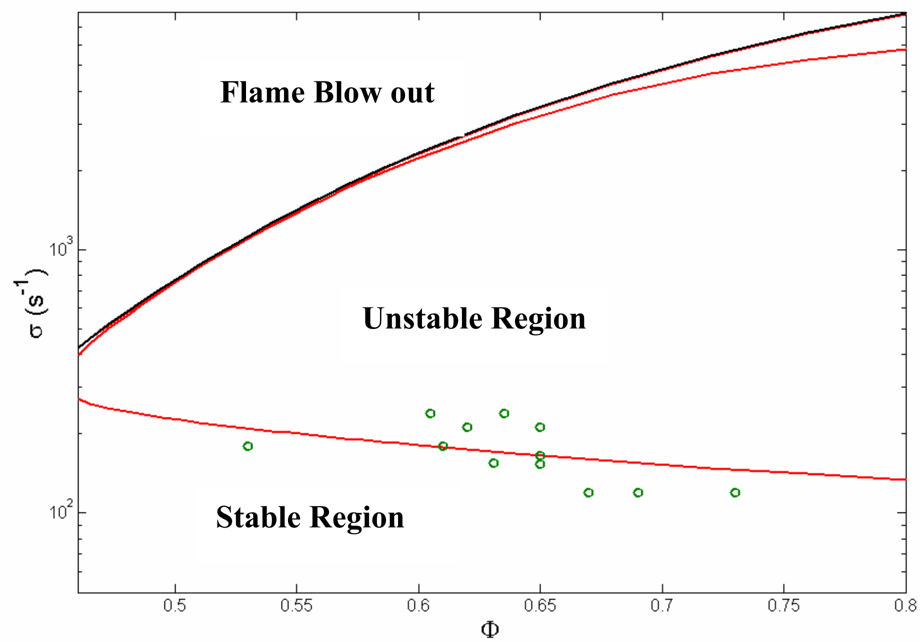

Fig. 9.5: Stability map developed from the acoustic transfer functions coupled with the flame transfer functions. The y-axis represents the mean mass flow rate and the x-axis represents the mean equivalence ratio. Green circles are experimentally observed instability points [10]

9.2 Application for an industrial Gas turbine engine

In this thesis, the modeling of a laboratory-scale combustor was outlined. The success in this modeling effort was very good. However, making the transition from a laboratory-scale combustor to an industrial scale gas turbine engine is a daunting task and involves resolving several key issues.

The first issue that needs to be resolved is to determine what extent of the engine you will model. It is probably not possible to model every complex part inherent in a gas turbine engine and it is certainly not practical. Since the coupling of the flame and acoustics occurs in the combustor region of the engine, it is logical to limit the model to that region.

If one adopts this idea, the question arises as to what boundary condition should be specified in the model to account for the compressor and turbine. In addition, one could also cut any fuel lines and injectors and specify an equivalent boundary condition for each of these. In an acoustic model, the appropriate type of boundary condition would typically be acoustic impedance. It has been observed from this study that to accurately characterize the combustor acoustics, a good representation of these boundary conditions must be realized.

One could potentially obtain this quantity through experimental measurement. Since the impedance is the ratio of acoustic pressure and velocity, one would need an accurate measure of both of these quantities at the points of interest. In addition, some sort of spatial average over the cross-section would probably be needed. With modern instrumentation continually improving, there are now small probes that can give relatively good estimates of both pressure and velocity at a given point. In fact, there have been some attempts to experimentally measure boundary impedance which can be specified in the model [18]. Another approach might be developing ways to obtain the impedance through analytical or numerical methods. In either case, acquiring the equivalent impedance at these boundaries is not an easy task and more work needs to be done in this area.

A second aspect that was not addressed in this thesis is the coupling of other types of acoustic modes. There are three types of acoustic modes that can be manifest in the combustor: longitudinal, circumferential, and transverse. Since the thermoacoustic instabilities in lean premixed gas turbine engines are typically a low frequency phenomenon, normally only the longitudinal and circumferential modes will couple with the flame. The transverse modes are higher frequency modes that set up in the transverse direction of the combustor.

As is evident from this thesis, a 1-D acoustic FE model does an excellent job in predicting the acoustic characteristics attributed to longitudinal modes. However, in many industrial gas turbine engines, the combustor section is composed of an annulus with the flame stabilizing on multiple injectors. In such a combustor, circumferential acoustic modes are commonly observed. To capture these modes, we could develop a 1-D annular acoustic model. Fig. 9.6 below shows how this might be done.

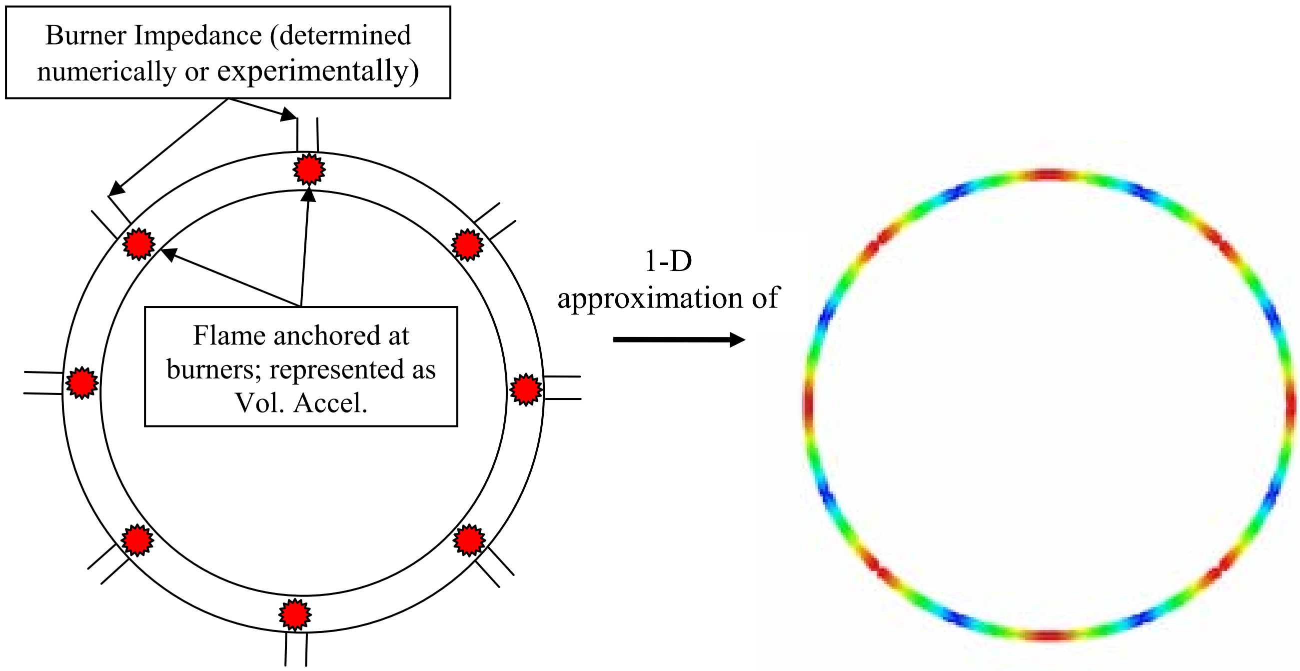

Fig. 9.6: Modeling approach for predicting the circumferential modes for a gas turbine engine with an annular combustor

The above schematic is very simple and is shown here to merely give a general idea as to how one might model the circumferential acoustics using a 1-D acoustic model [18].

Lastly, if transverse modes are significant based on the flame dynamics and combustor geometry, a 3-D acoustic FE model could be generated. However, even in such a case, the 3-D model could likely incorporate sections where 1-D modeling would be appropriate. If a 3-D model were to be used, an accurate spatial representation of the volumetric acceleration source would be needed. Independent of the type of model used, much of the work presented in this thesis could either be applied directly or modified to achieve accurate acoustic transfer functions need for the thermoacoustic reduced-order model.

Chapter 10

10 Conclusion and Future Work

10.1 Summary

Currently, many gas turbine engines are forced to limit their operating conditions due to thermoacoustic instabilities. Consequently, the task of understanding, predicting, and controlling thermoacoustic instabilities is of vital importance. Studies, such as this one, will hopefully result in improved understanding, modeling capability, and design tools for the combustion community. Such tools can help academia and industry push forward with improved engine designs that will reduce the problem of thermoacoustic instabilities.

The overall goal of the research presented in this thesis was to obtain accurate acoustic transfer functions to couple with thermoacoustic models for stability predictions. At the onset of this study, it was hypothesized that the finite element method could be utilized to adequately predict the needed transfer functions. Through this research, it was found that the finite element method can be used to successfully characterize the acoustics and produce transfer functions that correlate very well with experimental measurements.

As discussed in the introduction, these transfer functions can be coupled with the reduced-order models of the flame dynamics, mixing, and time delay to produce closed-loop predictions for overall stability of the system. It can be seen that the acoustic transfer functions coupled with the reduced-order model can predict the instability regions with relatively good accuracy.

10.2 Key Results

10.2.1 Cold Acoustic Model

Before introducing the complexity inherent in the flame, a simple "cold acoustic model" was developed and validated. One of the important aspects of this part of the modeling process was the tailoring of the model to the physics and scale of the problem. In premixed combustion, it is widely accepted that the flame will only respond to low frequency perturbations which effectively make the flame act like a low-pass filter. This results in a very low frequency range of interest. In this low frequency range only 1-D longitudinal acoustic waves will propagate. This assumption will hold true unless the cross-sectional dimensions are large enough for the low frequency wavelengths to set up in the transverse or circumferential direction. For the laboratory combustor, the physics of the flame and scale of the combustor warrant a 1-D acoustic FE model. The FE model was 3-D in space, but the acoustic waves were only permitted to propagate in one-dimension.

With this simplifying assumption, the FE development and computation time was significantly reduced. However, due to this approach, complex geometry and boundary conditions needed to be appropriately represented in a 1-D sense. This was primarily accomplished by researching well established analytical approximations for how acoustic plane waves interact with the different complex geometries and boundaries. As a result, equivalent cross-sections, lengths, and impedances were used. For example, it was found that a plate with many tiny perforations can be modeled as an orifice plate with an equivalent cross-section and adjusted thickness. This approximation and all others hold true as long as the acoustic wave lengths are large compared to the characteristic dimensions of the different geometries. In Chapter 4, these simplification methods are described in more detail.

Once the “cold acoustic model” had been developed and refined, a method for validating the model was essential. Two separate means of validation were employed. One technique was to compare the analytical and experimental mode shapes with those from the FE model. This was done and produced compelling evidence for the accuracy of the model. As a further means of validation, frequency response functions at discrete locations were measured and again compared to the model. Once again, the comparison showed that the model was highly correlated with the experimental data which gave a reassurance that the finite element model had accurately captured the “cold acoustic” response. Plots of this comparison can be seen in Fig. 5.2 through Fig. 5.7.

10.2.2 Temperature Effects

Once the “cold acoustic model” was developed and validated, inclusion of the flame in the model was the next step. This has been referred to in this thesis as the “hot-acoustic model”. As stated above, it was believed at the onset of this study that the presence of the flame alters the acoustic response significantly. There are two main areas of added complexity corresponding to the addition of the flame. The first is accounting for dependency of the fluid medium on the temperature gradients inherent in any combustion system. The second involves the representation of the flame as an acoustic source.

This work presented methods for understanding and accounting for the effects of temperature on an acoustic field. Given the difficulty of attempting to experimentally measure acoustic temperature dependency, a more theoretical and mathematical approach was adopted. This approach involved a derivation and closed-form solution of a temperature-dependent differential wave equation. Sujith et. al. were some of the pioneers for this mathematical development [24, 25, 26, 27], and this thesis compiles a concise summary of many of these works. In addition, through the use of these analytical solution techniques, case studies using simple geometries and boundary conditions were utilized to isolate and study how different temperature profiles affect such things as standing-wave patterns, natural frequencies, and wave reflection. From these case studies, interesting correlations were observed. One can see from several of the plots in Section 6.4 that although the spatially averaged temperature may be identical, varying temperature profiles strongly change the acoustic fields and natural frequencies.

In addition, some fundamental observations concerning wave reflection could be made from the case studies. For example, it was found that the reflection coefficient has a wider frequency bandwidth when the temperature gradient is steeper. In addition, the magnitude of the reflection coefficient is dependent only on the overall jump or drop in temperature. These insights and others are discussed in greater detail in Chapter 6. Such insights are helpful in understanding how the flame will affect the acoustic field. One of the main lessons learned from this study was that correct specification of the temperature profile is needed to accurately reconstruct the acoustic response.

The next step was to determine how to incorporate temperature into the finite element model. Generally in an acoustic analysis, there are three properties that are dependent on temperature: bulk modulus, density, and the speed of sound. However, it was found by comparing the relationships of these properties that the temperature dependency for the acoustics can be characterized by specifying only the temperature dependency of the density. This simplification is accomplished due to the interdependency of the three acoustic properties.

In order to check the FE implementation of the temperature dependency, a comparison was made between the finite element model and the analytical solution. Again, case studies with simple geometries were used to isolate just the temperature dependency. From these case studies, a comparison of the acoustic velocity, pressure, reflection coefficient, and impedance were made between the FE and analytical solutions. When comparing these different quantities, the finite element model and the analytical solution yielded an exact match for the pressure and velocity field, as well as, for the impedance and reflection coefficients. This verifies that the finite element implementation yields results that we would expect.

In the case of the laboratory combustor used in this study, the temperature profile was measured using thermocouples placed at various locations along the length of the combustor. The temperature profile was then mapped to the finite element model and the corresponding temperature dependent properties were related to the mapped temperature.

10.2.3 Flame as an Acoustic Source

Another important contribution of this work was the representation of the flame as an equivalent acoustic source. This was done through a mathematical study of the governing conservation laws. By manipulating these equations into the proper form, a complete reactive wave equation can be achieved. This reacting wave equation incorporates multiple source terms. However, it was shown that for low Mach number premixed combustion, all of the source terms could be neglected except for the chemical reaction source term. Consequently, a simplified differential reacting wave equation was achieved. This equation is consistent with mathematical relationships used by other researchers for the flame as an acoustic source.

By investigating the reacting wave equation, it can be seen that the unsteady flame is mathematically similar to a loud speaker. Therefore, by comparing the differential wave equations of the loudspeaker and flame, an equivalent relationship for the flame as a source can be derived. The resulting relationship allows the flame to be represented as a "volumetric acceleration" with an extra time derivative and constant term. Consequently, in the finite element model, the flame can be represented as a volumetric acceleration. The big advantage of this equivalent source is that it can be readily applied in almost any commercial FE code that performs acoustic analysis.

10.2.4 Hot-acoustic Validation

The methodology for modeling the temperature gradients and the flame as an acoustic source were validated by experimentally measuring the frequency response of the pressure and velocity with respect to the flame as an acoustic source. Since both the high temperature effects and the flame as a source would be inherent in the frequency response measurement, this measurement was used as a means of validating the "hot-acoustic model". The measurement used a photomultiplier tube to pick up the light emission of one of the intermediate reactions in the combustion process that has been shown to be a good indication of the heat release. The output measurement of acoustic pressure and velocity was measured with microphones and a hot wire anemometer. With this instrumentation setup, the frequency response of the acoustic pressure and velocity with respect to the flame was measured. This measurement method was sensitive to the inherent noise in the system which resulted in some low coherence over certain frequency regions. However, this experimental method provided sufficient data as to adequately validate the acoustic finite element models. From the plots in Chapter 8, we can see that there is good correlation between the FE model and the experimental data.

10.2.5 Application

The end result of this research provided accurate acoustic transfer functions for the reduced-order thermoacoustic model. It was shown in Chapter 9 that insights into stability could be gained by simply looking at the acoustic transfer functions. However, in order to understand how fuel concentrations and mass-flow rates affect the stability, a full reduced-order model is needed. In coupling the acoustic transfer functions with the complete reduced-order model, a stability map was produced for the laboratory combustor. This map consisted of the prediction of unstable regions based on the variation of the fuel-air ratio and the mass flow rate. When comparing this stability map with experimental data, it was seen that the general trends matched well.

The next step would be to utilize the reduced-order model to help make design changes which would improve thermoacoustic stability. In addition, the future phases of this research need to show how reduced-order modeling techniques can be applied by industry on a larger scale. From an acoustic modeling standpoint, there are a few different considerations needed to achieve such goals.

10.3 Remaining Issues and Future Work

10.3.1 Remaining Issues

The hypothesis that finite element modeling could be used to accurately acquire the acoustic transfer functions for thermoacoustic stability prediction was shown to hold true. In spite of this success, there still remain some issues which need to be further researched. Some of these issues involve the 1-D acoustic modeling, the assumptions in the temperature profile representation, further investigation of the flame as an acoustic source, and improved methods for measuring the hot-acoustic FRF's.

It should be noted that although the 1-D acoustic model was appropriate for the laboratory combustor, as the scale of the problem increases, higher dimensionality or more complex models might be requisite. The need for such models depends largely on the frequency range and the geometric size of the combustor components. If a higher dimensionality model was required for a system, more work would be needed to understand how to defeature the geometry and represent the appropriate boundary conditions and sources.

Another area which could be addressed further involves the assumptions used to represent the high temperature gradients. During this development, the assumptions that were made were that the fluid medium is an ideal and isentropic gas. In addition, the temperature dependency of the damping in the system was assumed to be negligible. These assumptions are fairly standard in acoustic analysis; however, further investigation in these areas might provide more insights. Another assumption made was that the mean pressure remains essentially constant along the length of the combustor. This is probably a reasonable assumption for the laboratory combustor used in this study. However, for larger-scale combustors, this assumption may not be a reasonable and methods for estimating the pressure distribution might be required.

The development of the flame as the acoustic source also involved several assumptions. The main assumptions in this derivation were: low mach number flow, negligible turbulent noise, and a small flame zone compared to acoustic wavelength. If these or any other assumptions detailed in Chapter 7 are violated, a more involved source term might be needed. In particular, if a 3-D acoustic model were needed, a spatial development of the source would be required. This might be accomplished using techniques such as reduced equivalent loading. The representation of the flame as an acoustic source is an area where more research is significantly needed.

The last issue which needs more development is the experimental methods for acquiring the hot-acoustic transfer functions. In the current method, the signal-to-noise ratio is low, which produces less adequate results. Since the laboratory rig is a turbulent system, eliminating the noise is not really a possibility. Instead, one could obtain better results by increasing the amount of signal measured. The low signal to noise ratio occurs in two measurements. The first is in the hotwire anemometer or two microphone velocity probe, used to measure the acoustic velocity. The hotwire has a low dynamic sensitivity, and the error in the two microphone measurement is very sensitive to any unwanted noise in the system such as turbulence. The result is that both of these measurements can easily get buried in noise. The other measurement that has a low signal to noise problem is the photomultiplier tube which measures the heat-release rate. Based on the experience in this research, this was typically a bigger problem than the velocity measurement. The difficulty in obtaining hot-acoustic transfer functions might be improved by enhancing the quality of the measuring devices or by changing the measurement methods. Although the measurements presented in this research were adequate, there would be great advantage to independently measure the acoustic transfer functions.

10.3.2 Future Work

The next step is to utilize the methodology discussed in this thesis on larger-scale or industrial-size gas turbine combustors. One of the most challenging considerations in this effort would be to determine relevant sections of the combustor to be modeled and accurately specify the appropriate boundary conditions. In addition to this, further investigation into the acoustic representation of the flame for annular burners would be needed.

Another area which needs to be developed further is the determination of the temperature profile. In this research, the temperature was measured experimentally and then curve-fit. This might be more difficult to accomplish in an industrial gas turbine engine. Therefore methods such as FEA or CFD could be utilized without too much difficulty, since the fluid subvolume will already be created for the acoustic analysis. Improving the accuracy of the temperature distribution would improve the accuracy of the acoustic characterization.

In the previous section, some comments about the insufficient measurement methods were overviewed. This is an area where improvements are certainly needed for experimentally measuring hot-acoustic frequency response functions. As discussed, improved methods and instrumentation for measuring heat release and velocity would be advantageous. Another improvement in the experimental methods would be to design the laboratory or industrial combustor in such a way that more spatial measurements could be made. Since the finite element analysis is an approximation of the spatial pressure field, more spatial measurements would help validate the models.

The last area of future work might be to couple other aspects of the physics into the finite element model. For example one could incorporate aspects such as the flow, heat transfer, fuel, and flame dynamics. Developing such a formulation would allow the reduced-order model to include spatial dimensionality under a structured framework. The work presented in this thesis and the needed future work will help to further the progress of understanding and reducing thermoacoustic instabilities.

References

1. Entezam, B., Van Moorhemf, W, Majdalani, J., 1998, "A Novel Investigation of the Thermoacoustic Field Inside a Rijke Tube", 7th AIAA/ASME Joint Thermophysics and Heat Transfer Conference June 15-18, 1998/Albuquerque, NM
2. Fleifil, M., Hathout, J. P.,Annaswamy A. M., Ghoniem, A. F., 2000, "Reduced-order Modeling of Heat Release Dynamics and Active Control of Time-Delay Instability"
3. Cook, R., Malkus, D., Plesha, M., Witt, R., *Concepts and Application of Finite Element Analysis, Fourth Edition*, John Wiley & Sons, Inc, 2002
4. Rayleigh, J., *The Theory of Sound, Second Edition*, Dover Publications, New York, 1945
5. Lieuwn, T., McManus, K., 2003, "Introduction: Combustion Dynamics in Lean-Premiexed Prevaporized (LPP) Gas Turbines", Journal of Propulsion and Power, Vol 19 No 5
6. Poinsot and Veynante, 2005, *Theoretical and Numerical Combustion, Second Edition*, Chap. 8
7. Poinsot, T., Trouve, A., Veynante, D. Crandel, S., and Esposito, E., "Vortex-Driven Acoustically Coupled Combustion Instabililities," Journal of Fluid Mechanics, Vol. 177, 1987, pp. 265-292
8. Blocsidge, G. J., Dowling A. P., Langhorne, P. J., 1987, "Reheat buzz: an acoustically coupled combustion instability. Part 1. Experiment & Part 2. Theory", J. Fluid Mechanics, Vol 193, pp. 417-473.
9. Dowling, A. P., 1999, "A kinematic model of a ducted flame", J. Fluid Mech., Vol. 394, pp. 51-72.
10. Martin, C., 2006, "Systematic Prediction and Parametric Characterization of Thermoacoustic instabilities in premixed gas turbine combustors," Masters thesis, Department of Mechanical Engineering, Virginia Tech
11. Park, S., Annaswamy, A., Ghoniem, A., 2002, "Heat release dynamics modeling for combustion instabilities analysis of kinetically controlled burning.", Combustion and Flame, Vol. 128, pp. 217-231.
12. Lieuwen, T., Neumeier, Y., Zinn, B. T., 1998, "The Role of Unmixedness and Chemical Kinetics in Driving Combustion Instabilities in Lean Premixed Combustors," Combustion science and Technology, Vol 135, n. 1-6, pp. 193-211

13. Schuermans, B., Bellucci, V., Paschereit, C. O., 2003, “Thermoacoustic Modeling and Control of Multi Burner Combustion Systems”, ASME Turbo Expo, June 10-19, Atlanta GA, pp. 1-10
14. Pankiewitz, C., Fischer, A., Hirsch, C., Sattelmayer, T., 2003, “Computation of Transfer Matrices for Gas Turbine Combustors Including Acosutic/Flame Interaction”, AIAA/CEAS Aeroacoustic Conference and Exibit, 12-14 May, Hilton Head, SC, pp.1-10
15. Kruger, U., Huren, J., Hoffmann, S., Krebs, W., Flogr, P., 2001, “Prediction and Measurment of Termoacoustic Improvements in Gas Turbines with Annular Combustions Systems”, Journal of Engineering for Gas Turbines and Power, Vol. 123, pp. 557-566
16. Walz, G., Krebs, W., Hoffmann, S., Judith, H., 2002, “Detailed Analysis of the Acoustic Mode shapes of an Annular Combustion Chamber”, Vol. 124, pp. 3 – 9
17. Pankiewitz, C., Sattelmayer, T., 2003, “Time Domain Simulation of Combustion Instabilities in Annular Combustors,” Journal of Engineering for Gas Turbines and Power, Vol 125, pp. 677-685.
18. Krüger, U., Hüren, J., Hoffmann, S., Krebs, W., Flohr, P., and Bohn, D., 2001, "Prediction and Measurement of Thermoacoustic Improvements in Gas Turbines With Annular Combustion Systems," ASME J. Eng. Gas Turbines Power, 123, pp. 557–566.
19. ABAQUS 6.6-3 User Manuals
20. Kinsler, L. and Frey A., 2000, *Fundamentals of Acoustics, Fourth Edition*, New York
21. Pierce, A. D., 1989, *Acoustics, An Introduction to Its Physical Principles and Applications*, Acoustical Society of America, Melville
22. ASTM E 1050, 1998, “Standard Test Method for Impedance and Absorption of Acoustical Materials Using A Tube, Two Microphones and A Digital Frequency Analysis System”, ASTM Designation: E 1050 – 98
23. Karthik, B., Kumar, B. M., and Suijith, R. I., 2000, “Exact Solution to One-dimensional Acoustic Fields with Temperature Gradient and Mean Flow,” J. Acoust. Soc. Am. Vol. 108, pp. 38-43
24. Sujith, R. I., Waldherr, G. A. and Zinn, B. T., 1995, “An exact solution for one-dimensional acoustic fields in ducts with an axial temperature gradient,’’ J. Sound Vib. 184, 389–402 ~
25. Sujith, R. I., “On the Propagation of Acoustic Waves Through a Region of Temperature Gradient”

26. Kumar, B. M. and Sujith, R. I., 1998, "Exact Solution for One-Dimensional Acoustic Fields in Ducts with Polynomial Mean Temperature Profile," J. of Vibration and Acoustics 120, 965-969
27. Kumar, B. M. and Sujith, R. I., 1997, "Exact Solution for One-Dimensional Acoustic Fields in Ducts with Quadratic Mean Temperature Profile" J. Acoust. Soc. Am., Vol. 101, pp. 3798-3799
28. Abramowitz, M. and Stegun, I. A., 1972, *Handbook of Mathematical Functions with Formulas, Graphs and Mathematical Tables*, Wiley, New York
29. Turns, S. R., 2000, *An introduction to combustion: concepts and applications, Second Eddition* McGraw Hill, Boston, Additional CD
30. Kuo, K. K., 1986, *Principles of Combustion*, John Wiley & Sons, Inc., New York, Chap. 3
31. Batra, R. C., 2006, *Elements of Continuum Mechanics*, AIAA, Reston, Chap 2
32. Kotake, S., 1975, "On Combustion Noise Related to Chemical Reactions", Journal of Sound and Vibration, Vol 42, No. 3, pp. 399-410
33. Haber, L. and Vandsburger, U., "A Globar Reaction Model for OH* Chemiluminscence Applied to a Laminar Flat-Flame Burner," Combustion Science and Technology, Vol. 175, 2003, pp 1859-1891
34. Lee, J. G. and Santavicca, D. A., 2003, "Experimental Diagnostics for the Study of Combustion Instabilities in Lean Premixed Combustors", Journal of Propulsion and Power, Vol. 19, No. 5, pp. 735-748
35. Pankiewitz, C. and Sattelmayer, T., 2003, "Time Domain Simulation of Combustion Instabilities in Annular Combustors", Journal of Engineering for Gas Turbines and Power, Vol. 125, pp. 677-685
36. Forssen, B. and Crocker, M., 1983, "Estimation of acoustic velocity, surface velocity, and radiation efficiency by use of the two-microphone technique", Journal of the Acoustical Society of America, Vol. 73, No. 3, pp. 1047-1053

Appendix A: Experimental Measurements & Calibration

Microphone Calibration

If true units of pressure are desired, a calibration factor should be used to get the microphones signals to the proper engineering unit. The most common method and the one used in this research is to use a pistonphone calibrator with a known output. Typically the output is a single tone with the amplitude given in decibels and a reference pressure of 20 micro-Pascals. The tones on our calibrator ranged from 250 Hz to 10,000 Hz. Although we typically used a calibration at 1,000 Hz since that is standard. The calibration factor comes out to be the following

$$H_{cal} = \frac{(20E-6)\left(10^{Amp/20}\right)}{Measured\,Voltage}. \tag{A,1}$$

Therefore the measured voltage from the microphone can be multiplied by this factor to get the acoustic pressure

$$p' = \left[Voltage_{meas.} \times H_{cal}\right] \quad (Pascals) \tag{A,2}$$

Data Acquisition

The acoustic experimental data acquisition was performed on an HP analyzer. Appropriate sampling rate and methods are predefined in the analyzer based on the frequency range of interest. Where the analyzer performed all of the averaging, windowing, and frequency signal processing. However, some trivial signal processing was necessary to acquire the acoustic velocity data.

Although the acoustic experimentation in this research used a digital signal analyzer, other data acquisition equipment could have been used such as LabVIEW. This does require more caution and setup time on the part of the experimentalist.

Experimental Velocity Measurement Development

Sound pressure can be measured easily with the use of a microphone; however, acoustic velocity presents some challenges. Using the conservation of momentum equation, the acoustic velocity can be related to the pressure gradient

$$-\nabla p = \rho\left[\frac{\partial u}{\partial t} + (u \cdot \nabla) u\right]. \tag{A,3}$$

Making the normal assumptions for acoustic analysis with small perturbations about a mean, no mean flow, and neglecting the higher order terms, Eq. (A,3) simplifies to the following common form,

$$\frac{\partial u'}{\partial t} = -\frac{1}{\rho}\nabla p' . \tag{A,4}$$

The equation can be simplified further if one only considers the velocity along some vector, **r**,

$$\frac{\partial u_r'}{\partial t} = -\frac{1}{\rho}\frac{\partial p'}{\partial r} . \tag{A,5}$$

The pressure gradient in Eq. (A,5) can be approximated using a two microphone technique. In this technique, two microphones are spaced some small distance apart along the **r** vector. The pressure gradient is then approximated using the finite difference method where the pressure signals from the two microphones are subtracted and then divided by the distance between them Δr

$$\frac{\partial u_r'}{\partial t} = -\frac{1}{\rho}\left(\frac{p_2' - p_1'}{\Delta r}\right). \tag{A,6}$$

At this point the Fourier Transform $\left(X = \int_{-\infty}^{\infty} x(t) e^{-i\omega t} dt\right)$ can be applied to Eq. (A,6),

$$\int_{-\infty}^{\infty} \frac{\partial u_r'}{\partial t} e^{-i\omega t} dt = -\frac{1}{\rho \Delta r}\left(P_2 - P_1\right). \tag{A,7}$$

The variables P_1 and P_2 are the Fourier Transforms of the time domain pressures, p_1' and p_2'. Integrating Eq. (A,7) by parts one gets the following expression,

$$e^{-i\omega t}\, u_r' \Big|_{-\infty}^{\infty} + i\omega \int_{-\infty}^{\infty} u_r' e^{-i\omega t} dt = -\frac{1}{\rho \Delta r}\left(P_2 - P_1\right). \tag{A,8}$$

The second term on the left hand side of Eq. (A,8) is simply the Fourier Transform of the acoustic velocity multiplied by ($i\omega$). The first term in Eq. (A,8) can be forced to zero by setting the acoustic velocity to zero at positive and negative infinity. Consequently instead of an ordinary Fourier Transform, a finite Fourier Transform is applied. The finite Fourier Transform is in most practical signal processing. Performing the operations discussed above, the discrete Fourier Transform of the acoustic velocity can be simplified to the following expression,

$$U(f) \cong \frac{i}{\omega \rho \Delta r}\left(P_2(f) - P_1(f)\right). \tag{A,9}$$

It should be noted that the above derivation was based on the one given by Forssen et al. [36].

Auto-Spectral Density Formulation

From here, the auto-spectral density can be determined for the acoustic velocity. The auto-spectral density is defined as follows

$$G_{uu} = \frac{2}{T}\left[U^{*}U\right], \tag{A,10}$$

where the symbol "*" represents the complex conjugate and the capital letter, U represents the Fourier transform of the acoustic velocity. For the sake of completeness, the auto-spectral density can also be related to the mean-squared value of the velocity in the following way.

$$G_{uu}\Delta f = \lim_{T\to\infty}\int_0^T u^2(t)dt \tag{A,11}$$

Equation (A,10) can now be used to find the auto-spectral density of the acoustic velocity,

$$G_{uu} = \frac{2}{T}\left(\frac{i}{\omega\Delta r\rho}\left(P_2 - P_2\right)\right)^{*}\left(\frac{i}{\omega\Delta r\rho}\left(P_2 - P_2\right)\right), \tag{A,12}$$

$$G_{uu} = \frac{2}{T\left(\omega\Delta r\rho\right)^2}\left[P_2^{*}P_2 + P_1^{*}P_1 - \left(P_2^{*}P_1 + P_1^{*}P_2\right)\right], \tag{A,13}$$

$$G_{uu} = \frac{1}{\left(\omega\Delta r\rho\right)^2}\left[G_{22} + G_{11} - \left(G_{21} + G_{12}\right)\right], \tag{A,14}$$

$$G_{uu} = \frac{1}{\left(\omega\Delta r\rho\right)^2}\left[G_{22} + G_{11} - 2\,\mathrm{Re}\left(G_{12}\right)\right], \tag{A,15}$$

where G_{11} and G_{22} are auto power-spectral densities of P_1 and P_2 respectively. In addition, G_{12} is the cross-power-spectral density of P_1 and P_2. The above derivation follows that given by Forssen et al [36].

Transfer Function Formulation

If now the acoustic velocity is considered to be the output of a transfer function which is driven by some arbitrary source, *s*, a transfer function can found between the acoustic velocity and the source using the following procedure. Let the symbol *S* be the Fourier Transform of the source signal *s*. The transfer function can then be expressed as follows

$$H_{SU} = \frac{U(f)}{S(f)} = \frac{S(f)^{*}U(f)}{S(f)^{*}S(f)}, \tag{A,16}$$

$$H_{SU} = \frac{i}{\omega\rho\Delta r}\frac{S(f)^*\left(P_2(f)-P_1(f)\right)}{S(f)^* S(f)} = \frac{i}{\omega\rho\Delta r}\frac{S(f)^* P_2(f)-S(f)^* P_1(f)}{S(f)^* S(f)}, \quad \text{(A,17)}$$

$$H_{SU} = \frac{i}{\omega\rho\Delta r}\frac{G_{SP_2}-G_{SP_1}}{G_{SS}} = \frac{i}{\omega\rho\Delta r}\left(H_{SP_2}-H_{SP_1}\right), \quad \text{(A,18)}$$

where H_{SP1} and H_{SP2} are the transfer functions between p_1' and the source and p_2' and the source respectively.

There are, however, a few precautions that need to be taken to get accurate two microphone acoustic velocity results:

Finite Difference Error

The pressure gradient in Eq. (A,5) is approximated with the finite difference technique between two microphones,

$$P \approx \frac{P_1+P_2}{2} \text{ and } \frac{\partial P}{\partial r} = \frac{P_2-P_1}{\Delta r}. \quad \text{(A,19)}$$

From the equation above we can see that as the distance between the microphones, Δr gets smaller we will obtain a better approximation of the pressure gradient. However, the irony is that the closer one spaces the microphones, the smaller the difference will be between the two pressure signals. When subtracting the two similar signals, any error or noise inherent in the pressure measurement will get amplified.

Consequently, there is a balance between these two conflicting constraints. From studies done by Waser Et al, an ideal spacing of the microphones for a frequency range of 31.5 Hz to 1.25 kHz is about 2 inches. This general suggestion of course can be optimized based on more precise frequency range of interest and signal-to-noise ratios.

Instrumentation Phase Mismatch and Calibration

At low frequencies the phase difference between two pressure signals becomes very small and can eventually reach the order of magnitude of the accuracy of the instrumentation. Therefore at low frequencies the measurement error is very sensitive to the instrumentation phase error. There are two ways to compensate for this problem. The first is to increase the physical phase difference by increasing the microphone spacing. The second way to correct the phase mismatch is to calibrate one microphone relative to the other (although this method has not shown very useful in our experimental setup). This can be done by finding the transfer function between the two microphones.

An easy way to perform this calibration is to flush mount the microphones in a rigid circular plate attached to the end of a tube. Ideally, the microphones should measure the same pressure with zero phase shift. The frequency response can then be measured with the system excited with white noise,

$$H_{12} = \frac{G_{12}}{G_{11}} \qquad \text{(A,20)}$$

The microphone response can then be corrected as follows,

$$\begin{aligned} \left(G_{11}\right)_c &= G_{11}, \\ \left(G_{22}\right)_c &= G_{22} \big/ \left|H_{12}\right|^2, \\ \left(G_{12}\right)_c &= G_{12} / H_{12}. \end{aligned} \qquad \text{(A,21)}$$

The corrected spectral densities and transfer functions can found by substituting the proper calibration factors into Eqs. (A,15) and (A,18) obtain more accurate results.

It should also be noted that to get actual units of velocity the microphone signals need to be calibrated as described above in Eqs. (A,1) and (A,2).

Velocity Processing Conclusion

The calibration factors can be substituted into Eqs. (A,15) and (A,18).

$$\left(G_{uu}\right)_c = \frac{H_{cal}}{\left(\omega \Delta r \rho\right)^2}\left[G_{11} + G_{22} \big/ \left|H_{12}\right|^2 - 2\,\mathrm{Re}\left(G_{12}/H_{12}\right)\right] \qquad \text{(A,22)}$$

$$\left(H_{SU}\right)_c = \frac{iH_{cal}}{\omega \rho \Delta r}\left(H_{SP_2}/H_{12} - H_{SP_1}\right) \qquad \text{(A,23)}$$

When trying to find the transfer function, an alternative approach may be taken using a single microphone. Instead of using two microphones, a single microphone may be used by taking one measurement in microphone position one and then moving the microphone to position two. By doing this the relative calibration factor is not needed resulting in the following equation and the phase mismatch error is completely eliminated.

$$H_{SU} = \frac{iH_{cal}}{\omega \rho \Delta r}\left(\left(H_{SP_1}\right)_2 - \left(H_{SP_1}\right)_1\right) \qquad \text{(A,24)}$$

This method proves to be slightly more accurate. However, in some applications, it is not a practical solution and a relative calibration should be performed.

Two Microphone Velocity Probe Case Study

A simple case study is presented below to show the utility and areas of caution when using the mathematical derivation described above. This study was done on a straight duct with an 8 inch cross-sectional diameter as shown in the figure below.

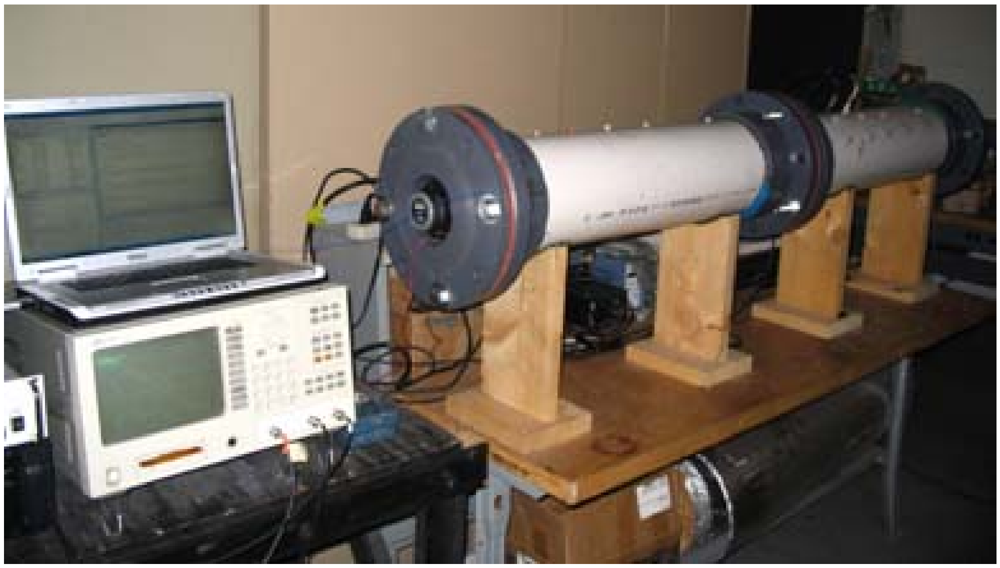

Fig. A.1: Experimental setup for the 2 microphone probe case study. 8 inch diameter PVC tubing driven at one end with a speaker. Two microphone probe place after center junction

Let us first start out looking at a finite element representation of the system. We can get a good indication of what the pressure and velocity should look like from the frequency response plots below. In Fig. A.2 and Fig. A.3, Finite Element frequency response plots are shown between pressure or velocity as the input and a volumetric acceleration speaker source as the input.

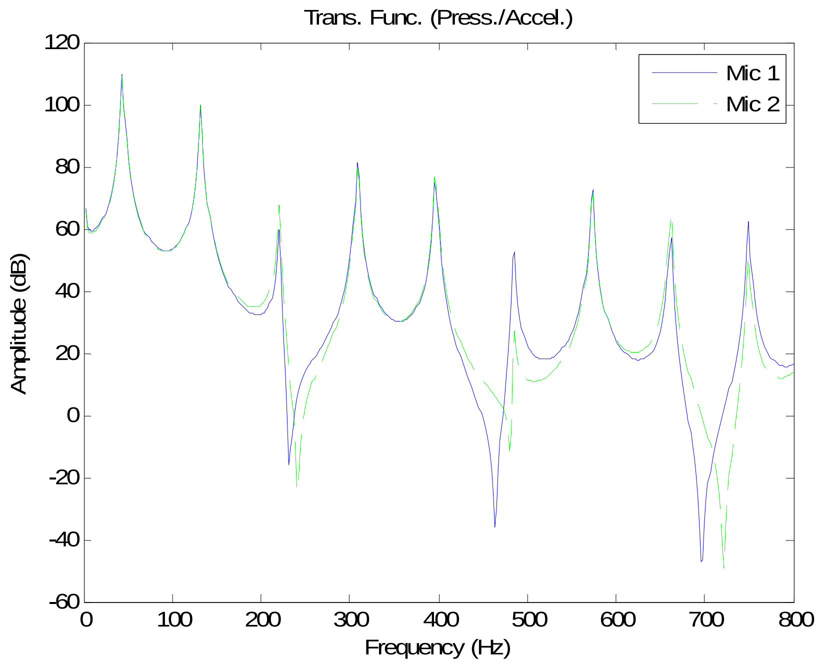

Fig. A.2: Pressure signals taken from the FE model of the 8" diameter duct. The pressure signals are taken at the locations of experimental 2 microphone probe.

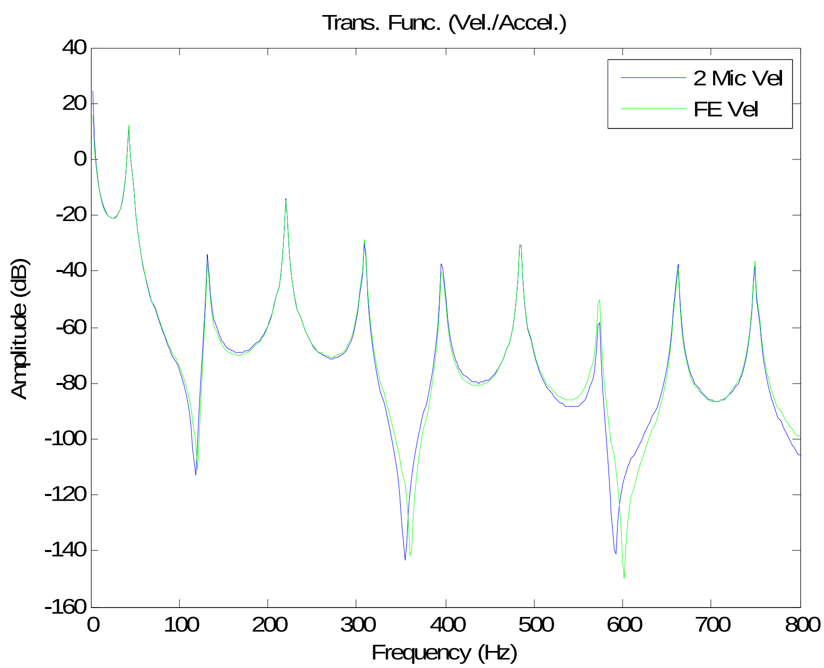

Fig. A.3: Comparison between the acoustic velocity at the location of the location of the 2 microphone probe. Here the velocity is calculated directly from the FE model and also calculated using the 2 microphone method from the FE pressure field.

One can see from Fig. A.3 that, theoretically, FE the two microphone velocity approximation correlates very well with the actual calculated FE velocity. However, as we will see below, when experimental noise is introduced the method is not nearly as good.

The first example given below shows the two microphone probe with a microphone spacing of 1 inch.

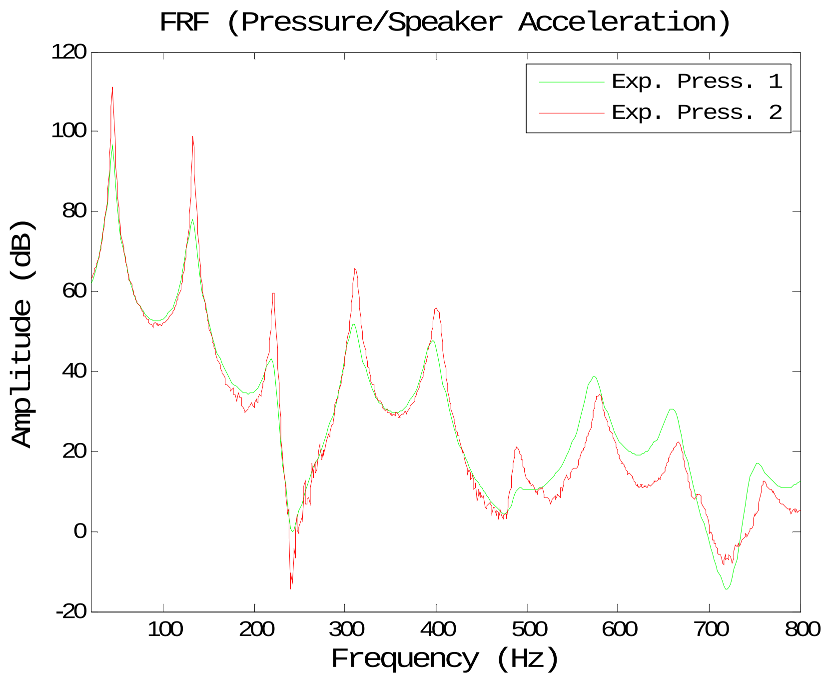

Fig. A.4: Frequency response plots with the pressure as the output and the speaker acceleration as the input. In this case the microphones were spaced an inch apart at a location of 4 feet downstream of the speaker

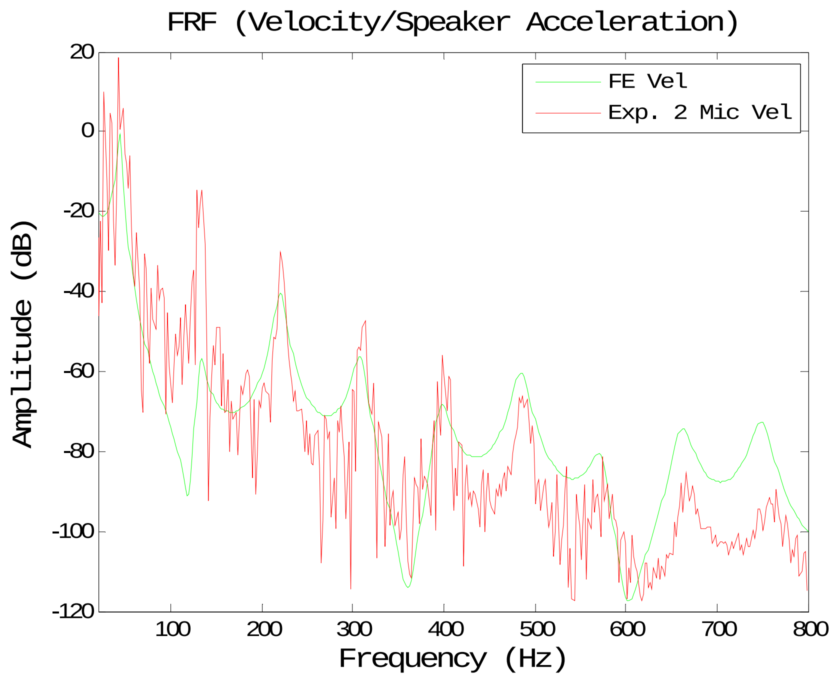

Fig. A.5: Comparison of the FE acoustic velocity to that measured by the two microphone technique when calculated using the first part of Eq. (A,18)

We can then space the microphones apart a greater distance and see what effect this has on the velocity calculation. Here we tried a spacing of 7.75 inches.

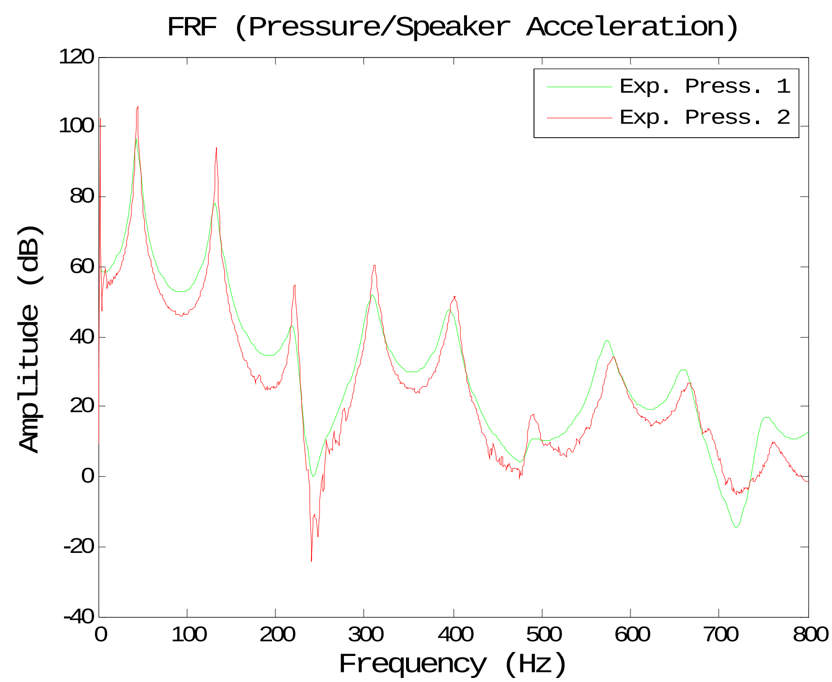

Fig. A.6: Frequency response plots with the pressure as the output and the speaker acceleration as the input. In this case the microphones were spaced 7.75 inchs apart at a location of 4 feet downstream of the speaker

In calculating the velocity, we used two different methods. First we use two different microphones. The second plot shows the velocity calculation performed with the same microphone and moved its location.

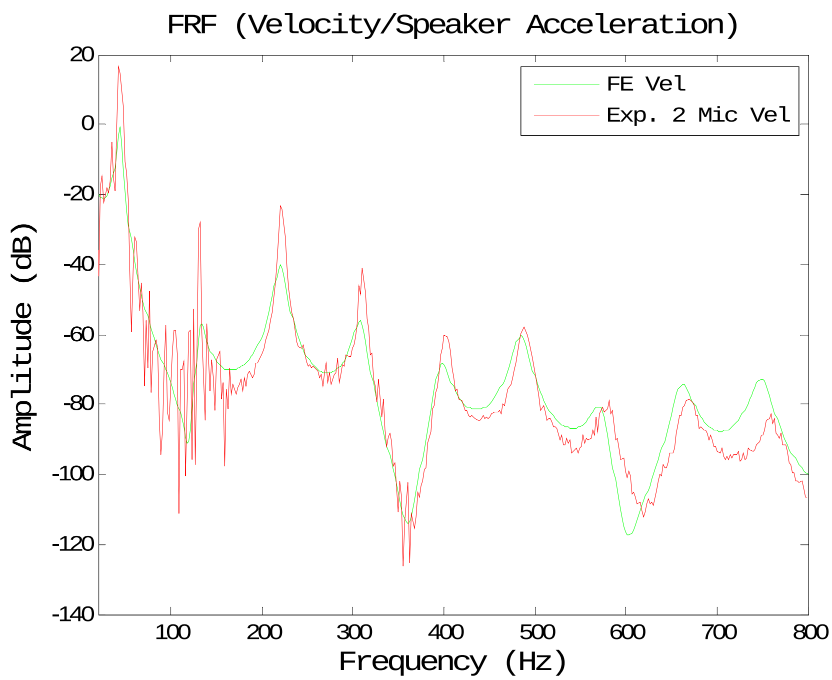

Fig. A.7: Comparison of the FE acoustic velocity to that measured by the two microphone technique with two different microphones and a spacing of 7.75 inches apart. Calculated using the first part of Eq. (A,18)

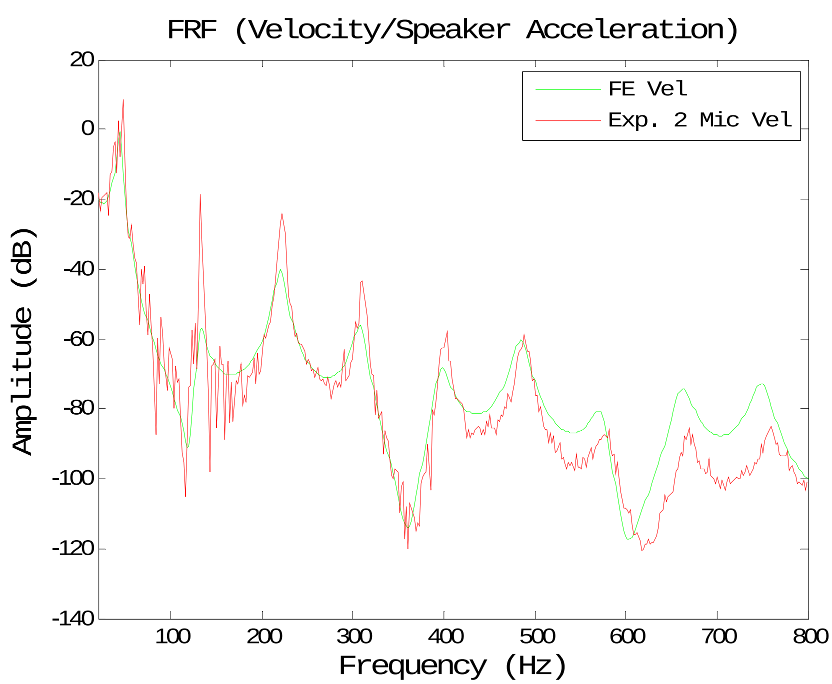

Fig. A.8: Comparison of the FE acoustic velocity to that measured by the two microphone technique using the same microphone and a spacing of 7.75 inches apart. Calculated using the first part of Eq. (A,18)

Lastly, the velocity was calculated using the second part of Eq. (A,18). The plot below displays this. In this plot, two microphones are spaced about 11/2 inches apart. It is quite obvious there is a notable difference when using the second part of Eq. (A,18). The difference has to do with the way in which the time records are averaged. If one averages the ratio of the cross spectrum to the auto-spectrum, it works significantly better than if the cross spectrum and auto-spectrum are calculated separately and then the ratio is taken.

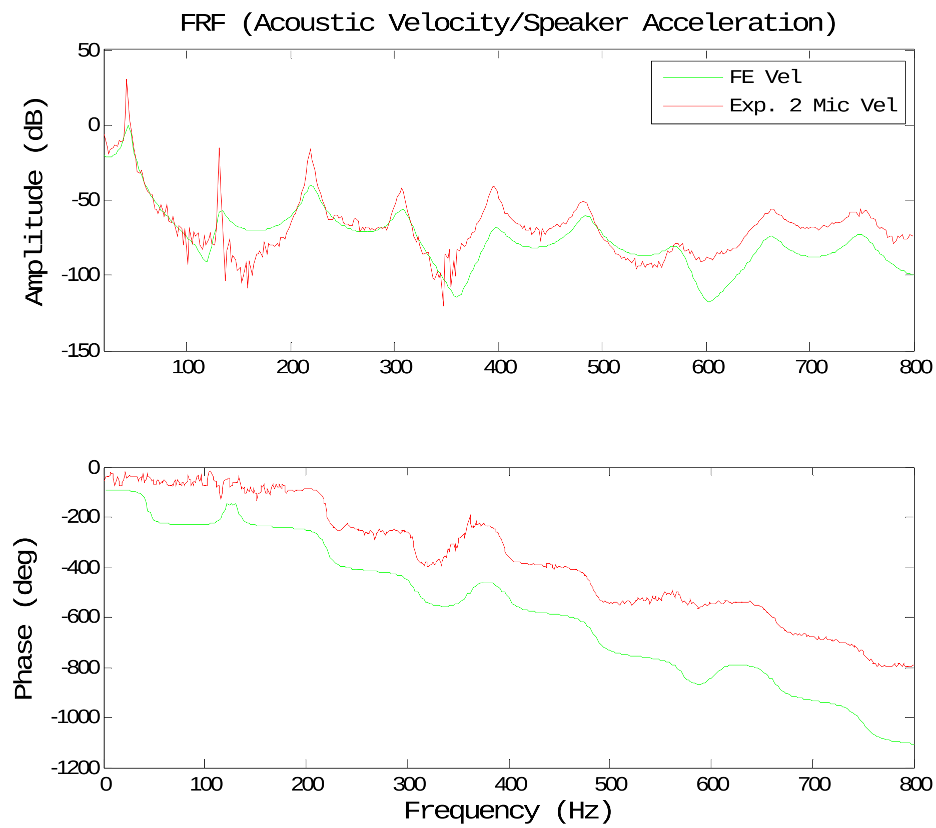

Fig. A.9: Comparison of the FE acoustic velocity to that measured by the two microphone technique using two different microphones and a spacing of 1.5 inches apart. Calculated using the second part of Eq. (A,18)

Sample Code for Signal Processing

```
clear all; clc; close all;

%-------------------------------------------------
%                                                *
%         Signal Processing for Cold             *
%           Acoustic Measurements                *
%                                                *
%-------------------------------------------------


%--------------Finite Element Results----------------
load mic1_2; P1 = mic1_2;    load mic2_2; P2 = mic2_2;
load mic3_2; P3 = mic3_2;    load mic7_2; P7 = mic7_2;


%% Frequency Range
f = (1:1:800)';
w = 2*pi*f;

%% Velocity Calculation
rho = 1.21; %Density metric units
dx1 = 1.5*(0.0254); %microphone seperation near flame
dx2 = 4*(0.0254); %microphone seperation near mixing

U1 = i./(w*(dx1)*rho).*(P2 - P1); %Velocity Flame
U7 = i./(w*(dx2)*rho).*(P7 - P3); %Velocity Mixing

FE_data = [P1 P7 U1 U7];

for n = 1:4
    figure(n)
    subplot(3,1,1)
        plot(f,10*log10(abs(FE_data(:,n))),'b','linewidth',1.5)
    subplot(3,1,2)
        plot(f,unwrap(180/pi*angle(FE_data(:,n)),190),'b','linewidth',1.5)
end

%% ---------------Experimental----------------------------------
%Load Data
cal = 52.25; %Calibration factor
load HS1_2; HSP1 = o2i1*cal; load HS2_2; HSP2 = o2i1*cal;
load HSP3;  HSP3 = o2i1*cal; load HSP7;  HSP7 = o2i1*cal;

load coh1; coh1 = o2i1;     load coh7; coh7 = o2i1;
load coh2; coh2 = o2i1;     load coh8; coh8 = o2i1;

f = o2i1x; w = f*21*pi;

%Pressure mic 1
figure(1)
subplot(3,1,1); hold on
plot(f,10*log10(abs(HSP1)),'r','linewidth',1.5); xlim([20 500]); ylim([-7 22]);
```

```
h = ylabel('Amplitude (dB)','Fontsize',13); set(h,'FontName','FixedWidth')
grid on; box on

subplot(3,1,2); hold on
plot(f,unwrap(180/pi*angle(HSP1),325),'r','linewidth',1.5);  xlim([20 500]);
ylim([-400 20]);
h = ylabel('Phase (deg)','Fontsize',13); set(h,'FontName','FixedWidth')
h = legend('Finite Element','Experimental','Fontsize',12);
set(h,'FontName','FixedWidth')
grid on; box on

subplot(3,1,3); hold on
plot(f,coh1,'r','linewidth',1.5);  xlim([20 500]);
h = xlabel('Frequency (Hz)','Fontsize',13); set(h,'FontName','FixedWidth')
h = ylabel('Coherence','Fontsize',13); set(h,'FontName','FixedWidth')
grid on; box on

%Pressure at fuel lines
figure(2)
subplot(3,1,1); hold on
plot(f,10*log10(abs(HSP7)),'r','linewidth',1.5);xlim([20 500]); ylim([[-10
20]]);
h = ylabel('Amplitude (dB)','Fontsize',13); set(h,'FontName','FixedWidth')
grid on; box on

ang = unwrap(180/pi*angle(HSP7),300);
subplot(3,1,2); hold on
plot(f,ang,'r','linewidth',1.5);  xlim([0 500])%;ylim([-200 100]);
h = ylabel('Phase (deg)','Fontsize',13); set(h,'FontName','FixedWidth')
h = legend('Finite Element','Experimental','Fontsize',12);
set(h,'FontName','FixedWidth')
grid on; box on

subplot(3,1,3); hold on
plot(f,coh7,'r','linewidth',1.5);  xlim([20 500]);
h = xlabel('Frequency (Hz)','Fontsize',13); set(h,'FontName','FixedWidth')
h = ylabel('Coherence','Fontsize',13); set(h,'FontName','FixedWidth')
grid on; box on

%Velocity
Gv_flame = (i./(w*dx1*rho)).*(HSP2-HSP1);
Gv_mixing = (i./(w*dx2*rho)).*(HSP7-HSP3);

%Velocity at flame
figure(3);
subplot(3,1,1); hold on
plot(f,10*log10(abs(12*Gv_flame)),'r','linewidth',1.5); xlim([20 500]);ylim([-37
-3]);
h = ylabel('Amplitude (dB)','Fontsize',13); set(h,'FontName','FixedWidth')
h = legend('Finite Element','Experimental'); set(h,'FontName','FixedWidth')
grid on; box on

ang = unwrap(180/pi*angle(Gv_flame),170)+240;
subplot(3,1,2); hold on
plot(f,ang,'r','linewidth',1.5);  xlim([20 500]);ylim([-360 220]);
h = xlabel('Frequency (Hz)','Fontsize',13); set(h,'FontName','FixedWidth')
h = ylabel('Phase (deg)','Fontsize',13); set(h,'FontName','FixedWidth')
```

```
grid on; box on

subplot(3,1,3); hold on
plot(f,coh1.*coh2,'r','linewidth',1.5);  xlim([20 500]);
h = xlabel('Frequency (Hz)','Fontsize',13); set(h,'FontName','FixedWidth')
h = ylabel('Coherence','Fontsize',13); set(h,'FontName','FixedWidth')
grid on; box on

%Velocity at fuel lines
figure(4)
subplot(3,1,1); hold on
plot(f,10*log10(abs(12*Gv_mixing)),'r','linewidth',1.5); xlim([20 500]);ylim([-
30 0]);
h = ylabel('Amplitude (dB)','Fontsize',13); set(h,'FontName','FixedWidth')
grid on; box on

ang = unwrap(180/pi*angle(Gv_mixing),244);
subplot(3,1,2); hold on
plot(f,ang,'r','linewidth',1.5);  xlim([20 500]);ylim([-500 100]);
h = xlabel('Frequency (Hz)','Fontsize',13); set(h,'FontName','FixedWidth')
h = ylabel('Phase (deg)','Fontsize',13); set(h,'FontName','FixedWidth')
h = legend('Finite Element','Experimental'); set(h,'FontName','FixedWidth')
grid on; box on

subplot(3,1,3); hold on
plot(f,coh7.*coh8,'r','linewidth',1.5);  xlim([20 500]);
h = xlabel('Frequency (Hz)','Fontsize',13); set(h,'FontName','FixedWidth')
h = ylabel('Coherence','Fontsize',13); set(h,'FontName','FixedWidth')
grid on; box on
```